OPTICALLY DRIVEN LIMIT CYCLE OSCILLATIONS IN MEMS

A Dissertation

Presented to the Faculty of the Graduate School

of Cornell University

in Partial Fulfillment of the Requirements for the Degree of

Doctor of Philosophy

by

David Benjamin Blocher

August 2012

OPTICALLY DRIVEN LIMIT CYCLE OSCILLATIONS IN MEMS

David Benjamin Blocher, Ph.D.

Cornell University 2012

We examine the dynamics of nanoscale bridge resonators fabricated from SOI wafers. When illuminated within an interference field, resonators are seen to self-oscillate due to feedback between heating and displacement. They are driven in high vacuum and their motion transduced with laser interferometry. Analysis of Maxwell's equations indicates that laser heating is not confined to the resonator's top surface. A finite element model is built to study thermo-mechanical coupling. Analysis shows that feedback is strongest in barely post-buckled beams, leading to low power self-oscillation. A theoretical model is built starting with the continuum description of the temperature and displacement fields and a Galerkin projection is used to obtain a set of coupled ordinary differential equations. These equations are analyzed using numerical continuation and perturbation theory. Analysis of the model suggests that a Hopf bifurcation leads to limit cycle oscillations and that multiple stable limit cycles may be possible due to periodicity in the interference field. The threshold power for self-oscillation as well as the amplitude, frequency, and frequency noise are measured experimentally. Measured amplitude-frequency relationships verify the predicted softening/hardening nature of first and second mode vibrations in pre- and post-buckled beams. Experimental results suggest that frequency noise in self-oscillating beams is due to instability in the power of the laser drive. Fluctuations in the laser power result in fluctuations of the resonant frequency via the power-amplitude-frequency relationship. Self-resonant beams

are also driven inertially and regions of sub- and superharmonic entrainment are measured, where the resonator response frequency is a whole multiple or sub-multiple of the drive frequency.

BIOGRAPHICAL SKETCH

The author was born in Durham, NC and received the B.S. degree in physics from Duke University, in May 2004. After college, he worked for an NGO in Malaysia bringing kindergarten education to estate regions and subsequently waited tables at Elmo's diner in Durham NC. In March 2006, he joined the research staff at MIT Lincoln Laboratory in Lexington MA, and left in August 2007 to pursue his Ph.D. in Theoretical and Applied Mechanics at Cornell University. In September 2012 he will begin a post-doctoral position at the University of California, Irvine.

to my mother: who demonstrated integrity, passion, and perseverance

ACKNOWLEDGEMENTS

This work was supported by a grant from the National Science Foundation, and teaching appoints within Cornell's Mathematics, Theoretical and Applied Mechanics, and Mechanical and Aerospace Engineering departments. Fabrication work was performed under the guidance of the staff at Cornell's Center for Nanoscale Science and Technology, and Center for Materials Research, with additional support from innumerable colleagues. I owe a great deal to my advisor Alan Zehnder for his confidence, support, and guidance over the last 5 years. The space he granted for independent research, and his patience in spite of my ever changing research interests, allowed me to grow as a scientist.

In addition, I have been blessed with a number of personal and professional mentors over the years without whom nothing would be possible. From a young age my mother inspired my interest in mathematics and the world, showing me how to ensure that a basketball post was mounted orthogonal to the ground using the Pythagorean theorem. My high school physics teacher, David Green stimulated my interest in physics by insightfully answering all of my questions with questions. At Duke, Prof. Henry Greenside introduced me to the intersection of physics and computing, and later guided me to attend graduate school. At Cornell, weekly meetings of diner club, and the thesis writing group have been a tremendous source of support: thank you Alexis, Ben, Joel, Matt, Nick, and Rocio. I am forever in debt to Ricardo H., Mike K., Liz A., and the countless nameless others who have seen me through my most difficult personal times at Cornell.

Lastly, I am forever grateful to the scholars who came before me, specifically: to the engineer and mathematician Henri Poincaré for showing me the beautiful geometry of differential equations; to the physicist Balthasar van der Pol for his

pioneering work on limit cycles; to mathematicians Frank Hoppensteadt and Eugene Izhikevich for their inspiring work on neural networks; and finally to R.M. Langdon, D.L. Dowe, and others who first discovered interferometrically transduced self-oscillations in MEMS.

TABLE OF CONTENTS

LIST OF TABLES

LIST OF FIGURES

CHAPTER 1

INTRODUCTION

1.1 Introduction and Motivation

Made possible by mature technologies for micro-fabrication developed for the electronics industry, over the last few decades researchers have begun fabricating micro-scale devices whose operating principle is mechanical [12, 69, 72, 128], optical [87], magnetic [89], thermal [122] or even relying on coupled-fields [99, 113]. Shifting attention away from silicon's electrical properties to it's mechanical properties [95] has enabled the design of accelerometers [62], pressure sensors [62], switches [102], micro-mirror displays [109], mass detectors [127, 53, 137, 135], clocks [69], filters [72], as well as other microelectromechanical systems (MEMS). MEMS devices may be co-fabricated with drive and detection circuitry, since they are fabricated using the same techniques as microprocessors. In addition, their small size ($\sim 10^{-6}$m) allows for low cost batch-fabrication and packaging.

Resonant MEMS devices have been of particular interest due to their application to resonant sensing and signal processing. In resonant sensing, the frequency of oscillation of the MEMS device carries information about the quantity of interest. Such applications rely on the sharply peaked, high frequency resonance curves possible in lightly damped small devices. Due to silicon's low material damping, devices such as the double-paddle oscillator have demonstrated mechanical quality factors as high as $Q = 5 \times 10^7$ at cryogenic temperatures [115], and cantilevers with frequencies reaching into the low GHz range have been fabricated by shrinking the device dimensions to the nanoscale [73]. Low

damping, and coupling of electro-mechanical, or opto-mechanical fields has resulted in novel inherently non-linear effects such as parametric amplification [143, 112], self-oscillation [7], and amplitude-frequency relationships, making MEMS a rich test bed for experimental nonlinear dynamics.

In order to induce vibrations, MEMS devices are often excited electrostatically [3], piezoelectrically [36], magnetically [114], optically [66, 55, 54, 35], or thermoresistively [103] with an externally modulated input signal. However, such methods require an independent, highly stable periodic drive signal and may require additional conductive layers on the resonator surface which increase damping and broaden the resonant peak. It has been shown that illuminating an optically thin MEMS device within a laser interference field may lead to self-oscillations, termed limit cycle oscillations (LCOs), in the absence of any external periodic forcing. These large amplitude vibrations only occur when the unmodulated laser power is above a critical value [7]. Thus interferometric transduction can drive self-oscillation without needing an independent periodic drive signal nor additional device layers, making it a promising technique for enabling low cost sensing and signal processing applications. Such applications however, require devices with highly stable, possibly tunable frequencies. MEMS oscillators transduced in this way have shown a high level of frequency noise [142] which could be problematic to their adoption in such applications.

Naturally occurring feedback oscillations have also been observed to occur due to thermo-mechanical feedback in satellites [124] as well as due to aeroelastic feedback in airplanes [26, 25], and hydrodynamic bearings [83], phenomena which are referred to as “thermal-flutter,” “aeroelastic-flutter,” and “oil-whip”

respectively. Limit cycle oscillation has also recently been proposed as an energy harvesting technique for thermal-flutter [90] and aeroelastic-flutter [14, 27]. Feedback oscillations have also been produced in MEMS using active electrostatic [37, 36] or optical [141] feedback to drive self-oscillation.

The first portion of this dissertation is organized around three experimental studies, spread out over two chapters. After fabricating singly-supported (cantilever) and doubly-supported (bridge) MEMS devices, and building an experimental apparatus to drive and detection their motion, we:

- Excited noisy LCOs by illuminating them within a laser interference field in "Transition to Limit Cycle Oscillation"
- Tuned the limit cycle frequency by varying the laser power in "Frequency Tuning"
- Stabilized the limit cycle frequency using an external drive in "Entrainment"

The final Chapter, 4, is devoted to understanding the causes of limit cycle oscillation in our devices, and the far from equilibrium dynamics.

In the remainder of *this* chapter we broadly present the theoretical underpinnings relevant to each experimental study and review past work in the area. First, we give an overview of the theory of limit cycles, and discuss past work measuring and modeling their onset in optically actuated devices. We also discuss what our motivation for this work was. We give a brief outline of our experimental results specific to the transition to LCO and our modeling conclusion. Next we give an overview of nonlinear oscillations, and how nonlinearities lead to frequency tuning in our MEMS devices when the laser power is changed. We

also discuss prior efforts to tune the frequency of MEMS devices, and how tunability in our devices leads to frequency noise. Finally, we discuss the theory of entrainment of limit cycles, and how it is used to tune and stabilize noisy LCOs in our devices.

Chapter 2 gives specific details on how our beams were fabricated, as well as material and geometric parameters relating to devices fabricated. Experimental results for each of the three studies are presented and discussed in Chapter 3. Chapter 4 is devoted to theoretical analysis and modeling of limit cycle oscillations.

This dissertation is intended to be a written record of research performed, but also as a guidebook for future researchers working the experimental setup used. As such, copious details on device fabrication as well as setup procedures and care is given in Chapter 2 in the hope that it will streamline the work of future students in the lab.

1.2 Background - Transition to Limit Cycle Oscillation, Modeling and Analysis

Langdon and Dowe [67] first demonstrated interferometrically transduced self-oscillation in a MEMS device. They showed that an optically thin aluminized polyester beam suspended over a reflective substrate sets up a Fabry-Pérot interferometer which couples absorption in the beam to deflection of it. If illuminated with a continuous wave (CW) unmodulated laser, the beam bent statically for low laser power, but for high enough power ($P > P_{Hopf}$) the beam began to

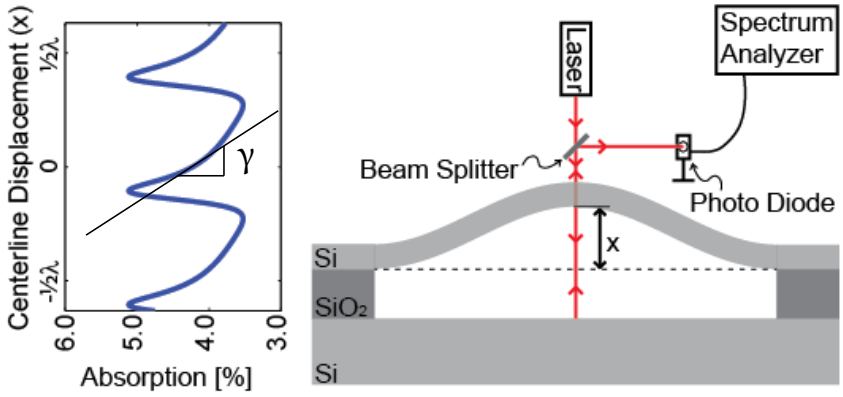

Figure 1.1: Diagram of basic experimental setup used to excite LCOs and measure their motion. The absorption contrast, γ for zero initial displacement is change in absorption per unit of beam deflection.

self-oscillate[1].

Oscillation of the device through the interference field also modulates the intensity of reflected light which may be measured and analyzed to determine the motion [67, 117, 17]. Although researchers use different specific experimental setups, in a typical experiment, samples are mounted in a vacuum chamber to reduce viscous damping, and a CW laser is focused perpendicularly on the center of the beam. The reflected signal is measured with a high speed photodiode and analyzed on a spectrum analyzer (see Figure 1.1). Such experiments [46, 7] have shown the existence of hysteresis: i.e. once the laser power reaches P_{Hopf} and the device begins to self-oscillate, it will continue to oscillate as the laser power is reduced until a lower power $P_{SNBC} < P_{Hopf}$ at which point the vibration ceases [2].

[1] In the terminology of dynamical systems, a "Hopf bifurcation" is a type of transition from steady state to periodic motion, and is the phenomenon responsible for the term used for the critical power, P_{Hopf}. This terminology is that of Zalalutdinov et al. [144], not that of Langdon and Dowe.

[2] Once again the terminology comes from dynamical systems - here Saddle Node Bifurcation of Cycles, where a stable and unstable limit cycle coalesce or divide. This bifurcation is sometimes referred to as a fold of limit cycles due to its shape on a bifurcation diagram.

Two laser systems have also been employed where one high power laser is used to drive, and a second low power laser is used to measure oscillations [98, 35, 46]. The measuring laser may also be introduced at an oblique angle and collected in a position sensitive photodiode to determine displacement of the device from deflection of the laser [21]. Such devices are often optically thin and the interferometer is formed between the device and underlying substrate. In addition, devices have been coated with thin layers of reflective material and illuminated with a laser introduced via an optical fiber or through a partially transparent mirror such that the interferometer is set up between the device and the fibre free end or mirror [67, 118, 46]. This setup allows for additional modification of the optical cavity by displacing the fiber/mirror. Stokes et al. [117] show that when varying the cavity length, the amplitude of oscillation is periodic in roughly $\frac{\lambda}{2}$. Hane et al. [46] later confirmed this, and further showed that the amplitude of oscillation is limited to $\frac{\lambda}{2}$.

Theories of optically transduced self-oscillation credit the feedback between device displacement and optical absorption/reflection for causing oscillations, however differing claims exist about the mechanism by which changes to the absorption/reflection are coupled to device displacement. Various authors have claimed that electronic stress, radiation pressure, or photothermal stress alone matter, with some claiming that many of these effects compete in the same device. Significant work on the mechanism of optical activation exists in the field of optically driven oscillation, where the excitation laser is externally modulated. This work is reviewed below along with models and analysis of when unmodulated illumination can lead to self-oscillation.

For beams made from semiconducting materials, electronic stress may be an important consideration. When ionizing radiation strikes a semiconductor, generation of electron-hole pairs creates electronic stress. Stearns et al. first examined this effect in doped silicon, calculating that the electronic strain was 2.6 times greater and of opposite sign than photothermal stress in his p-doped silicon samples excited with an Argon laser (λ = 514 nm) [116]. Prak et al. performed similar experiments with similar results [98]. Pitcher et al. studied the effects of surface coatings on the amplitude of vibration of boron doped silicon resonators driven with an intensity modulated laser at wavelength λ = 850 nm, suggesting that electronic stress caused a nonlinear relationship between thickness of surface coating and vibration amplitude [96]. Limited work exists on undoped silicon. Datskos et al. studied undoped silicon cantilevers with a thin aluminum coating using diode lasers with λ = 780 nm and λ = 1300 nm [21]. They calculate that when their devices are excited at λ = 780 nm the electronic stress is 3.7 times larger than photothermal stress. They also show that electronic stress acts much faster than thermal effects, and in general depends on the free charge carrier density (i.e. doping), and wavelength of excitation. They suggest that excitation with photon energies above the bandgap (i.e. wavelengths below λ < 1100 nm for Si) are dominated by electronic stress, and energies below the bandgap (i.e. λ > 1100 nm for Si) are dominated by photothermal stress. However, Lammerink et al. have studied optically driven silicon beams with and without surface coatings, and found no indication of electronic stress [66].

For high finesse optical cavities with highly reflective beams, radiation pressure has been shown to dominate. Dorsel et al. first observed bi-stability in a MEMS beam forming a Fabry-Pérot interferometer in 1983, attributing it to

spatially periodic radiation pressure caused by periodicity in the interference field. In 1996, in the same issue of the journal *Nature*, Arcizet et al. [4] and Gigan et al. [43] fabricated MEMS devices for negative feedback using radiation pressure in order to demonstrate cooling due to feedback damping. In order to avoid absorption in the beam highly reflective coatings ($R \geq 99\%$) were applied to the beam surface. Gigan et al. suggested that 50-70% of the forcing in their devices was due to radiation pressure and the rest was photothermal, while Arcizet et al. suggest that all of the forcing in their devices was due to radiation pressure. We note that Metzger et al. had previously demonstrated feedback cooling and attributed it to photothermal effects [79]. Later Pruessner et al. fabricated MEMS beams for in-plane deflection, excited via an on-chip wave guide. Distributed Bragg reflectors were used to create sharply peaked transmission spectra [99], i.e. high optical finesse. Experimental results indicate the presence of both radiation pressure and photothermal forces. The use of waveguides, and transverse illumination of toroidal resonators has also been demonstrated in [61, 105, 105, 71], where coupling between optical and mechanical modes is observed.

It is also worth mentioning the work of Zook et al. [56] who fabricated enclosed optically thin microbeams suspended above embedded photodiodes. Movement of the beam through the interference field modulated the amount of light absorbed on the photodiode below, causing a changing charge concentration, thus inducing an electrostatic force which drove deflection. This novel scheme results in the lowest threshold power for self-oscillation known to this author of $1\mu W$, which is an order of magnitude less than the second lowest of $\simeq 10\mu W$ measured by Kippenberg et al. [61].

Unless devices are doped to increase electronic stress, or surface coated for high reflectivity to reduce absorption and promote radiation pressure, photothermal effects have been shown to dominate. Early work focused on beams with partially transparent thin metal coatings on their top surface. Such coatings increased the reflectivity needed to detect device motion, though not by enough to eliminate absorption. Coatings also confined absorption heating to the device top surface allowing for through thickness gradients (see Sections 4.4 and 4.5). If the coating is thick enough to add structural rigidity, these through thickness thermal gradients are amplified by differing coefficients of thermal expansion (i.e. the "bi-metallic effect") to drive deformation. Unfortunately, coatings also add material damping.

Langdon and Dowe [67] studied thick (25-50μm) beams with thin (50nm) surface coatings of aluminum. They assume that the laser power is absorbed near the top surface of the beam causing vertical thermal gradients throughout the beam and deflection due to resultant bending moments. The feedback gain, they claim, is equal to the product of three quantities: the laser power, the beam displacement per unit laser power, and the change in laser transmission percentage per unit displacement. The feedback gain, they suggest, must be greater than one to ensure self-oscillation.

Churenkov [19] considered the case where surface coatings are thick enough to add mechanical rigidity and assumed that bending moments in such beams were due to the bi-metallic effect. He then uses energy methods to derive formulae for the minimum power needed for self-oscillation. Hane assumes, like Langdon and Dowe, that optical coatings are thin and derives a formula for the beam dynamics which explains both the threshold laser power for self-

oscillation, and the saturation of vibration amplitude at $\frac{d}{2}$ [45].

However, neither Churenkov's, Hane's, nor Langdon and Dowe's analyses are applicable to the uncoated optically thin beams studied in [7, 144]. For uncoated beams there is no bi-metallic effect. For optically thin beams, absorption occurs throughout the beam thickness (see Section 4.4) and the combination of high aspect ratios and high thermal conductivity ensures negligible vertical thermal gradients in the beam (see Section 4.1). In addition, energy methods cannot capture hysteresis loops which are experimentally observed [7].

Further work was done by Kozel et al., who assumed that the interference cavity was tuned such that the beam was at a peak in the reflection/absorption [63]. In such a case, movement through the interference field at the beams natural frequency, f_o, produced a temperature modulation at $2f_o$, which he assumes drives self-oscillation through parametric amplification. A condition for self-oscillation is derived using energy methods. Note that although parametric amplification could sustain self-oscillations, it could not be responsible for the instability that gives rise to self-oscillation (a local phenomenon). In order for displacement at f_o to produce temperature modulation at $2f_o$, the beam must move through a peak in the interference field. Thus in order for parametric forcing to cause an instability which leads to self-oscillation, the initial beam deflection has to be *exactly* at a peak in the reflection/absorption, or thermal noise has to be large enough to drive the beam through the peak.

Others have assumed periodic surface heating of doubly- and singly-supported beams, solved for the temperature distribution, and analyzed deflection due to thermal stress waves. Fatah studied thermally thin doubly-supported beams, and related their out-of-plane deflection to their average tem-

perature increase by assuming that the device bends into a shallow arch, and setting the strain to due change in length equal to the thermal strain due to heating [35]. Lammerink et al. studied singly supported beams, relating out-of-plane deflection to through thickness temperature gradients in the device [66]. Finally, Ilic et al. used finite element analysis (FEA) to show that deformation in cantilevers is confined to a small region near the anchor support [55, 54]. Fatah and Ilic then give an amplitude of driven oscillation in doubly- and singly supported beams respectively, which is directly proportional to the amplitude of the modulated laser power. However, these analyses of externally modulated optical drive fail to capture the essential property of LCOs - that oscillation begins only after the unmodulated laser power reaches a threshold value.

Other observations of self-oscillation have been reported with little modeling or analysis of the onset. Stokes et al. observed self-oscillation in gold coated silicon dioxide resonators and attributed it to photothermal effects though no model or analysis was given [118, 117]. Later work by Zalalutdinov et al. showed self-oscillation in CW laser illuminated disks [145]. Self-oscillation was also demonstrated in domes using positive feedback to feed the measured displacement back into the laser drive power with a variable phase lag [141]. Work by Sekaric et al. demonstrated increases to quality factors for CW laser illuminated paddle oscillators operating in air, as well as self oscillation at high laser powers [112].

Many parameter models built around the absorption induced thermal stress which display hysteresis have been used to accurately predict threshold powers for self oscillation in specific devices of various geometries such as disks, domes, paddles and beams [7, 144, 145, 45]. These models show that the thresh-

old power for self-oscillation in MEMS devices depends on the direct feedback between static heating and displacement, yet it is unclear in general what mechanism causes the displacement. In addition, model parameters have not been systematically studied, nor tied to the physical mechanisms underlying deformation. Such analysis would support design questions such as - *How does one construct a MEMS resonator to have a low threshold power for self-oscillation?*

In order to better understand the causes of optically transduced LCO, and build better models to predict its onset, we focus our attention on simple beams. In this dissertation, we fabricate singly- and doubly-supported beams and measure the critical power for self oscillation (Section 3.1). Results show that location within the interference field is important in determining whether feedback inhibits or enables self-oscillation. In Chapter 4 the mechanism behind thermo-mechanical coupling is studied in detail. Analysis of the absorption, reflection and transmission of monochromatic light from a thin film stack indicates that laser heating is not confined to the top surface. The finite element method (FEM) is used to show that deflection due to heating comes from a combination of thermal gradients and compressive stresses at the beam's support. Finally, we present an almost parameter free model which suggests that barely post-buckled beams should have the lowest threshold power for self-oscillation. Numerical continuation of the model equation suggests the presence of multiple stable limit cycles, periodically spaced in amplitude due to periodicity in the interference field.

1.3 Background - Frequency Tuning

Applications such as filtering may require long term frequency stability, or short term frequency control. In spite of fabrication process control the frequency between nominally identical resonators on a single wafer will vary. Temperature fluctuations during use may cause short term frequency fluctuations [126], and ageing or surface contamination of devices [94] can lead to permanent frequency offsets. For this reason, significant attention has been drawn to tuning of MEMS resonant frequencies after fabrication.

Techniques to irreversibly modify devices post-release include laser trimming [41], ion milling [123], and laser annealing [6], though simple techniques to induce non-permanent frequency shifts are particularly desirable. A number of such techniques have been proposed and may be categorized as techniques which :

- Introduce membrane (i.e. in-plane) tension or compression in the device
- Introduce an electrostatic linear stiffness of variable magnitude
- Introduce an electrostatic bias which shifts the steady state configuration and changes the local curvature of the energy potential (i.e. stiffness)

The first technique is applicable to all devices supporting membrane stress regardless of the actuation technique. The second two techniques are specific to electrostatically driven MEMS. Below, we give an overview of frequency tuning through membrane stress, applicable to the doubly-supported MEMS beams we studied. We describe the effects of membrane stress, give equations of motion, and define terms such as “linear frequency/stiffness” and “nonlinear

frequency/stiffness" which are used in later sections. Finally, we review prior work in frequency tuning of MEMS, including electrostatic techniques, and give an overview of our results.

Theory: Linear Oscillations

Though deformation in beams are described by partial differential equations (PDEs) governed by continuum mechanics, various types of model reduction are often used to obtain approximate equations. Most often, one assumes small displacement and rotation to obtain the linear (PDEs) of Euler-Bernoulli beam theory valid for small deformation of slender beams [42]. Further simplification may be obtained by assuming first mode vibration, and using the Galerkin or Rayleigh-Ritz method to minimize the projection error [65]. This process reduces the governing PDE to an ordinary differential equation (ODE) on the centerline displacement, x, (see Figure 1.1). The resulting equation is that of a simple harmonic oscillator:

$$m\ddot{x} + c\dot{x} + kx = 0 \tag{1.1}$$

where the modal mass, m, modal stiffness, k, and damping constant, c, depend on beam geometry, boundary conditions, and damping model. A forcing term, $F\cos(\omega_d t)$, may be included on the right-hand side for modeling driven oscillation.

The free oscillation of (1.1) is described by a damped sinusoid decaying inside an exponential envelope with time constant $\tau = \frac{Q}{\pi f}$, where $f = 2\pi\sqrt{\frac{k}{m}}$ is the resonant frequency, and Q is the quality factor[3]. The quality factor is obtained

[3]No distinction is made between the damped and undamped frequency since $Q >> 1$ is an

experimentally from $Q \simeq \frac{f}{\Delta f}$, where Δf is the frequency interval between points on the resonance curve where the amplitude is down by $\frac{1}{\sqrt{2}}$ from its maximum value (see Figure 1.2). Note that the principle of superposition holds for equation (1.1), s.t. if $A_1 \cos(\omega t)$ and $A_2 \cos(\omega t)$ are solutions then $(A_1 + A_2)\cos(\omega t)$ is also a solution. Thus, amplitude is independent of frequency.

Theory: Nonlinear Stiffness and Nonlinear Oscillations

Equation (1.1) is valid for small deformation of slender beams, and neglects the effects of non-linearities such as shear deformation, rotary inertia, warping, static deformation, etc. which are important for large deformation or high vibration modes. A good overview of nonlinear beam theories may be found in the dissertation of Malatkar [76]. Other notable works on large amplitude vibrations of, or stress effects on doubly-supported beams include those by Eisley [29, 28], Evensen [30], Atluri [5], Bouwstra et al. [11], Nayfeh et al. [84], and Lestari et al. [70].

For devices supporting in-plane tension, midplane stretching is the dominant source of non-linearity [140] which may be accounted for using Timoshenko beam theory [129, 130, 39]. Including the effect of midplane stretching, neglecting damping, and non-dimensionalizing time we get [29]:

$$\ddot{x} + k\left(1 - \frac{\sigma}{\sigma_b}\right)x + k_3 x^3 = 0;\ k, k_3 > 0 \tag{1.2}$$

where the total stiffness depends on the unstressed linear stiffness, k, ratio of the compressive stress, σ, to the buckling load, σ_b, and includes a nonlinear term, $k_3 x^3$. See Section 4.3 for a detailed derivation.

appropriate assumption for the devices we study.

Assuming that the beam is unbuckled (i.e. $\sigma < \sigma_b$) then $x_{eq} = 0$ is the only equilibrium solution to (1.2) and is a stable equilibrium. The "linear stiffness" or the slope of tangent to the load curve at $x = x_{eq} = 0$ is simply the coefficient on x, $k\left(1 - \frac{\sigma}{\sigma_b}\right)$, and the (cubic) "nonlinear stiffness" is k_3. For small amplitude oscillations the nonlinear stiffness term may be ignored leading to a "linear frequency" (i.e. frequency of small oscillation), coming from the linear stiffness. For a doubly-supported beam with no pre-stress, the amplitude of oscillation at which non-linear effects become important is $A_{crit} \approx \frac{2t}{\sqrt{0.528Q(1-\nu)^2}}$ where t is the beam thickness, Q the quality factor, and ν the Poisson's ratio [128]. Note that there are differing treatments of the critical amplitude by Kaajakari et al. [59] and Postma et al. [97]. At large amplitudes, the k_3x^3 term adds stiffness to the system (since $k_3 > 0$), increasing the frequency of oscillation (see Figure 1.2). This phenomenon is termed an amplitude-frequency relationship, and the curve in frequency-amplitude space which describes it is termed the backbone curve [101]. This amplitude dependent frequency of oscillation we term the "nonlinear frequency." When the frequency increases with amplitude ($k_3 > 0$) the oscillator called "amplitude hardening," while opposite ($k_3 < 0$) is termed "amplitude softening."

Assuming that the beam is buckled (i.e. $\sigma > \sigma_b$), then $x = 0$ is no longer a stable equilibrium solution, and the beam will be in one of two buckled states, $x_{eq} = \pm x_b$. A change of variables $\tilde{x} = x - x_b$ is then used to pull the equilibrium solution back to zero [28]. Mixed terms in the expansion of the cubic nonlinearity produce a quadratic nonlinearity:

$$\ddot{\tilde{x}} + c_1(\sigma, \sigma_b)\tilde{x} + c_2\tilde{x}^2 + c_3\tilde{x}^3 = 0;\ c_1, c_2, c_3 > 0 \tag{1.3}$$

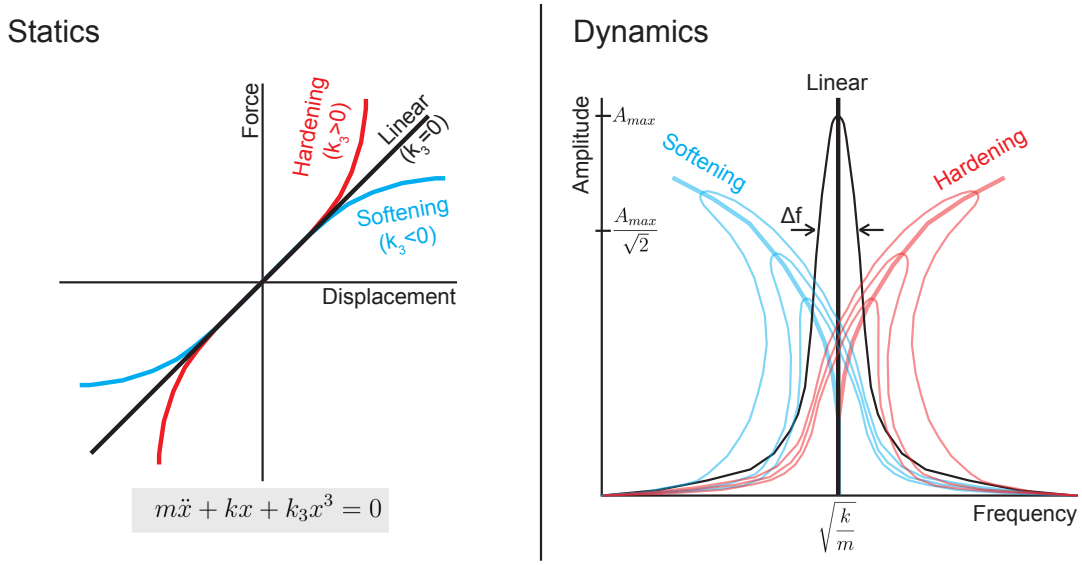

Figure 1.2: Load curve (left) and resonance curves (right) for the cubically nonlinear oscillator $m\ddot{x} + kx + k_3x^3 = 0$. The thick lines on the right are the backbone curves - i.e. relationship between amplitude and frequency in the absence of forcing or damping. Note that in the linear model, amplitude-frequency relationship is vertical as suggested by the superposition principal. The thinner lines show resonant responses for a fixed damping level with varying levels of forcing. Note that for the nonlinear oscillators ($k_3 \neq 0$), at decreasing drive amplitudes the resonant response is increasingly linear. The width of the linear resonant curve Δf, used to calculate Q is also indicated.

A quadratic non-linearity breaks the symmetry, and leads to amplitude softening regardless of the sign of c_2 [51, 80]. Competition or collaboration between quadratic softening and cubic hardening or softening exists in oscillators having both quadratic and cubic nonlinearities. The linear stiffness, here denoted c_1, is zero at the buckling load and increases monotonically with compressive stress thereafter [11]. See Appendix B for a detailed discussion of amplitude-softening/hardening, and linear frequency of oscillation as it relates to stress levels in doubly-supported beams.

Literature Review

Thornton et al. first demonstrated that changes in ambient temperature would tune the frequency of MEMS bridges in 1986 [125, 126, 117]. Zook et al. later used tension to deliberately tune the linear frequency of a MEMS beam in 1991 [148], bending the chip on which devices were fabricated to add stress in the device layer [119]. Others have locally heated beams to induce thermal stress and modify the stiffness via the temperature dependent Young's modulus, giving tunings of up to 10% [88, 104, 58, 108]. Zhang et al. demonstrated $< 1\%$ tunability in optically driven (i.e. externally modulated) MEMS beams by changing the median laser power [146].

Stress has also been induced electrostatically [138, 147] giving frequency shifts up to 98% in specially designed resonators. Electrostatic devices have been tuned using "fringing field actuators" [3], or for parallel plate actuators by increase the DC bias to change the gap, making use of the $\frac{1}{x^2}$ force law [138, 64]. Comb-drive resonators have been tuned by fabrication of an additional tuning comb whose overlap varies with displacement due to linearly varied finger lengths [68], or out-of-plane steps [82]. A DC bias voltage across these combs creates an electrical linear stiffness in proportion to the applied bias voltage. One author has even suggested using pull-in as a means to increase the resonant-frequency [60], though does not account for contact forces which typically make pull-in irreversible.

Finally, we note the work done to tune nonlinearity in MEMS resonators. Yao et al. first demonstrated that increasing the DC bias of an electrostatically driven resonator could change a resonator from hardening to softening [138]. Kozinsky et al. later demonstrated the same [64], attributing the change to com-

petition between the intrinsic mechanical hardening and the electrostatic softening. DeMartini et al. also demonstrated linear and nonlinear tuning in parametrically excited MEMS [22] by varying the DC bias and modulation depth. Lastly, Adams et al. demonstrated independent tuning of linear and nonlinear stiffness with two "fringing field actuators" [2].

In this dissertation, we examine frequency tuning of optically self-excited oscillators. Increasing the laser power past P_{Hopf} is seen to increase the linear resonant frequency through added compressive thermal stresses. At the same time, the resulting increase in amplitude of oscillations adds nonlinear frequency tuning for doubly-supported resonators. The competition between these two effects results in a wide range of tuning relationships and also maps laser power instability into frequency jitter (see [132] for a treatment of nonlinearity and frequency noise in optical MEMS). Singly-supported devices which do not support membrane stress show little tunability and low jitter.

It is expected that nonlinear effects in optically transduced MEMS will become more important as the push for high frequency devices shrinks device dimensions and places more emphasis on devices supporting membrane stress. As devices become smaller, the $\frac{\lambda}{2}$ amplitude saturation of optically transduced LCOs (see Section 1.2) will become an increasingly large proportion of device thickness and length, making large amplitude effects increasingly relevant.

1.4 Background - Frequency Entrainment

When an LC oscillator operating with frequency, f_{LCO}, is externally driven with harmonic signal $A_D \cos(2\pi f_D t)$, having drive frequency, f_D, and drive amplitude,

A_D, the type of response depends on the strength of forcing and frequency detuning, $f_D - f_{LCO}$. For low drive amplitudes with drive frequencies well separated from f_{LCO}, the oscillator is unaffected by the drive. The frequency content of the motion is mostly at f_{LCO} with a small component at f_D. For high drive amplitudes at frequencies close to f_{LCO}, the frequency of the limit cycle is shifted to respond only at f_D [86, 101]. The limit cycle is then said to be 1:1 entrained or locked, where 1:1 indicates the drive:response frequency ratio. Entrainment may also occur when the drive frequency is near an integer multiple or demultiple (fraction) of the limit cycle frequency, i.e. n:1 subharmonic entrainment at $f_D \approx n \times f_{LCO}$ or 1:n superharmonic entrainment at $f_D \approx \frac{1}{n} \times f_{LCO}$, where n is an integer [4] [86, 101]. To illustrate, if $f_D = 0.33$ MHz and $f_{LCO} = 1$ MHz, then for A_D great enough, the limit cycle will be 1:3 superharmonically entrained to respond at 0.99 MHz. Similarly, if $f_D = 3.03$ MHz and $f_{LCO} = 1$ MHz, then for A_D great enough, the limit cycle will be 3:1 subharmonically entrained to respond at 1.01 MHz. The phenomenon of entrainment is also referred to as "phase-locking" since when entrained the phase of the response is locked to the phase of the drive.

Typical analysis of entrainment indicates the presence of sharply defined V-shaped regions of entrainment in $f_D - A_D$ parameter space emanating from $(f_{LCO}, 0)$ [101]. In this picture, for a fixed (f_D, A_D) we are either inside the V and the limit cycle is entrained or we are outside the V and the limit cycle is not entrained. In addition, no matter how small the drive amplitude, A_D, we can choose a drive frequency, f_D, sufficiently close to f_{LCO} in order to guarantee locking.

[4] The term "primary" entrainment is sometimes used to distinguish 1:1 entrainment from sub- or superharmonic entrainment

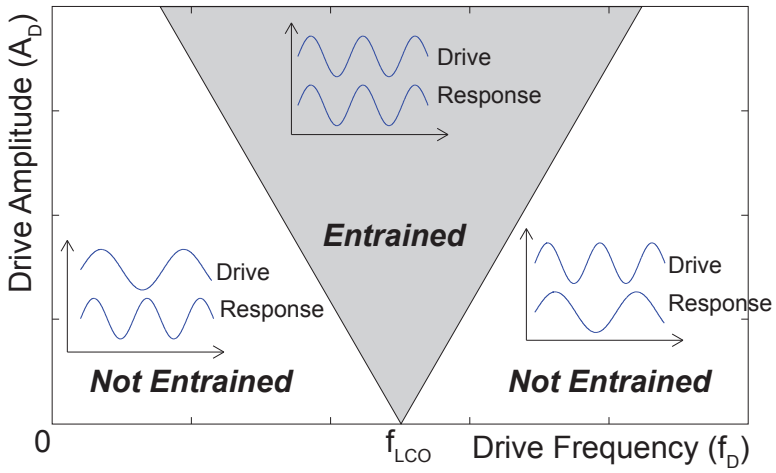

Figure 1.3: Sketch of $f_D - A_D$ parameter space for typical entrainment scenario.

Observation of subharmonic entrainment in an electrical circuit led Van der Pol to call the phenomenon "frequency demultiplication" since the limit cycle response was at a demultiple, or fraction of the drive frequency [134]. Van der Pol studied entrainment of limit cycle oscillators exhibiting relaxation oscillation, characterized by a slow asymptotic behavior followed by a sudden jump [101]. He demonstrated subharmonic entrainment up to 200:1, with results published up to 40:1 [134].

Zalalutdinov et al. demonstrated 1:1 and 2:1 entrainment in a MEMS pillar [142], illustrating how entrainment could be used to reduce the frequency noise[5] of a LCO from $\frac{\Delta f}{f} \sim 10^{-3}$ to that of the highly stable drive with $\frac{\Delta f}{f} \sim 10^{-9}$. Inertial drive was used to obtain 1:1 entrainment, and 2:1 entrainment was obtained by amplitude modulation of the CW laser power at a frequency near 2 f_{LCO} (i.e. parametric forcing). Higher order subharmonic entrainment was not seen, nor

[5]Frequency noise in the system is seen as sporadic motion of the resonant peak. Δf in this context is the expected deviation in a set of multiple measurements of the frequency, and is unrelated to the width of the resonant peak used in calculating the quality factor.

was superharmonic entrainment.

Feng et al. demonstrated 1:2 superharmonic entrainment in a piezoelectric system - beams with first mode frequencies separated by a factor of roughly two were co-fabricated on top of individual piezoelectric actuators with a mechanical web connecting the beams [36]. Self-oscillation was established in the higher frequency beam ($f_{LCO} \sim 296$ kHz) by feeding the measured displacement into the drive. The neighboring beam was then driven near it's resonant frequency ($f_R \sim 145$ kHz). Entrainment was seen with drive frequencies in the range of 147.6 to 147.7 kHz.

Shim et al. demonstrated sub- and superharmonic resonance[6] in mechanically coupled MEMS beams [114]. Two doubly-supported beams with roughly equal length were co-fabricated with a shorter beam coupling them at their midline. One beam was driven magnetomotively and the displacement of the other beam measured. Superharmonic resonance was measured up to 1:7 in addition to other resonances [7]. Unlike the work of Van der Pol [134], Zalalutdinov [142], and Feng [36], Shim et al. do not investigate a self-oscillating system.

Analysis has also been performed by Pandey et al. [91], who built a thermomechanical model of the devices studied in [142]. Direct numerical integration of the model was shown to accurately predict the measured regions of entrainment. A slow-flow analysis is presented in [92] and the effects of parametric versus direct forcing are explored in [93].

[6] Sub- and superharmonic "resonance" is a response at the resonant frequency due to forcing at an integer multiple or fraction of it.

[7] Note Shim et al. reference the drive frequency with respect to the response frequency, and thus refer to forcing of the beam at a frequency below it's natural frequency as "subharmonic driving". We adopt the opposite convention in order to be consistent with prior usage [134, 101, 86, 47]. They also refer to their results as frequency entrainment. We reserve the use of the work "entrainment" to refer to self-resonant systems in order to be consistent with the same authors cited above.

In this dissertation we examine entrainment as a means to stabilize a noisy limit cycle and tune it's frequency. We show that for noisy limit cycle oscillators, entrainment is a inherently statistical phenomenon. For low forcing amplitudes, the limit cycle is seen to transition in and out of entrainment, and a minimum strength of forcing is required to obtain persistent "strong" locking. We examine hysteresis in the region of locking as a function of the operating point on the backbone curve, showing that hysteresis is most prominent at the base of the backbone curve. Finally, we examine sub- and superharmonic entrainment in doubly-supported and singly-supported beams. Superharmonic entrainment of orders from 1:2 to 1:7 and subharmonic entrainment of 2:1 and 3:1 are seen a doubly-supported beam, while no sub- or superharmonic entrainment is seen in singly-supported beams. Results suggest that the strength of the nonlinearity is responsible for enabling high order sub- and superharmonic entrainment.

CHAPTER 2

EXPERIMENTAL SETUP AND PROCEDURES

2.1 Device Fabrication

Previous work [7, 144] had shown that a large negative absorption contrast (see Figure 1.1) leads to low power self-oscillation. Thus, silicon-on-insulator (SOI) wafers were selected with device and oxide thickness chosen in order to optimize the absorption contrast, γ. Analysis of several commercially available wafers was performed using the code presented in [111] and optical parameters listed in Section 2.2.1 to model reflection, transmission and absorption from a thin film stack. The nominal wafer device layer thickness was used as the beam thickness, the buffered oxide layer thickness as the undeflected gap to substrate, and the wafer handle was modeled as semi-infinite.

Ultimately, SOITECH UNIBOND G6P-060-01 150mm wafers were ordered which had a *nominally* 205nm thick (100) Si device layer, 400nm thick SiO_2 oxide layer and 525μm thick Si handle. The computed absorption as a function of deflection is shown in Figure 1.1, and has zero deflection absorption of $\alpha = 0.0399$ and an absorption contrast of $\gamma = -5.06 \times 10^{-5} \frac{1}{nm}$. Note that final devices ended up having differing values of α, γ, due to device thinning in the release step, and stress related initial deformations discussed in subsequent sections. In addition, variation in the initial device layer thickness and oxide layer thickness was present. The batch of wafers from which we ordered had quoted specifications of 205.9 and 399.2 nm for the device and oxide layer thickness with 6σ variation of 16.7 and 2.2 nm respectively.

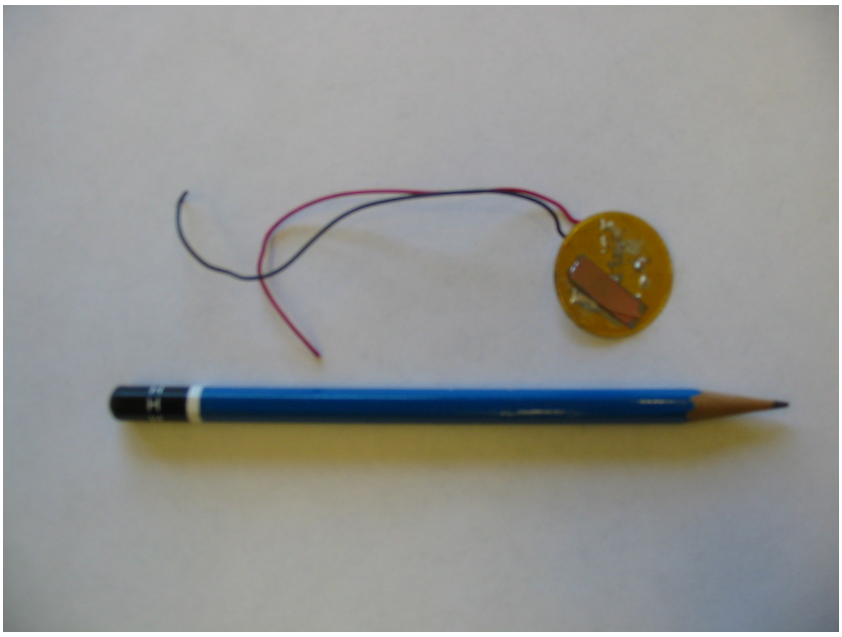

Figure 2.1: Picture of chip mounted to piezo drive (see Section 2.4.1).

Due to the cost and size of these wafers, we chipped them into $\frac{1}{4}$" $\times$ $\frac{3}{4}$" pieces before processing (see Figure 2.1). A protective coating of SPR 955 photoresist (PR) was spun onto the topside of a wafer which was then chipped using a KS 7100 dicing saw. The long side of the chips was oriented along the wafer flat in order to enable later alignment of beams to Si crystallographic planes - see Figure 2.2 for a sketch of the chip and beam orientation. After dicing we noticed that the protective coating had peeled off in areas due to poor adhesion. However, no damage to the device layer was visible during inspection. Finally, the protective coating was stripped from chips in a hot bath to prepare them for lithographic fabrication.

Due to our relatively large feature size, we elected to use photolithography as opposed to electron-beam lithography to define our devices. We selected 5$\times$ projection lithography with a GCA 6300 DSW stepper due to its high depth of focus. Our design process required a single 6" mask which was written using

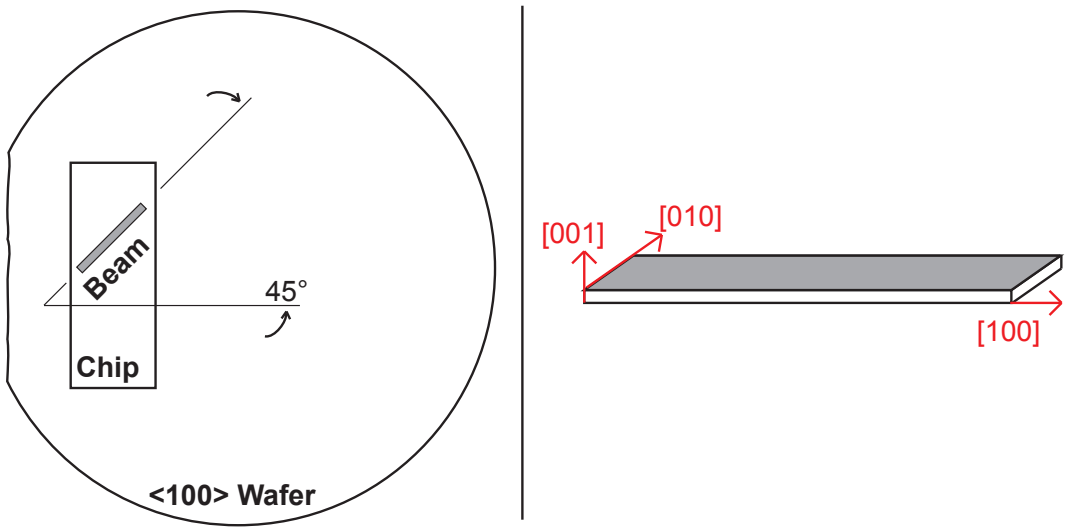

Figure 2.2: Sketch of orientation of chip with respect to wafer, beams with respect to chip, and most importantly beams with respect to Si crystal directions.

a Mann PG3600 pattern generator. Early chips were fabricated from a mask having doubly-supported and singly-supported beams fabricated side-by side. However due to the possibility of mode coupling, and the beams' close proximity with respect to the laser spot size, it was difficult to analyze the motion of single beams fabricated from that mask. A second mask was generated with larger inter-device separation, and all data presented here comes from devices made with the second mask.

Resist uniformity was a challenge when working with small pieces and resulted in low yield. Several different resists, spin speeds, and spin times were tested in order to maximize uniformity in the resist thickness. Resist thickness was measured at 15 points on a single chip using the FilMetrics F40 optical measurement system (see Section 2.2 for details). Best uniformity was obtained using P20 to promote adhesion, followed by Shipley 1813 resist spun for 30 sec at

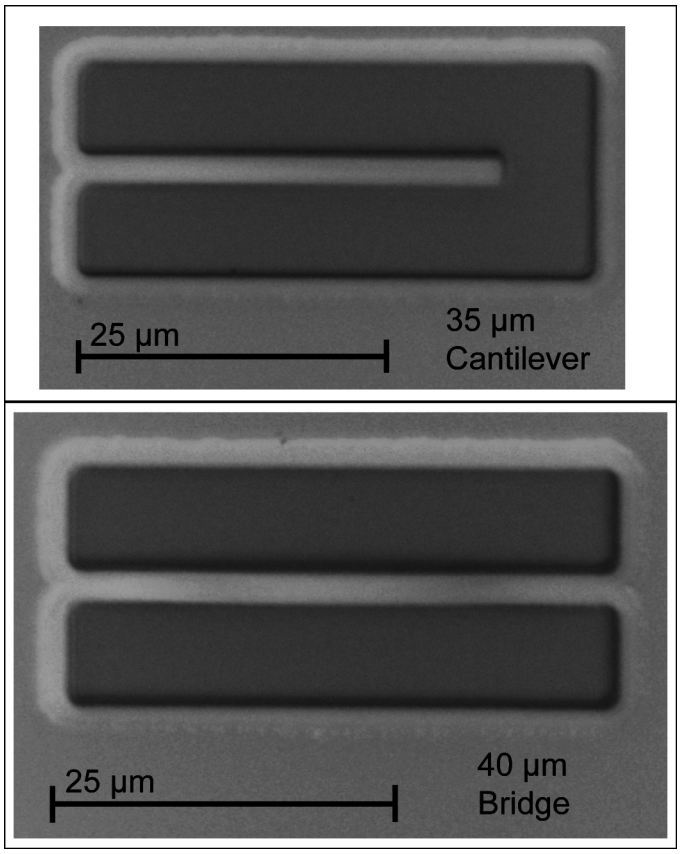

Figure 2.3: Optical microscopy image of 35μm long singly-supported and 40μm long doubly-supported devices.

3000 RPM, and finally soft-baking for 60 sec at 115°C. This process resulted in a PR thickness of 1425 ± 60 nm which was thick enough to withstand later etching. Even with this level of uniformity, the variation in thickness is greater than the 40-50 nm peak-trough distance in the dosage swing curve.

Small pieces also introduced challenges to photolithography. In order to expose chips in the stepper, a plastic sheet was cut to fit the vacuum chuck and a small hole cut in the appropriate location for the chip. The mask was aligned to the long edge of the chip, and then shifted up before exposing. In this way we could align our devices to the chip with an error of $\Delta\theta < 0.1°$. Including misalignment during dicing we expect total alignment errors of our beams to

the Si crystallographic planes of $< 1^{\circ}$. After exposure, chips were post-exposure baked for 60 sec at 115°C, and then developed in 300MIF for 60 sec.

An Oxford 81 plasma etcher was used to etch through the device layer, and part of the way through the underlaying oxide. A CF_4 process was used with 30 sccm flow rate at 40 mTorr pressure and 150 W power, for $\sim$ 8 min. Wet chemistry was used for the final release. Early chips were released using 6:1 Buffered Oxide Etch (BOE), which resulted in an unexpected $\sim$ 20 nm thinning of devices due to a slow, but measurable Si etch rate of $\sim 0.95 \frac{nm}{min}$ and a long total etch time of $\sim$ 16 minutes. Final chips were released using a 1:1 volume solution of water and 49% HF in water resulting in a $\sim$ 3:1 solution of H_20:HF. This chemistry gave a slower Si etch rate and faster SiO_2 etch rate, resulting in less device thinning. Device layer thickness was measured before and after release (see Section 2.2).

After release, chips were transferred to a container with 100% water, which was mostly dispensed and slowly refilled for 2 minutes to gently rinse the chip while keeping devices submerged. We observed the formation of small bubbles in the patterned area which may have contributed to stiction issues. Chips were then rinsed:

- Once in 3:1 H_2O:methanol
- Once in 1:1 H_2O:methanol
- Once in 1:3 H_2O:methanol
- Twice in 100% methanol

Finally, chips were transferred to the Tousimis Autosamdri 815-B for critical point drying. Stiction remained a significant problem for longer devices in spite

of critical point drying. Mild agitation during release and rinse seemed to be correlated with higher yield, though it is not clear if the impact was direct. In spite of best practices most $30\mu m$ and longer devices were stuck.

2.2 Device Characterization

2.2.1 Device Thickness and Material Properties

In addition to inspection using optical microscopy, several tools were used for metrology at various stages of the lithographic process. Of particular importance was the evaluation of device thickness which is critical in determining device frequency, buckling stress, and optical properties. This section describes the characterization of device thickness, and lists material properties used in subsequent analyses.

Validation of initial wafer film thickness was performed on a Woollam spectroscopic ellipsometer. Four points on the wafer were scanned starting at the wafer center and moving out towards the wafer flat with 1.5 cm spacing between points. The wafer was scanned at a 75° incident angle with wavelengths from 170 nm to 250 nm in 10 nm increments. Analysis of the reflected light was used to determine layer thicknesses, and results were within the specifications given by SOITECH.

Chip level thickness characterization was performed using the FilMetrics F40 optical measurement system. A film stack model was built using an Si handle and 399.2nm SiO_2 oxide layer followed by a Si device layer and SiO_2 native

oxide layer. Since the manufacturer's specifications for variation in oxide layer thickness were much smaller than the variation in device layer thickness, the oxide layer thickness was fixed in the model, and the device layer and native oxide thicknesses were used as two fitting parameters. FilMetrics only analyses normally incident light and is less accurate than the ellipsometer. In addition, measured device layer thicknesses were consistently 2-3 nm lower than both the manufacturer's specs and the measured ellipsometer data from an undiced wafer. This systematic error is likely due to differences between actual material optical properties and textbook values. Better results would be obtained by measuring the optical properties of our films directly using the ellipsometer, and using those properties in the FilMetrics analysis. In addition, film thickness is expected to vary according to location on the wafer. No effort was made to track a chip's original location from within a wafer, information which could have been useful.

Chip #	Pre-etch	Post-etch	Beam Thickness	Gap-to-Substrate
0	202.1 nm	183.4 nm	174.0 nm	408.5 nm
I	201.6 nm	200.8 nm	200.4 nm	399.6 nm
II	203.5 nm	199.6 nm	197.6 nm	401.1 nm

Table 2.1: Table of measured device layer thickness pre- and post-etch, and calculated final beam thickness and gap-to-substrate. BOE was used during the release etch of the first chip resulting in substantial device thinning.

Measurements of the pre- and post-etch device layer thicknesses on each chip were used to calculate final beam thickness. The silicon device layer was etched during the final release, at a very slow by measurable rate. Sections of unreleased device layer should only experience topside etching whereas beams should experience topside and partial bottom-side etching during the release process. In order to account for bottom-side etching, a material loss factor of 1.5

Material	ρ $[\frac{kg}{m^3}]$	ν	E [GPa]	α_T $[K^{-1}]$	k $[\frac{W}{m*K}]$	c $[\frac{J}{kg*K}]$	n_{rn}	n_{cn}
Si	2420	0.279	130	2.5×10^{-6}	170	712	3.882	0.019
SiO_2	2200	0.17	70	0.5×10^{-6}	1.38	1120	N/A	N/A

Table 2.2: Material properties used in analyses. Listed from left to right are the density (ρ), Poisson ratio (ν), Young's modulus (E), coefficient of thermal expansion (α_T), thermal conductivity (k), specific heat capacity (c), real part of the refractive index (n_{rn}), and imaginary part (n_{cn}). We use the convention $\tilde{n} = n_{rn} + in_{cn}$ for the refractive index to avoid ambiguity.

was used for the device thickness, and a gain factor of 0.5 added to the gap-to-substrate. Pre- and post-etch device layer thickness as well as calculated beam thickness and gap to substrate are given in Table 2.1. Since measured device thinning was only slightly larger than the expected accuracy of the thickness measurement, significant error is expected.

Material properties of the Si device layer and SiO_2 oxide layer used in subsequent analyses are presented in Table 2.2. Although Si is an orthotropic material, our devices are oriented along the crystal symmetry planes allowing for an isotropic analysis [50]. The Young's modulus given is E_{100}, the modulus in the direction of bending. FEM analysis using orthotropic material constants with correct device orientation agreed with our isotropic analysis.

2.2.2 Undercutting and Effective Length

Isotropic etchants used in the final release etch away the anchor support in addition to releasing the beam. This undercutting provides a thin webbing around the beam which reduces the beam's stiffness (see Figure 2.4). The relative stiff-

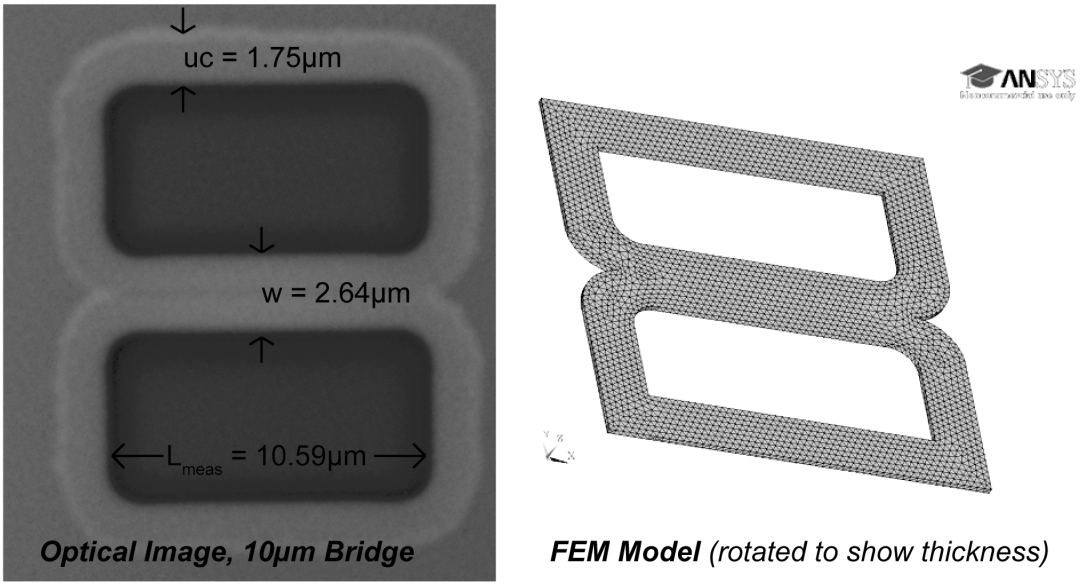

Figure 2.4: Optical image (left) of nominally 10 μm long beam illustrating undercutting, along with finite element model of the beam (right). Rounding at the far corners was not included do to its negligible change to beam stiffness. Ten node tetrahedra are used in meshing (Solid 187).

ness reduction is most pronounced in shorter beams where the undercutting is a significant fraction of the total length and also in doubly-supported beams where undercutting occurs at two supports.

Undercutting, uc, width, w, and length, L_{meas} were measured for a doubly and singly supported device of each length on Chip I[1]. Optical blurring limited measurement precision to $\pm$ 0.35μm. The average undercutting was $uc = 1.75\mu m$, and average width was $w = 2.64\mu m$. We define the effective length, L_{eff}, as the length of a beam with no undercutting which would have the same resonant frequency as the actual undercut beam (ignoring stress effects in doubly-supported beams). In order to calculate L_{eff}, we built a finite element model of the device

[1]Singly-supported 40 μm long devices were not studied since all devices of that length and support were stuck on Chip I.

layer using the measured length and including undercutting (see Figure 2.4). A zero-displacement boundary condition was applied around the perimeter. We used thickness and material properties from Section 2.2.1. The first mode frequency, f_o, was computed using a modal analysis, and compared to theoretical first mode frequencies given as follows [131]:

$$f_o = \frac{k_o^2 t}{2\pi L^2}\sqrt{\frac{E}{12\rho}}, \tag{2.1}$$

where $k_o = 1.875$ for a singly-supported beam (i.e. clamped-free) and $k_o = 4.730$ for a doubly-supported beam (i.e. clamped-clamped). We then solved equation 2.1 for the length, L, that would give a theoretical frequency matching the ANSYS calculated f_o. Results are given in Table 2.3 for singly-supported beams and in Table 2.4 for doubly-supported beams[2]. An ANSYS modal analysis was also performed on models with no undercutting, and calculated frequencies matched theoretical predictions.

Measured resonant frequencies of singly-supported beams matched predicted frequencies well. In doubly-supported beams, pre-stress and imperfection caused measured frequencies to differ from the FEM calculated (unstressed) resonant frequencies used to calculate L_{eff}. This should not affect the validity of our calculation of L_{eff}, which is used to estimate buckling loads and determine buckling parameters in later modeling work. In spite of out best efforts to control the fabrication process, variation exists between devices on the same chip and between chips, thus effective lengths are approximate.

[2]Results given are calculated for Chip I, but used for all other chips released using the same chemistry. Devices on Chip 0 were uniquely thin due to BOE etching, and additionally had more undercutting than Chip I. Effective lengths of doubly-supported devices of lengths 7-25 μm from Chip 0 were analyzed to be 9.11, 12.02, 16.90, 21.84, and 26.84 μm.

Singly-Supported					
L_{nom}	L_{meas} [μm]	f_o [MHz]	L_{eff} [μm]	f_r [MHz], Chip *I*	f_r [MHz], Chip *II*
7 [μm]	7.21	4.50	7.26	4.60	4.42
10 [μm]	10.38	2.19	10.41	2.36	2.23
15 [μm]	15.41	0.998	15.42	0.998	1.01
20 [μm]	20.66	0.556	20.66	0.590	0.582
25 [μm]	25.60	0.362	25.60	0.385	0.371
30 [μm]	30.77	0.251	30.77	0.265	0.260
35 [μm]	35.92	0.184	35.92	0.199	0.193

Table 2.3: Table of device nominal length, L_{nom}, measured length, L_{meas}, FEM calculated unstressed frequency, f_o, effective length, L_{eff}, and measured resonant frequency, f_r, for singly-supported devices. Measured lengths are from Chip *I*, and resonant frequencies are measured at low drive, low laser power. Beams nominally 40 μm were almost all stuck. Finite element modeling includes $uc = 1.75\mu m$ of undercutting.

Doubly-Supported					
L_{nom}	L_{meas} [μm]	f_o [MHz]	L_{eff} [μm]	f_r [MHz], Chip *I*	f_r [MHz], Chip *II*
7 [μm]	7.73	21.97	8.29	20.5	N/A
10 [μm]	10.59	12.30	11.08	12.0	9.85
15 [μm]	15.78	5.76	16.46	5.38	5.30
20 [μm]	21.04	3.29	21.42	3.53	3.65
25 [μm]	26.1	2.16	26.46	2.90	2.89
30 [μm]	31.12	1.53	31.46	2.31	2.36
35 [μm]	36.4	1.12	36.73	1.89	1.97
40 [μm]	41.44	0.901	41.53	1.63	1.70

Table 2.4: Table of device nominal length, L_{nom}, measured length, L_{meas}, FEM calculated unstressed frequency, f_o, effective length, L_{eff}, and measured resonant frequency, f_r, for doubly-supported devices. Measured lengths are from Chip *I*, and resonant frequencies are measured at low drive, low laser power. Finite element modeling includes $uc = 1.75\mu m$ of undercutting.

2.2.3 Stress, Imperfection Level and Initial Deflection

Out-of-plane displacement in released devices could be seen in optical images as color changes across the length of a beam or in tilted scanning electron mi-

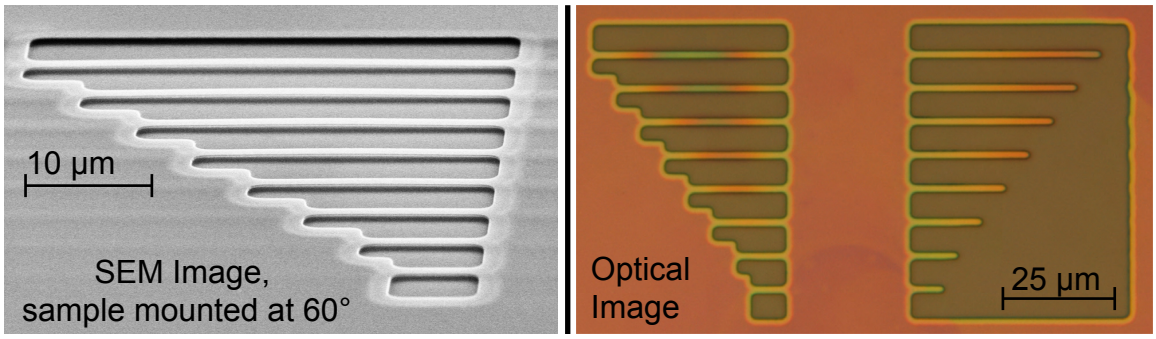

Figure 2.5: SEM image (left) and optical image (right) of devices made using initial mask. The sample is tilted in the SEM image, and *slight* out-of-plane displacement in longer beams is visible. Color variation across beams is visible in the optical image due to interferometric effects.

croscopy (SEM) images as deflection (see Figure 2.5). These out-of-plane displacements were caused by residual stress and stress gradients in our SOI device layer, in addition to possible surface effects in released devices. Measured displacements were small fractions of the beam length but were large in comparison to the period of the interference field ($\frac{\lambda}{2}$ ≈316 nm), dramatically changing the photothermal feedback. In addition, the initial arching of doubly-supported beams and compressive stress across their length shifted their linear resonant frequency, and introduced geometric nonlinearities, leading to an amplitude frequency relationship. Accurate measurement of initial stress level and deformation was thus necessary and is described below.

Wafers ordered from SOITECH came with no available specifications on stress levels, nor were any available from company representatives. Traditionally, compressive stress in thin films is characterized using wafer surface curvature methods [38], or measurement of buckling length of fabricated devices [44]. The first method requires initial curvature measurements before films are grown/evaporated, and was not expected to yield sufficient precision anyway

for the film thicknesses present in our wafers. Thus, the second approach was employed. The theoretical formula for the buckling load, σ_b, of a clamped-clamped beam of length L is [42]:

$$\sigma_b = \frac{\pi^2 E t^2}{3L^2} \tag{2.2}$$

where E is the Young's modulus, t the device thickness, and L the device length. Thus the pre-stress is bracketed by the buckling load of the shortest buckled beam and longest unbuckled beam. Furthermore, since the buckling load depends on beam thickness, our chemically thinned beams give more information about the stress level.

Several techniques were available to determine if an individual beam was buckled. SEM imaging at an oblique angle clearly indicated that longer devices had out of plane deflections, though could not provide a clear threshold length for buckling. Optical inspection gave clearer results about the out-of-plane deflection. In addition to inspection of their initial configuration, devices were driven under vacuum to determine their non-linear behavior. Pre-buckled devices are expected to be amplitude-hardening, and post-buckled beams to be amplitude-softening (see Section 1.3 and Appendix B). Results are given in Table 2.5. Optical inspection and dynamic testing are qualitative in nature and not entirely consistent possibly due to imperfections in the anchor support and residual stress gradients which cause pre-buckling deformation. Optical inspection gave results closer to stress levels suggested by SOITECH, and thus was used to determine buckling.

The actual stress level in the device layer is bracketed by the buckling stress

of the longest unbuckled and shortest buckled beams. Analysis of Chip I gives a range in pre-stress of 37.5 - 63.5 MPa and analysis of Chip 0 gives a range of 45.4 - 89.7 MPa, with the intersection being 45.4 - 63.5 MPa. Thus *if we do not account for imperfection and assume that stress levels are uniform across and chips* then we estimate a compressive pre-stress of σ =55±10 MPa in our devices.

	Chip I, t=200.4 nm		
Length	Nonlinearity Behavior	Optical Inspection	σ_b
7 [μm]	Hardening	Consistent Color	250 MPa
10 [μm]	Hardening	Consistent Color	140 MPa
15 [μm]	Softening	Consistent Color	63.5 MPa
20 [μm]	Softening	Variation in Color	37.5 MPa
25 [μm]	Softening	Variation in Color	24.6 MPa
	Chip 0, t=174 nm		
Length	Nonlinearity Behavior	Optical Inspection	σ_b
7 [μm]	N/A	Consistent Color	156 MPa
10 [μm]	N/A	Consistent Color	89.7 MPa
15 [μm]	N/A	Variation in Color	45.4 MPa
20 [μm]	N/A	Variation in Color	27.2 MPa
25 [μm]	N/A	Variation in Color	18.0 MPa

Table 2.5: Results of optical and dynamic testing of doubly-supported devices from Chips 0 and I, as well as buckling stress calculated using equation 2.2. Dynamic results are not available for Chip 0, since it was re-etched before testing in order to release paddle oscillators not discussed in this dissertation. Devices longer than 25 μm all display softening and variation in color.

More accurate results may be obtained by measuring a beam's initial out-of-plane deflection. Later acquisition of a Zygo 7300 optical profilometer[3] made this measurement possible. Using this data, we could accurately calculate the location within the interference field of different spots on beams, in addition to estimate both *stress and imperfection levels* in doubly-supported beams.

Profiles of singly-supported beams were not consistent between chips, or

[3]Contact profilometers had previously been available, but in general cannot be used to image thin free-standing devices.

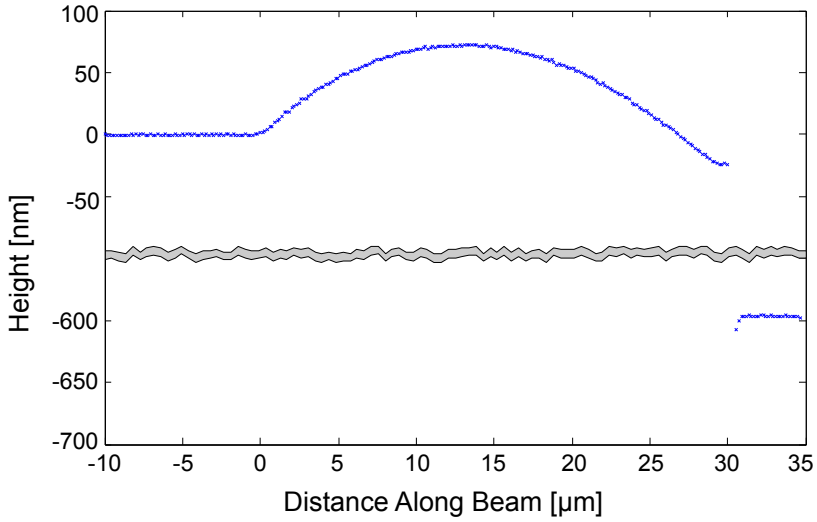

Figure 2.6: Initial deflection of 30μm long singly-supported beam from Chip II. Note the break in the y-axis, and jump in displacement at the right between the topside of the beam at the tip and the substrate below.

even between different beams of the same length on the same chip. They were typically curved up at the anchor point indicating the presence of stress gradients in the device layer [32]. Tip deflections were seen to be as high as ~1 μm. Occasionally, they were also curved back down across the length. Simple beam theory analysis shows that this deflection was not the result of gravity, and is likely due to surface effects. See Figure 2.6 for a representative profile.

Profiles of doubly-supported beams were slightly different between chips, but had little variation within chips[4]. Even the shortest beams showed slight out-of-plane deflection away from the substrate, consistent with the presence of "imperfection buckling." The midline deflection of doubly supported beams from Chips I and II are given in Table 2.6, and a representative profile may be seen in Figure 2.7.

[4]Less than 10 nm variation within a chip is seen in the midline displacement of doubly-supported beams with the same length.

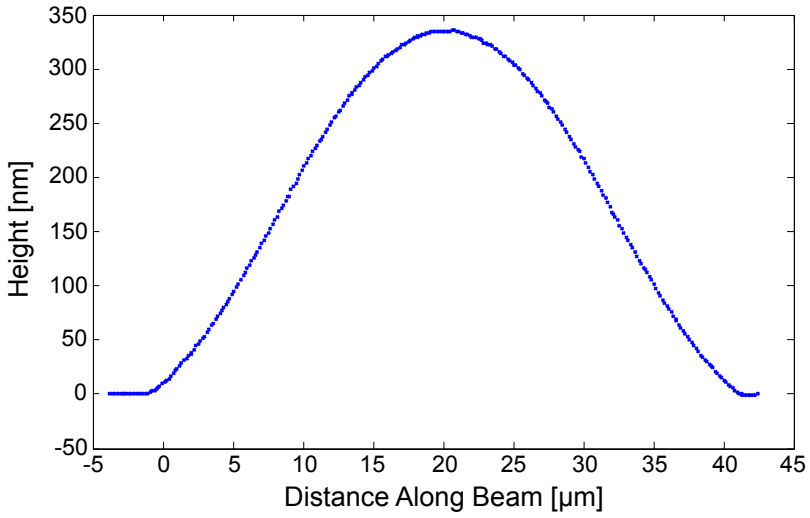

Figure 2.7: Initial deflection of a 40μm long doubly-supported beam from Chip II illustrating buckling.

Using our measured midline deflections, we are able to simultaneously estimate the stress and imperfection level in our devices. Several authors including Luo et al. [75], Nayfeh et al. [85], and Chen et al. [18] have proposed models for determining stress levels in (micro-)beams from their post-buckled configurations. We follow the presentation by Fang et al. [31, 34, 33] who deal explicitly with imperfection levels, and present data in support of their model. Their

Length	Midline Deflection	
	Chip I	Chip II
7 [μm]	37 nm	48 nm
10 [μm]	54 nm	69 nm
15 [μm]	97 nm	120 nm
20 [μm]	158 nm	176 nm
25 [μm]	204 nm	222 nm
30 [μm]	252 nm	263 nm
35 [μm]	286 nm	304 nm
40 [μm]	323 nm	339 nm

Table 2.6: Midline deflection of doubly-supported beams from Chips I and II measured using optical profilometry.

model is briefly described below along with the process used to determine stress and imperfection levels based on measured out-of-plane deflections.

There are many causes of imperfection in microbeams including residual stress gradients in the device layer, fabrication defects, asymmetry of the anchor supports, and initial shape imperfections. Fang et al. lump together all sources of imperfection and model them as an initial shape imperfection in the first buckling [31, 34]. They assume that the amplitude of initial deformation is proportional to the length with non-dimensional constant of proportionality[5], γ_{imp}. Finally, they use non-linear beam theory to derive the following algebraic equation which relates the midline deflection, w_{max}, to the stress, σ, and imperfection level, γ_{imp}:

$$w_{max}^3 + \left(16\frac{I}{A} - 4\frac{L^2\sigma}{\pi^2 E} - \gamma_{imp}^2 L^2\right)w_{max} - 16\frac{I}{A}\gamma_{imp}L = 0 \tag{2.3}$$

where I is the area moment of inertia, A is the cross-sectional area, and E is the Young's modulus. We use the method of least squares to solve for (σ, γ_{imp}) which minimizes the error in predicted midline deflections. For beams from Chip I we get (σ = 16 MPa, γ_{imp} = 0.0051), and for Chip II we get (σ = 11 MPa, γ_{imp} = 0.0066)[6].

[5]Not to be confused with the absorption contrast, γ.

[6]We note that the model is "sloppy" [13], and thus there is a direction in σ-γ_{imp} in which the fitting error does not change significantly in the neighborhood of the best fit. Future work may include measurement of the device frequency to help differentiate displacement due to imperfection and displacement due to compressive stress.

2.3 Experimental Setup

Laser interferometry was used to drive and detect beam motion in a way similar to that described by Carr et al. [17]. Details of similar experimental setups are available in the dissertations of Aubin [8] and Wang [136]. Below we describe the vacuum, optical, and electrical components of our experimental setup. See Figure 2.9 for a diagram of the vacuum system, and Figure 2.8 for a labeled picture. In subsequent sections, we give details on experimental procedures.

The chip containing devices of interest is mounted on a piezo-drive disk (Radio Shack 273-073A Piezo Transducer), leveled, and loaded into the vacuum chamber for testing. The sample holder is bolted to the inside top face of the vacuum cube using vented screws. The bottom face of the vacuum cube consists of a custom viewport through which devices are illuminated, having a 1.4″ diameter 0.13″ thick Corning HPFS 7980 fused silica window with $\sim 87\%$ transmission at $\lambda = 633$ nm (MPF Products). The whole vacuum system is designed using 2.75″ conflat flanges with copper gaskets for ultra high vacuum (UHV) operation. Two BNC electrical feedthroughs are welded into the custom top face for electrical access to the piezo drive.

Vacuum levels are monitored using an MKS 999 multi-sensor transducer thermally isolated from the view cube with a 5.5″ stand-off tube to allow high temperature bake-out of the vacuum cube (200°C), in spite of the limited (85°C) bake-out temperature of the sensor. The vacuum chamber is isolated from the high vacuum pump using a pneumatic gate valve (Kurt Lesker - SG0150PVCF), and from the roughing pump using a pneumatic angle valve (Kurt Lesker - SA0150MVCF). An MKS PDR 900 controller attached the vacuum sensor man-

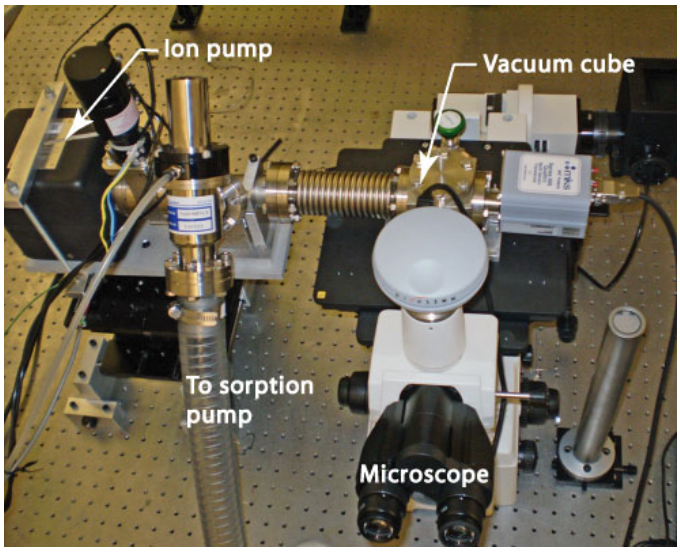

Figure 2.8: Image of experimental setup. Optical and electrical components are not visible.

ages the vacuum valves to ensure pump isolation in the event of a chamber leak. Finally, a Swagelok shut-off valve (Kurt Lesker SS-4H-TW) is mounted on the view cube and used to vent the system before opening it. Rough vacuum ($\sim 10^{-3}$ mbar) is obtained using a cryogenic sorption pump (MDC part # SP-1500), and high vacuum ($\sim 10^{-7}$ mbar) is achieved using a Varian Vaclon Plus 20 Starcell ion pump.

Optical excitation is accomplished with a Spectra Physics SP 106-1 Helium-Neon (HeNe) laser with continuous wave (CW) operation and nominally 20 mW output in TEM_{00} mode. Cross-polarizing optics (Newport 05LP-Vis-B and 05P009AR.14 linear polarizers in MT-RS rotation stages), are used to attenuate the laser power. The beam is aligned to the microscope using two beam steering mirrors and divergence is corrected using a beam expander with adjustable offset second mirror (Newport KPX082 and KPX096 lenses with 50.2 and 113 mm focal lengths respectively). The combination of a polarizing beamsplitter cube (Newport - 05BC16PC.4) aligned with the incoming polarized light and quarter-

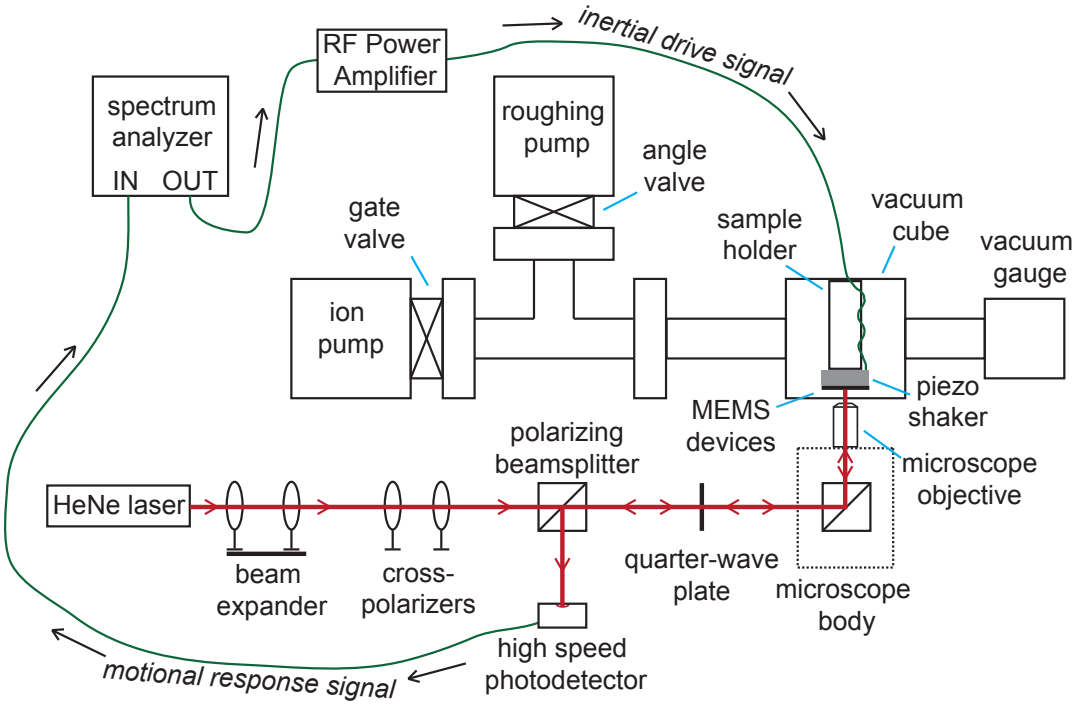

Figure 2.9: Diagram of experiment setup including vacuum, optical and electrical components.

wave plate (Newport - 05RP14-24) between the cube and microscope allows us to separate incoming light from reflected light based on its polarization angle.

Light is focused onto the sample using a Nikon Eclipse TE-2000U inverted microscope with 50× Nikon CFI Plan EPI ELWD objective. Microscope internal optics provide an additional 1.5× magnification for 75× total. Light coming from the laser travels straight through the polarizing beam splitter, through the quarter wave plate, and is focused onto ~ 5 μm diameter spot on the sample by the microscope. Reflected light travels back through the quarter wave plate, is diverted by the beam splitter, and is focused onto a ac-coupled photodiode (Newport 818-BB-21A). The frequency content of the photodiode signal is analyzed on an Agilent E4402-B spectrum analyzer (with option 1DN). The entire

vacuum and optical system is installed on an optical table with Newport XL-A pneumatic isolators for vibration control. Our vacuum system is designed such that it has no moving parts during operation and thus does not introduce vibrations on the optical table.

2.4 Experimental Procedures

2.4.1 Loading Chip and Operating Vacuum

Prior work has shown that micro-device quality factor degrades over time [49], and so devices are loaded and tested as soon as they are released. High purity indium (Alfa Aesar # 14720) is used as a low temperature solder to bond chips to the piezo-drive element. Double-sided tape has been used in similar setups, though it will outgas during vacuum operation. Indium bonds moderately well with the silicon chips and has a melting temperature low enough (157°C) that neither piezo depolarization, nor device annealing are expected to occur during bonding. Slivers of indium are cut using a razor, and placed under the four corners of a chip on top of the piezo disk. The disk is then placed on a hotplate heated to $\sim 160 - 170$°C for bonding.

Once the chip is bonded to the piezo disk, the disk is lightly clamped at its edge in our sample holder. We measure the height at all four corners of the chip using a linear variable differential transformer (LVDT). Unlike calipers or dial indicators, the pressure applied by the light weight of its ferromagnetic core does not bend the piezo disk or de-bond the chip. Using the custom holder's three fine threaded and spring tensioned adjustment screws, the chip height and

tilt are set to positioning the chip within 2 mm of bottom face of the vacuum cube, and leveling to within 0.01°. The vacuum cube top face with attached sample holder, piezo disk, and chip is then bolted back into the vacuum cube.

Rough vacuum is attained using the sorption pump. Once the chamber pressure reaches 5×10^{-3} mbar, the high vacuum ion pump is turned on, and angle valve closed to isolate the chamber from the roughing pump. After chamber pressure stabilizes at $< 10^{-6}$ mbar, the pressure transducer's ion gauge is turned off in order to preclude possible device damage due to ionizing radiation. The pressure is then read from the ion pump's current-pressure relationship.

Alignment of the optical system proceeds in two steps. Initially, the microscope is aligned to the grid of optical table and clamped in place using L-brackets. The laser height is adjusted to be level with the center of the microscope port and in the plane of the optical table. The beam expander is introduced into the optical path before any beam steering mirrors, and the position of the second focusing lens set such that the outgoing beam has no visible divergence. The laser beam is then aligned using the steering mirrors to be centered in and orthogonal to the microscope port. This rough alignment procedure is only performed once, while the following fine alignment procedure is carried out every time devices are loaded. First, the laser power is attenuated using the cross-polarizers and the devices are imaged with a microscope integrated camera (Spot Idea - ID2920). The microscope objective and multiplier intended for data collection are selected. Beam steering mirrors are adjusted such that the imaged diffraction pattern is symmetric, and its center does not change when the microscope is de-focused. Laser spot size is further reduced, by moving the second lens of the beam expander giving the laser beam a slight negative

divergence.

When taking into account measured internal losses in the microscope, measured loss in the viewport, and calculated geometric loss due to the spot size being larger than the beam width, approximately 35% of the power entering the microscope makes it onto the sample. The power entering the microscope is measured using a Thorlabs S120B optical detector and calibrated to polarization angle of the first polarizer. Accounting for microscope losses, we then calibrate the power on sample to the angle of the first polarizer. In this way we can determine the power on sample without blocking the beam path with our optical detector to measure it directly. This allows us to measure hysteresis effects.

2.4.2 Procedures - Transition to Limit Cycle Oscillation

In order to examine the transition to limit cycle oscillation, devices were illuminated at low laser power. The laser spot location was established using the microscope camera, and the image de-focused slightly to maximize the measured resonant peak in the return signal. If thermal noise vibrations were not discernable in the device under test with the intended laser power and spot location, then the device was driven inertially with the piezo disk. The drive amplitude was kept low enough that the resonant response while sweeping up matched the response while sweeping down, i.e. the resonator response was in the linear regime. The laser power was then increased in small increments until the amplitude of response was seen to jump dramatically. A total of 100 sweeps were recorded at each laser power in order to allow for post-collection averaging and statistical analysis. When applicable, oscilloscope traces of the

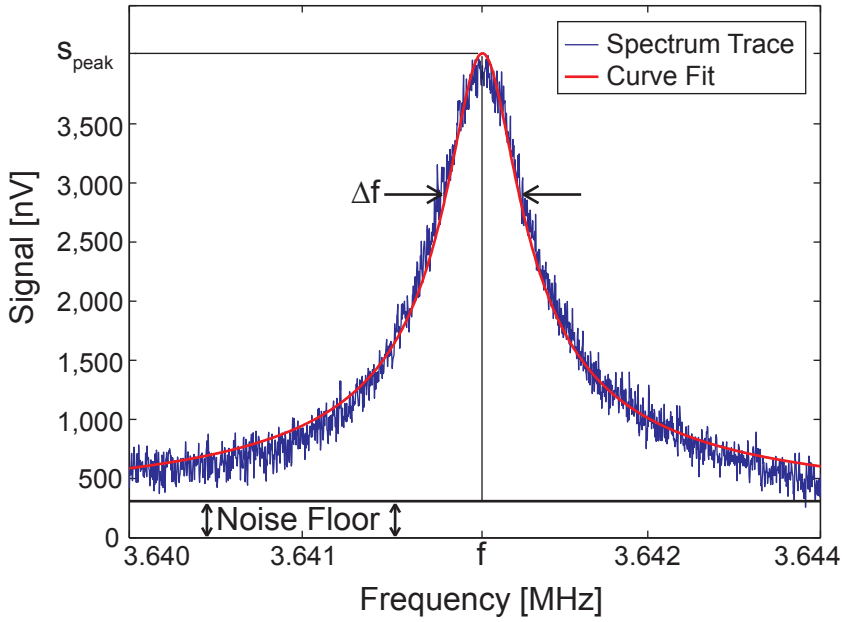

Figure 2.10: Sample resonant curve with curve fitting to Lorentz function to get s_{peak}, f, and $Q \equiv \frac{\Delta f}{f}$. The signal is assumed to be proportional to the amplitude, thus Δf is measured with the signal down by a factor of $\frac{1}{\sqrt{2}}$.

response were also recorded.

For each sweep, the quality factor, Q, resonant frequency, f, and signal amplitude, s_{peak}, were determined by curve fitting the resonant response to a Lorentz function shifted up to account for noise and/or dark current [78]. See Figure 2.10 for an illustration of the curve fitting. The signal amplitude was converted to amplitude of oscillation using the process outlined in Section 2.4.5. Below the laser power threshold for LCO, frequency noise was small in comparison to the resonant width and thus there was little difference between (a) fitting each sweep to obtain Q_i and averaging the results or (b) averaging the sweeps and fitting the average to obtain Q.

The spectrum analyzer's `Resolution BandWidth` (RBW) set a upper limit to the detectable quality factor of

$$Q_{max} = 2\frac{f}{RBW}, \tag{2.4}$$

where f is the resonant frequency[7]. For driven oscillations, the resolution bandwidth of the spectrum analyzer is limited to $RBW \geq 1$ kHz, and for un-driven oscillations, the lowest available RBW is 10 Hz. We define frequency jitter to be the standard deviation of the measured resonant frequency across the 100 sweeps[8].

2.4.3 Procedures - Frequency Tuning

Once the laser power is increased beyond P_{Hopf}, a sharp transition to large amplitude vibrations is seen. In order to check for hysteresis, the laser power is then reduced until the point at which the amplitude of oscillation decreases back to its lower level. Instability in the laser power and limited rotation precision of the linear polarizer limits our control of the laser power to ± 4 μW at 1000μW. As with the case for pre-Hopf thermal noise or driven vibrations, 100 successive sweeps of the resonant response were recorded at each laser power. In addition, 10 successive sweeps of the first 3 harmonics were recorded. Post-Hopf amplitudes of oscillation were typically large enough that the photodiode response signal was visible on an oscilloscope. When applicable, traces of the

[7]Non-linear ringdown is an interesting alternative to measurement of the width of the resonant peak for determining quality factor in non-linear oscillations [20].

[8]This measure is roughly equal to the Allan deviation at a single observation time. We are unable to achieve zero dead time between samples.

response were recorded.

The amplitude of oscillation was once again analyzed using the methods describe in Section 2.4.5. For large amplitude vibration, since the frequency content of the return signal was shifted mostly into the harmonics (see Section 2.4.5), the device resonant frequency was determined by dividing the frequency of the 2^{nd} harmonic by 2. Quality factor was not measured since it has no meaning in the context of self-oscillation.

2.4.4 Procedures - Frequency Entrainment

In order to demonstrate entrainment in our devices, a chip is loaded into the vacuum chamber, and the chamber is pumped down to $\leq 10^{-6}$mbar. A CW unmodulated laser is focused to a spot on the device of interest, and the laser power is increased past the onset of limit cycle oscillations (see Sections 3.1 and 3.2). With the device self-oscillating at limit cycle frequency f_{LCO}, it is then inertially driven at drive frequency, f_D, using the piezo drive[9]. When the limit cycle is entrained, its frequency will be shifted to match the drive frequency, or a multiple/fraction thereof, and the response and drive will be phase-locked. When not entrained, the response will be quasi-periodic with f_{LCO} and f_D frequency components, and the response and drive phases will drift. Frequency matching and phase locking form the conceptual basis for our measurement of entrainment. For more background on the phenomenon of entrainment, see Section 1.4.

In this section, we outline three different experimental procedures for mea-

[9]Note that f_{LCO} is the limit cycle frequency in the absence of any inertial forcing.

suring entrainment in our devices. The methods differ as to the source for generating the drive signal and the tool for determining the frequency content of the response signal. For each method, the data collected is whether or not entrainment is present at each point in time as system parameters are varied.

Filtered Sweep:

The first method employed was to use the spectrum analyzer as the source for the drive signal, and as the tool for examining the frequency content of the response. When set into `Source Mode`, the spectrum analyzer outputs a swept sine wave which we fed through the high frequency amplifier, and applied to the piezo element used to drive the device. The response signal from the photodiode is connected to the input of the spectrum analyzer (Figure 2.11), which filters the input response signal (i.e. device motion) at the output drive frequency. In other words, a narrow band-pass filter is applied to the return signal, whose pass frequency matches the drive frequency.

When the limit cycle is entrained, ($f_{response} = f_{drive}$), the response signal passes through the filter, and a high amplitude signal is measured. When entrainment is lost, ($f_{response} \neq f_{drive}$), the response signal is filtered out, and a low amplitude signal is measured. Thus, when using the spectrum analyzer as the source to study 1:1 entrainment, the measured response is a plateau whose end points show the frequency at which locking begins and is lost (see Figure 2.12). The sweep rate of the drive signal is determined by the `Sweep Time` and `Frequency Span` settings of the spectrum analyzer. By default, the drive frequency is swept up from low to high frequency. Sweep down is achieved by selecting a negative `Center Frequency`.

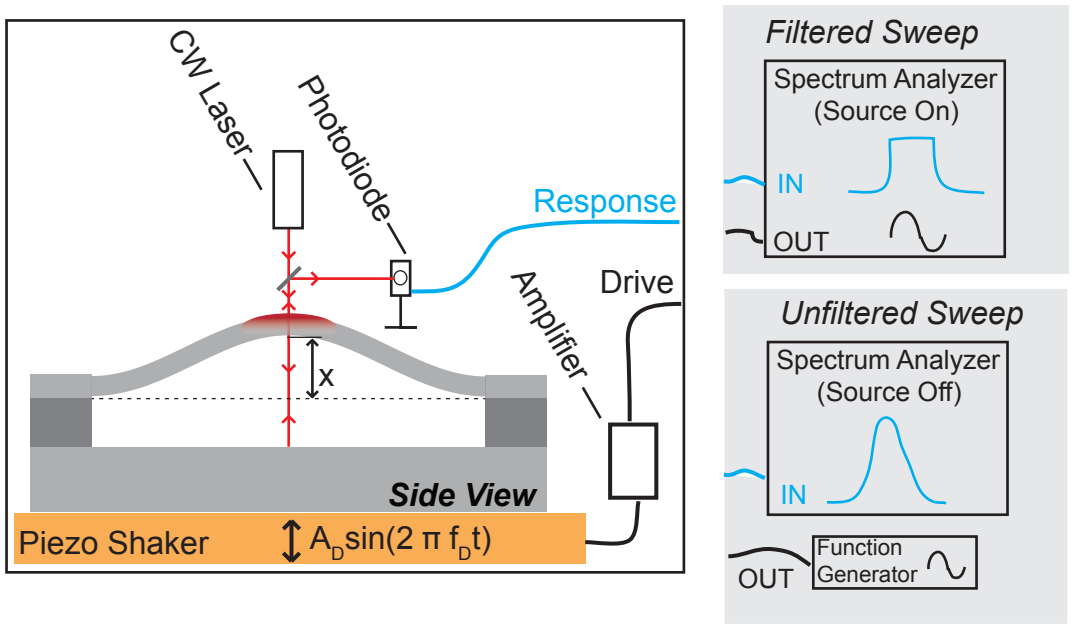

Figure 2.11: Diagram of setup configurations used to measure entrainment.

Since trace data can be saved, and scripts used to help automate the process of picking the endpoints of plateaus, this procedure allows for precise and automated measurement of the frequencies at which entrainment begins and is lost, and is used for measuring statistics of entrainment for weak forcing. The source power is also recorded, converted to peak-to-peak voltage across the piezo with a measured calibration factor, and used as a measure of the drive amplitude, A_D. The spectrum analyzer's minimum `Resolution BandWidth` (pass filter) is $RBW \geq$ 1kHz when in `Source Mode`, limiting the measurable width of the region of entrainment to $\Delta f_{min} \approx 2$ kHz. For very low forcing amplitudes care must be taken in differentiating a narrow plateau indicating a small region of entrainment from a sharp resonant peak which would be present even in the absence of inertial forcing.

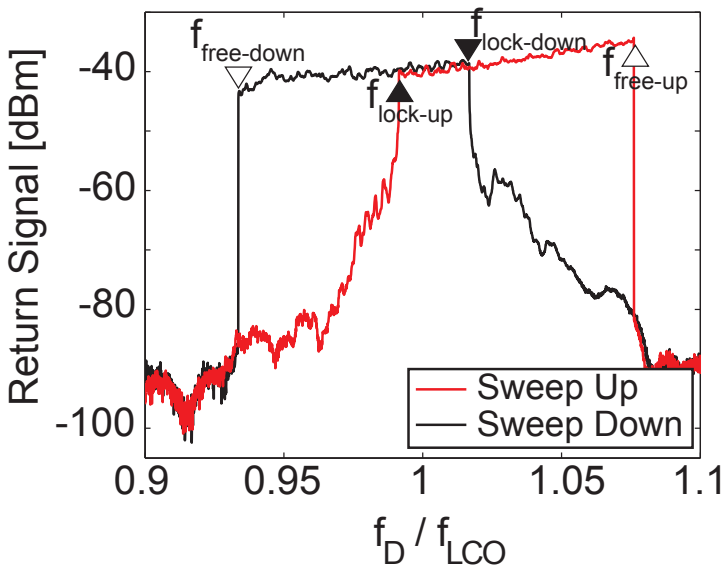

Figure 2.12: Representative results of filtered sweep using spectrum analyzer. In between the filled triangles entrainment is seen in both sweep directions, though to the left and right of this region entrainment depends on the direction of sweep.

Unfiltered Sweep:

Since the band-pass filter used by the spectrum analyzer in `Source Mode` is centered at the drive frequency, we cannot use filtered sweeps to study subharmonic or superharmonic entrainment since the response frequency is at an integer multiple or fraction of the drive frequency. In this case we use a function generator to create the harmonic drive signal, and examine the response signal on the spectrum analyzer or oscilloscope.

A pair of function generators are used to create the swept sine drive signal. We generate a sine wave at the drive frequency using a Hewlett Packard HP3312A 10MHz function generator. This signal is fed through the high frequency amplifier and applied to the piezo element used to drive the device. A

low frequency (~ 1 Hz) triangle wave from a Tektronix CFG250 function generator is input into the HP function generator, placed in `Voltage Controlled Oscillator` mode, and used to slowly sweep the drive frequency. This setup allows us to generate sweep rates as low as $10\frac{Hz}{sec}$ at 200kHz drive, but introduces moderate line noise, such that fluctuations in the drive frequency as high as $\Delta f \approx 500Hz$ at 2 MHz drive are seen.

The response signal from the photodiode (i.e. device motion), is then analyzed in one of two ways. First of all, the spectral content of the response can be observed on the spectrum analyzer. On each ~ 100 ms sweep of the spectrum analyzer, the frequency content of the response is measured. When not entrained, a noisy peak is seen at $f_{LCO} \neq f_D$ and a second steady peak is usually seen at f_D, though it may disappear below the noise floor. The frequency at which entrainment begins and ends is manually recorded from a Tektronix CFC250 100MHz frequency counter connected to the drive signal.

Secondly, entrainment may be verified in terms of phase-locking rather than frequency matching. In limit cycle oscillation, the photodiode signal is large enough to be viewed on the oscilloscope. The drive signal from the function generator and response signal from the photodiode are both input into a Hewlett Packard 54601A 100MHz oscilloscope, and we trigger on the drive signal. When entrained, or phase-locked, the response signal will appear coherent. When not entrained, the response signal will appear as high amplitude noise since its phase will drift with respect to that of the drive.

When n:1 subharmonically entrained, the response signal will complete exactly $\frac{1}{n}$ cycles in the time the drive signal completes 1 cycle. In order words, at a given phase in the drive, the limit cycle is in one of n different phases, and

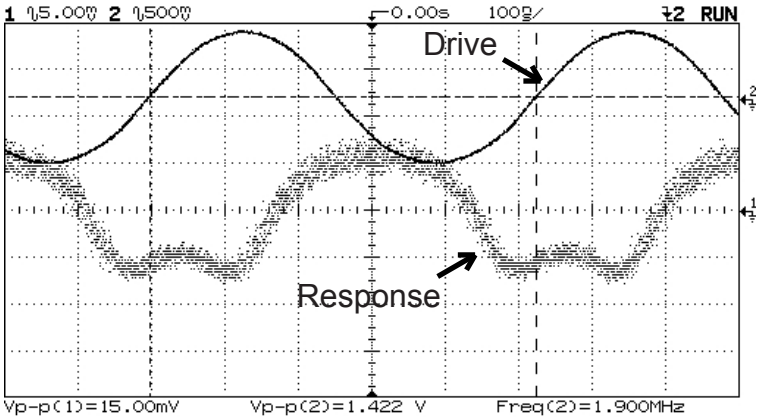

Figure 2.13: Representative data from oscilloscope indicating 1:1 entrainment. Note that in the time the drive signal completes one cycle, the response signal completes exactly one cycle. The small peaks in the through of the response signal are due to non-linearities in our detection scheme (see Section 2.4.5 for details).

the response signal viewed on the oscilloscope will appear as n superimposed signals. Thus in order to view subharmonic entrainment on the oscilloscope, we trigger on the response and look for coherence in the drive signal. This makes the drive signal appear noisy on such plots due to frequency noise *of the limit cycle*.

Finally, we characterized the level of frequency distortion present in the drive signal. Keeping harmonic distortion low is particularly important when measuring superharmonic entrainment - e.g. when driving the oscillator at $f_D \approx \frac{1}{2} f_{LCO}$ with significant $2f$ harmonic distortion, one cannot differentiate between 1:2 entrainment from the signal at f_D and 1:1 entrainment from the $2f$ distortion near f_{LCO}. Due to the frequency dependent electrical and mechanical impedance of our piezo-element, the distortion is frequency dependent. In order to measure the harmonic distortion, the function generator is used to generate a sine wave with amplitude A^{in}_{amp}, which drives the piezo through a high

frequency amplifier. The amplified signal across the piezo with amplitude A_D is viewed on the spectrum analyzer and the power in the first 3 harmonics measured. Sine waves at various frequencies in the range of those used experimentally were tested and distortion levels are reported in Table 2.7.

f_D = 250 kHz				
A^{in}_{amp} [V]	A_D [V]	P[f_2]/P[f_D]	P[f_3]/P[f_D]	P[f_4]/P[f_D]
0.1 V	1.34 V	3.1×10^{-3}	2.5×10^{-3}	2.6×10^{-4}
0.25 V	3.28 V	4.9×10^{-3}	3.3×10^{-3}	2.7×10^{-4}
0.5 V	6.56 V	8.3×10^{-3}	4.9×10^{-3}	3.3×10^{-4}
1.0 V	11.6 V	1.0×10^{-1}	3.9×10^{-2}	4.5×10^{-3}
f_D = 500 kHz				
0.1 V	0.844 V	5.0×10^{-3}	2.4×10^{-3}	2.2×10^{-3}
0.25 V	2.09 V	4.4×10^{-3}	2.6×10^{-3}	1.1×10^{-3}
0.5 V	4.13 V	6.8×10^{-3}	2.2×10^{-3}	3.1×10^{-4}
1.0 V	7.34 V	7.7×10^{-2}	2.1×10^{-2}	2.2×10^{-3}
f_D = 1.0 MHz				
0.1 V	0.400 V	2.2×10^{-3}	1.2×10^{-3}	1.2×10^{-3}
0.25 V	1.00 V	3.9×10^{-3}	2.2×10^{-4}	4.0×10^{-4}
0.5 V	1.94 V	4.4×10^{-3}	1.0×10^{-3}	3.3×10^{-4}
1.0 V	3.40 V	5.2×10^{-2}	8.4×10^{-3}	1.8×10^{-3}
f_D = 2.5 MHz				
0.1 V	0.159 V	1.2×10^{-2}	1.1×10^{-2}	8.7×10^{-3}
0.25 V	0.320 V	1.3×10^{-2}	8.6×10^{-3}	8.0×10^{-3}
0.5 V	0.614 V	2.0×10^{-2}	2.0×10^{-2}	8.2×10^{-3}
1.0 V	1.72 V	2.3×10^{-1}	2.5×10^{-1}	6.5×10^{-2}
f_D = 5.0 MHz				
0.1 V	0.180 V	2.1×10^{-2}	8.2×10^{-2}	1.5×10^{-3}
0.25 V	0.475 V	2.2×10^{-2}	8.7×10^{-2}	8.0×10^{-4}
0.5 V	0.905 V	4.2×10^{-2}	1.0×10^{-1}	5.2×10^{-3}
1.0 V	4.38 V	6.0×10^{-1}	5.4×10^{-1}	1.3×10^{-1}

Table 2.7: Table of harmonic distortion data giving the ratio of the power in each harmonic f_2, f_3, f_4 to the power in at the fundamental drive frequency f_D.

2.4.5 Calibration of Displacement Amplitude

Determining an accurate amplitude of vibration from the reflected laser beam is not a straight forward task due to the non-linearities introduced by the periodic interference field. For high enough amplitude of vibration, the device moves through peaks in the interference field (see Figure 2.14), introducing $2f$ and $3f$ components in the reflected signal and reducing the measured power in the first harmonic, f. For low amplitude of vibration, the reflection vs. deflection curve can be approximated as linear and the modulation in the reflected intensity is proportional to the amplitude of vibration. These distinct ranges of amplitude lead to differing methods of calibration which are presented below along with a brief discussion of the efforts of past researches to calibrate vibration amplitudes in optical detection systems.

High Amplitude Calibration:

Langdon and Dowe first observed that the reflected light from laser interference transduced beams, measured in a photodiode and viewed on an oscilloscope, appeared to be the convolution of sinusoidal device motion with periodic interferometric reflection, resulting in harmonic distortion for large amplitude vibration [67]. Stokes et al. observed the same phenomenon in the frequency domain, seeing strong $2f$ through $6f$ harmonics of the reflected signal when viewed on a spectrum analyzer [118, 117]. Aubin et al. [7] later used this observation as a means to calculate the amplitude of vibration of a disk shaped oscillator by assuming that the device motion was sinusoidal and finding the amplitude of motion which when convolved with the reflection gave the mea-

sured signal[10].

Our approach is similar to that of Aubin et al., though in contrast to the linear cantilevers studied by Langdon, and Stokes, or the small amplitude vibrations (~80 nm) of large disk (21 μm diameter) resonators studied by Aubin, we must deal with stiffness non-linearities which lead to non-sinusoidal motion in our devices.

Letting $s(t)$ be the measured signal, $R(x)$ be the reflectance as a function of displacement, and $x(t)$ be the displacement of the beam as a function of time at the point of illumination, our general problem is to find $x(t)$ given $s(t) = c_o + c_1 R(x(t))$ where the parameters c_o and c_1 are due to the a.c. coupling and sensitivity of the photodiode and are unknown in advance. In order to parameterize the motion[11], we assume that the stiffness non-linearity in our barely post-buckled devices is dominated by the quadratic non-linearity (see Section 1.3). The equation of motion, then becomes:

$$\ddot{x} + x + \epsilon x^2 = 0; \tag{2.5}$$

where we introduce a parameter, ϵ, to account for the strength of the non-linearity. Solutions to 2.5 are given as an exercise in [101], and are of form[12]:

$$x(t) = a_o + a_1 sn^2(u, k);\ u(t) = a_2 t + a_3 \tag{2.6}$$

[10]Zook et al. [56] also give a good qualitative description of harmonic distortion in such optical systems.

[11]In general one could use splines, though this would result in an increasingly large number of fitting parameters, and minimization of residuals would likely be plagued by spurious local minima.

[12]A verification of this solution for the case of $\epsilon = 1$ is given in Appendix 4 of [100], and the proof for $\epsilon \neq 1$ follows the same procedure.

where $sn(u,k)$ is the Jacobi elliptic function with argument u and modulus k [1], and the median shift, a_o, amplitude, a_1, "frequency", a_2, and phase, a_3, are parameters. Note that the period with respect to u of $sn(u(t),k)$ depends on the modulus, k, and thus the period of $x(t)$ with respect to time depends on k and a_2. Measured frequency is input as a constraint between a_2 and k to effectively eliminate one parameter. In addition, we neglect the median shift, a_o, which is small relative to the amplitude, a_1. Given a measured oscilloscope trace of $[t_i, s_i]$, $i = 1..n$, the problem thus becomes one of choosing the parameters $\bar{p} = [c_o, c_1, a_1, k, a_3]$ that minimizes $\Sigma_i[s_i - s(R(x(\bar{p}; t_i)))]^2$. See Figure 2.14 for an illustration of this fitting. Spectrum analyzer measurements of the frequency content in the measured signal are shown in Figure 2.15. Calibration of displacement amplitude based on relative magnitude of harmonics was initially tried, though oscilloscope traces are a richer data set which gave better results.

Low Amplitude Calibration:

When the amplitude of vibration is less than the distance to the nearest peak/valley in the interference field, the interference field may be approximated as linear. In addition, stiffness non-linearities which produce anharmonicity in the motion may be ignored for small vibrations. In this regime, shape fitting the measured reflection gives poor results, since the shape of the motion is very close to harmonic and there is little harmonic distortion in this entire range. However, since the photodiode current is proportional to the laser intensity, in this regime the height of the measured resonant peak (see Figure 2.10), scaled by the laser power, may be assumed to be proportional to the amplitude of vibration, i.e.:

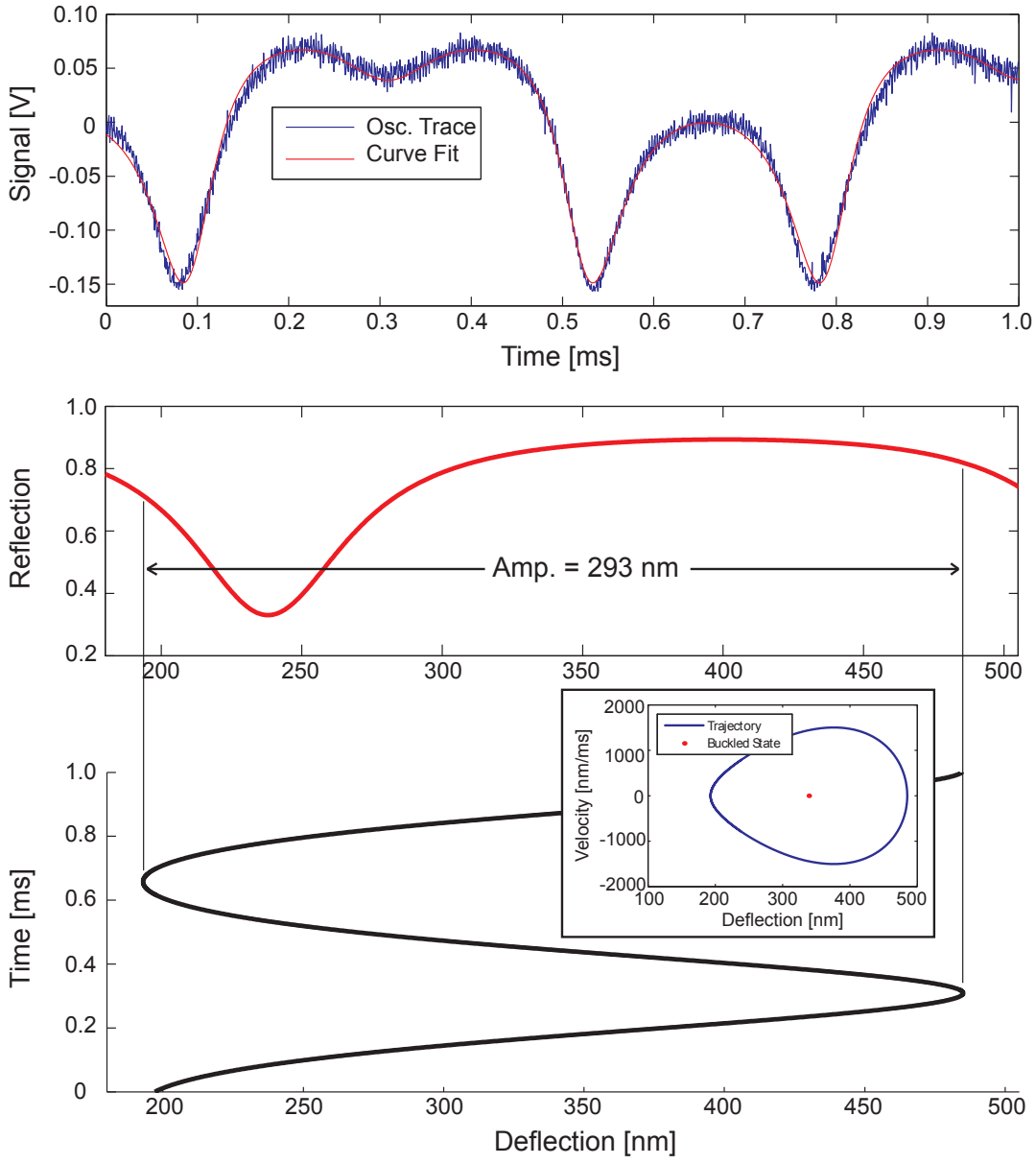

Figure 2.14: (top) Oscilloscope trace data along with curve fitting; (middle) Plot of reflectance as a function of displacement, $R(x)$; (bottom) Displacement as a function of time, $x(t)$, from fitting. Inset is the fit trajectory illustrating the anharmonicity of the motion. Data is from limit cycle oscillation in a 40 μm beam from Chip II, illuminated with 1.05 mW on sample.

$$A = \frac{s_{peak}}{P \times SF} \tag{2.7}$$

where A is the amplitude of vibration in nm, SF is the scale factor in $\frac{nV}{nm\,\mu W}$, s_{peak} is the height of the resonant peak in nV, and P is the laser power on sample in μW. In order to determine the appropriate scale factor, SF, it is sufficient to measure vibration with a single known amplitude in this regime. Below we compare three different methods for obtaining oscillation of a known amplitude. In our experiments we use the final method. The first tow are presented and discussed for comparison purposes.

Method I: Thermal Tune

One such method which gained interest due to applications in atomic force microscopy and gravity wave detection, is to measure the amplitude of thermal noise vibrations. Calculations based on the Equipartition Theorem relate the thermal noise amplitude to resonator stiffness and mass. A good treatment by Butt is available [15], as well as others [110, 52, 40]. An example of its use in calibration is given in Ref. [133]. The most simple treatment by Hutter et al. relates the thermal noise amplitude to the beam stiffness using:

$$\sqrt{\hat{z}^2} = \frac{0.64}{\sqrt{K}}, \tag{2.8}$$

where $\sqrt{\hat{z}^2}$ is the thermal noise amplitude in Å at room temperature and K is the beam stiffness in $\frac{N}{m}$. We can calculate the stiffness using beam theory as:

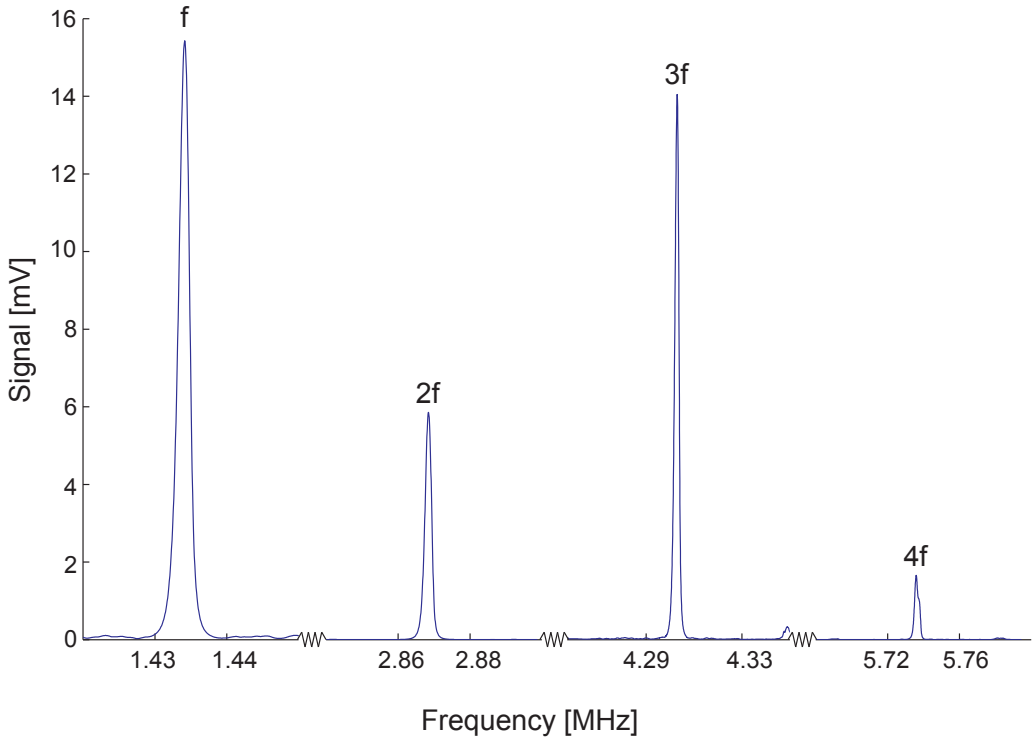

Figure 2.15: Spectrum analyzer data from set matching trace data in Figure 2.14. Note the significant harmonic distortion due to both the anharmonicity of the motion and the nonlinearity of the reflection as a function of displacement.

$$\begin{aligned} K &= \frac{192EI}{L^3}, \qquad \text{doubly-supported;} \\ K &= \frac{3EI}{L^3}, \qquad \text{singly-supported.} \end{aligned} \tag{2.9}$$

Use of this technique in optically self-excited systems is problematic since parametric amplification is seen to increase or decrease the amplitude of thermal noise vibrations. As a result, there is a trade-off between the high laser pow-

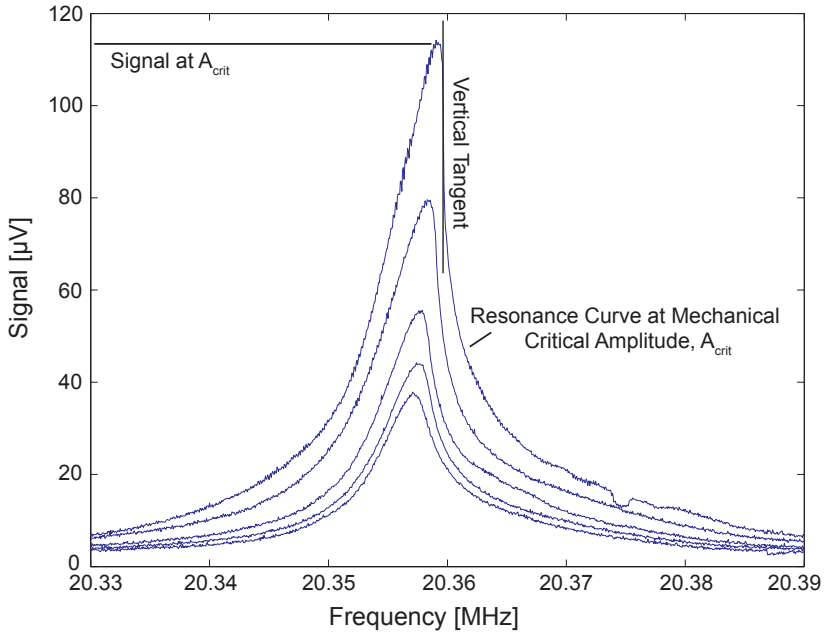

Figure 2.16: Mechanical critical amplitude in driven oscillation of a 7 μm doubly-supported beam from Chip I with 370 μW on sample.

ers needed to resolve such vibrations and the increase in vibration amplitudes that happens as a result of parametric amplification at higher laser powers.

Method II: Mechanical Critical Amplitude

A second method used by Carr et al. relies on measurement of the mechanical critical amplitude, A_{crit}, defined as the amplitude of vibration for which the resonance curve develops a vertical tangent as a result of stiffness nonlinearities [16]. Tilmans et al. derive an equation relating the critical amplitude of a doubly-supported beam to its geometric properties and quality factor assuming no pre-stress[128]:

$$A_{crit} \approx \frac{2t}{\sqrt{0.528Q(1-\nu)^2}} \tag{2.10}$$

where t is the beam thickness, Q the quality factor, and ν the Poisson's ratio. Note that this amplitude is independent of device length. Several treatments are available. Kaajakari et al. give a formula for the critical amplitude in terms of the effective non-linearity and quality factor, and then present a derivation of the effective non-linearity in a doubly-supported, unstressed beam [59]. An alternate formula is also given by Postma et al. [97]. However, measured data are not presented in the above papers to validate the models presented. In our calibration we follow Tilmans' formulation. The 7 μm beams are selected since they are closest to being un-stressed, and they are driven at various forcing levels to measure the mechanical critical amplitude. See Figure 2.16 for experimental data[13].

Use of this technique is problematic in several ways. First of all, such calculations for unstressed doubly-supported beams, are not applicable to our singly-supported beams which do not support midplane stretching, or post-buckled doubly-supported beams whose non-linearity is geometric. Secondly, differing out-of-plane displacements between different beams or at differing points on the beam changes the optical contrast leading to more or less modulation of the reflected signal for the same amplitude of vibration. As a result, scale factors are specific to a device and illumination spot on the device.

Method III: Optical Critical Amplitude

[13]Some authors define A_{crit} as the maximum amplitude on the resonance curve with a vertical tangent, and others define it as the amplitude on that curve at the point of vertical tangency. In Figure 2.16 we illustrate the former definition.

In calibrating our scale factor for low amplitude vibration, we rely on measurement of the optical critical amplitude, defined as the lowest amplitude of vibration for which the device moves through a peak/valley in the interference field (see Figure 2.17). As a result, this method ensures continuity with high amplitude calibration. A list of scale factors is given in Table 2.8 and compared with results from the other two methods. A sensitivity analysis was performed on our calculations for the 30 μm and 40 μm doubly supported beams, assuming errors in the measured film thickness of ±2 nm. This level of error in film thickness gave deviations in the scale factors of 5.5% and 0.8% for the 30 and 40 μm beams respectively. High amplitude data was re-calculated and gave deviations of 4.2% and 8.3% respectively. Some recent notable work on calibrated optical detection has been done using pulsed lasers [74, 73].

Device	SF Method III	SF Method I	SF Method II
30 μm doubly-supported	360	913	54.0
35 μm doubly-supported	151	288	54.0
40 μm doubly-supported	137	147	54.0
35 μm singly-supported	1090	556	54.0

Table 2.8: Scale factors, SF in $\left[\frac{nV_{signal}}{nm_{amplitude}\,\mu W_{laser}}\right]$, for devices from Chip II calculated using various methods. Doubly-supported beams are illuminated at their midline, and singly-supported beams at their tip.

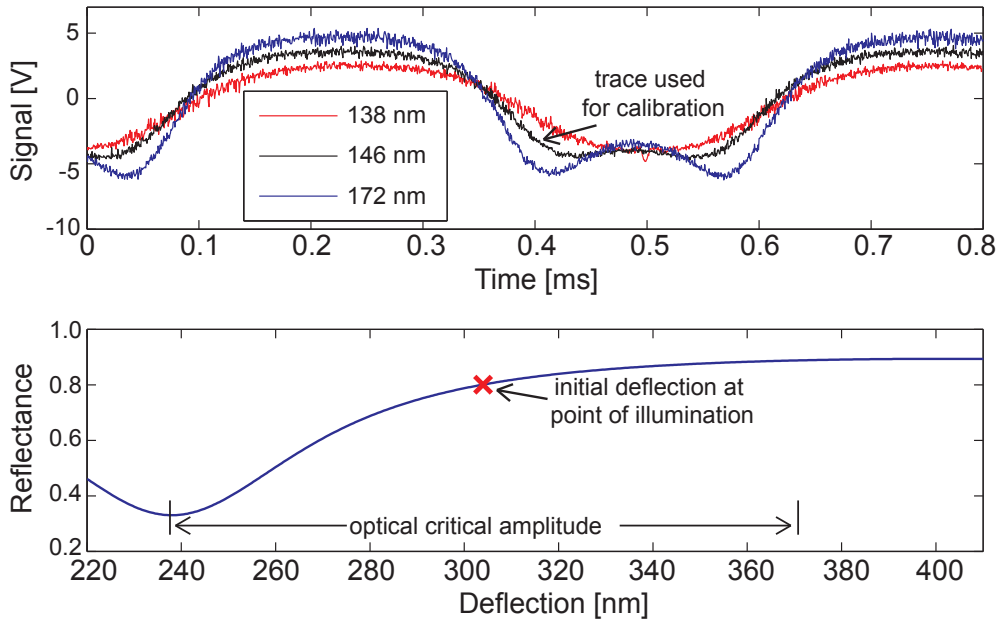

Figure 2.17: Oscilloscope traces for 35 μm double supported beam (top), with amplitude of oscillation below the optical critical amplitude, at it, and above it. For oscillation amplitudes higher than the optical critical amplitude, secondary peaks are visible in the reflected signal. In addition, the optical critical amplitude is illustrated on the reflectance curve (below).

CHAPTER 3

EXPERIMENTAL RESULTS AND DISCUSSION

3.1 Transition to Limit Cycle Oscillation

In this section, we present results on the transition to limit cycle oscillation (LCO) in singly- and doubly-supported devices. Behavior of the device is seen to depend in a complicated fashion on the location on the beam which is illuminated, and on laser power. Given a device and location illuminated on the device, increasing the CW laser power was seen to do one of two things: inhibit oscillation leading to a decrease in quality factor; or reinforce oscillation leading to an increase in quality factor. In the later case, as the power was increased past $P = P_{Hopf}$ large amplitude LCO began. These different behaviors are illustrated in Figure 3.1, with feedback damping in a 25 μm doubly-supported beam, and the transition to LCO in a 40 μm doubly-supported beam, both illuminated at their midline.

The transition to LCO was also measured with respect to the amplitude of oscillation. When feedback was of the correct sign to reinforce oscillation, low amplitude thermal noise vibrations ($O(0.1)$ nm) gave way to high amplitude limit cycle oscillations ($O(1-100)$ nm) as the laser power was increased beyond $P = P_{Hopf}$. See Figure 3.2 for a plot of the peak-to-peak amplitude of vibration as a function of CW laser power for several devices from Chip II illuminated at their center. Note that shorter doubly-supported devices were seen to exhibit slower growth in amplitude after the Hopf bifurcation and a lower limiting amplitude than longer doubly-supported beams. Variation in limiting amplitude as a function of location within the interference field was previously observed

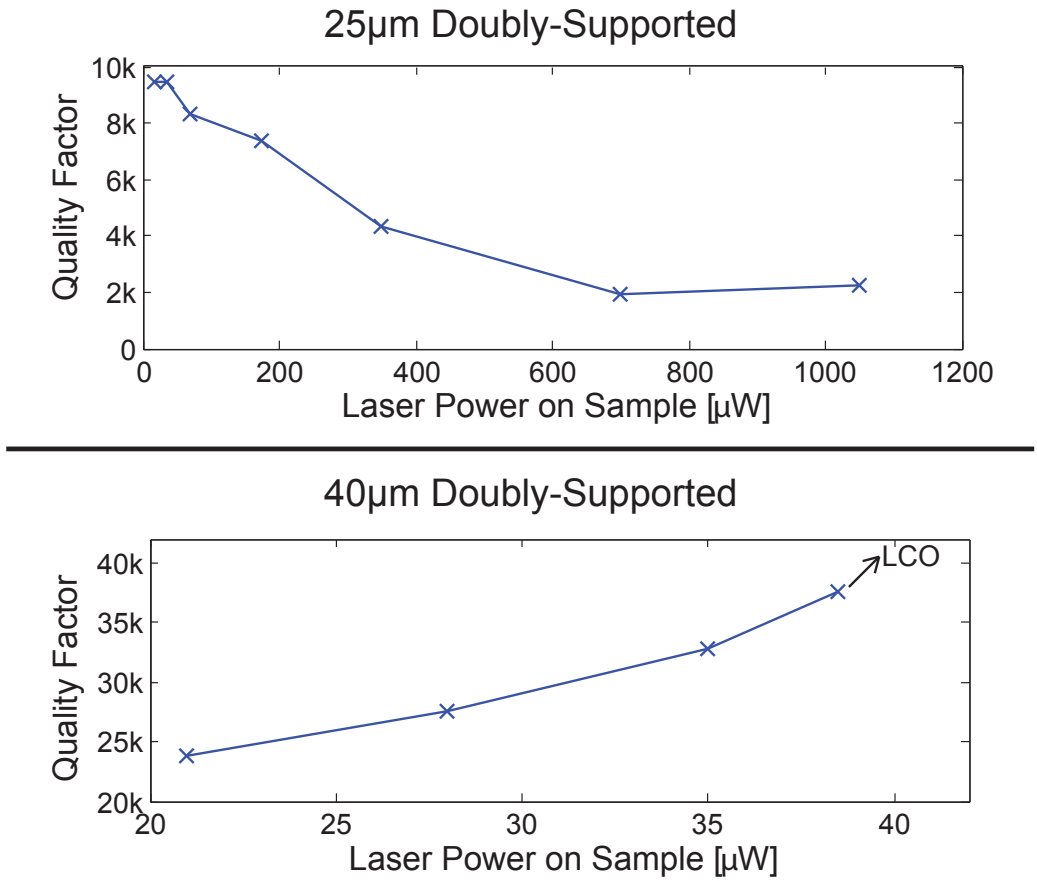

Figure 3.1: Quality factor as a function of laser power on sample for two doubly-supported devices from Chip II subject to centerline illumination. For P>37μW in the 40 μm beam the resonant peak is narrower than the resolution bandwidth and the precise quality factor cannot be measured. For P $\geq$ 50 μW, limit cycle oscillation is seen.

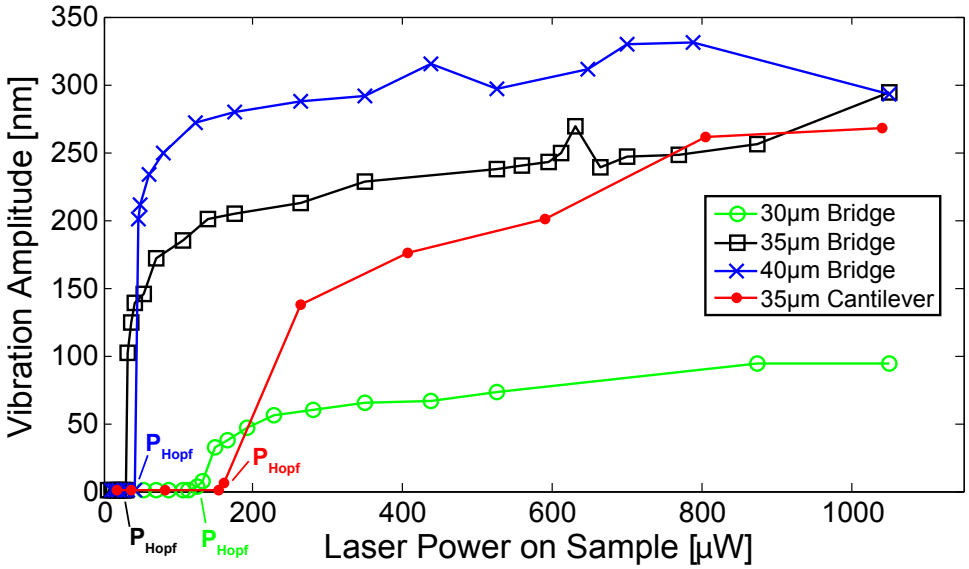

Figure 3.2: Peak-to-peak amplitude of vibration as a function of laser power on sample in devices from Chip II. Doubly-supported devices are subject to centerline illumination. The singly-supported device is subject to illumination near the midline, slightly closer to tip than anchor.

by Hane et al., though they were unable to measure the actual gap to substrate in order to determine the location of the beam within the interference field [46].

Due to imperfection buckling in our devices, each length of doubly-supported devices has a different centerline displacement and corresponding location within the interference field. In Figure 3.3 we plot the location of the beam centerline within the interference field for doubly-supported devices from Chip II using the measured buckling amplitude from Table 2.6. Laser heating will cause additional static deflection. FEM analysis shows that this deflection is $O(1)$ nm for the doubly-supported devices studied and laser powers used [10], and thus can typically be neglected.

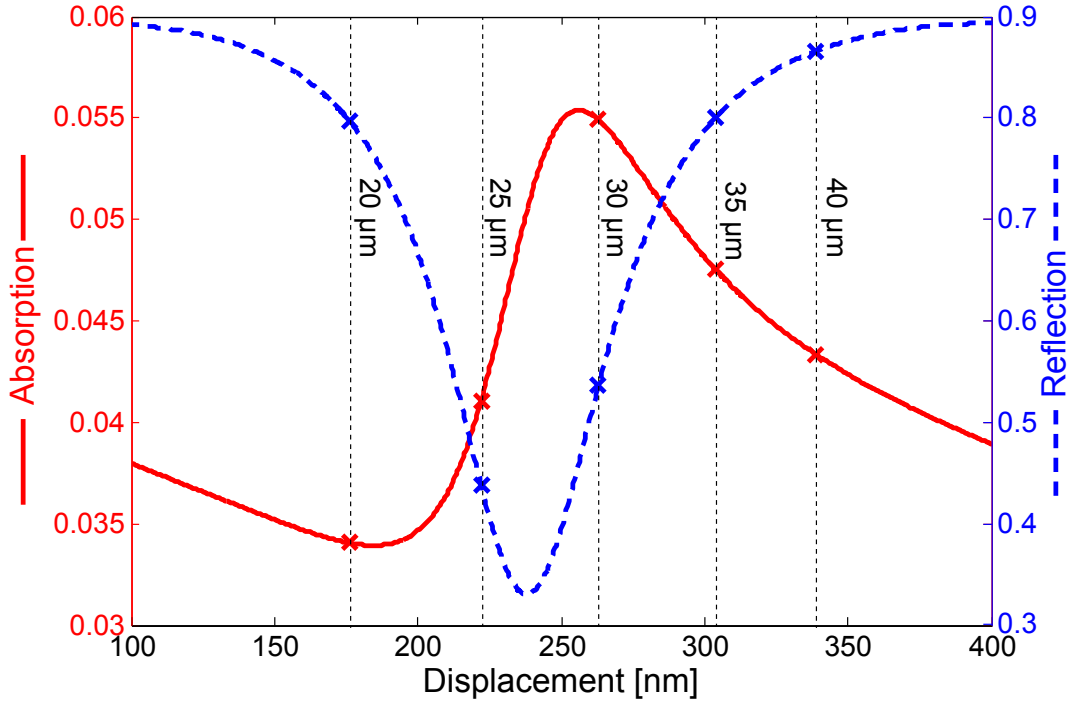

Figure 3.3: Location within the interference field of the midline of doubly-supported beams from Chip II . Out-of-plane deflections due to both imperfection and compressive pre-stress in devices are discussed in Section 2.2.3.

Comparing Figures 3.2 and 3.3 we note that the limiting amplitude is more complex than the distance from equilibrium to some point in the interference field. Were that the case, the difference in limiting amplitude between different data sets would be equal to twice the difference in their equilibrium positions. However, this is not the case in the data. Note that the difference in the limiting amplitude of vibration between the 30 and 35 μm beams and the 35 and 40 μm beams from Figure 3.2 is ~170nm and ~ 65nm respectively. On the other hand, the difference in centerline displacement from Table 2.6 is 41 and 35 nm respectively. While the relationship between limiting amplitude and location within the interference field is close for the 35 and 40 μm beams, it is not at all

for the 30 and 35 μm beams. This observation is consistent with the data from Ref [46].

The sensitivity of limiting amplitude to changes in the location within the interference field was most pronounced in the 30 μm beams which were closest to a peak in the absorption. The measured difference in device thickness of 2.8 nm between Chips I and II (see Table 2.1) altered the interference field slightly, and led to a measured 11 nm difference in centerline deflection (see Table 2.6). Amplitude of vibration as a function of laser power in these devices is plotted in Figure 3.4 alongside the location of the beam centerline within the interference field.

The threshold power for self oscillation was also seen to depend on the specific location on the beam which was illuminated. This result is likely due to a combination of two factors: first of all, as we scan the illumination spot along the beam the location within the interference field of the beam at the spot changes due to out-of-plane displacements; and secondly that illumination closer to the anchor produces a smaller increase in temperature for the same laser power leading to a weaker thermo-mechanical coupling. Measured values for P_{Hopf} at various points of illumination on a 40 μm doubly-supported beam from Chip II are depicted in Figure 3.5, along with the measured out-of-plane displacement and corresponding location within the interference field. Values of P_{Hopf} vary by a factor of 50 as we scan along the beam, with the minimum power being at a location offset from center and the maximum power being at a location close to the anchor. Note that illumination at points **e** and **f** produces self-oscillation despite positive absorption contrast, and the additional out-of-plane deflection needed to achieve negative absorption contrast is much larger than the shift

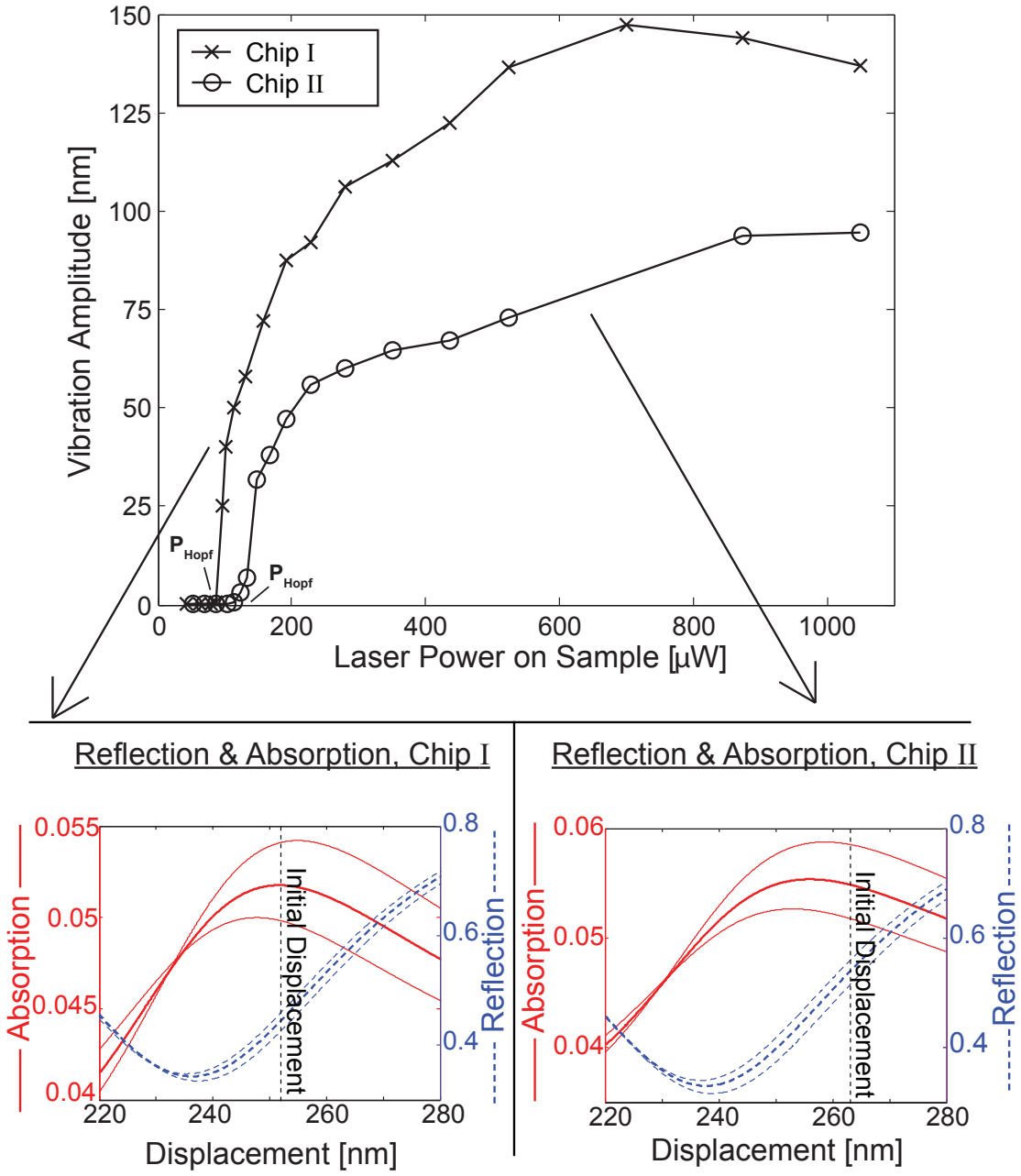

Figure 3.4: Comparison of vibration amplitude of 30 μm doubly-supported devices on Chips I and II, subject to centerline illumination (top). Reflection and absorption based on measured thicknesses from Table 2.1 are plotted at the bottom using thick lines. Thin lines indicate solutions given a variation of ±2 nm in the measured device thickness. Error in the measured buckling amplitude is not considered, but would lead to a shift along the x-axis of the vertical dotted line.

expected due to absorptive heating[1].

Complementary results for a 35 μm singly-supported beam are given in Figure 3.6. The specific device tested later became stuck during entrainment testing and thus optical profilometry data is not available. Due to the variability in static deflection among singly-supported devices of the same length, displacement data from a different 35 μm beam is not given. Note the sharp transition between low power self oscillation at point **c** and negative feedback leading to vibration damping at point **d**. In limit cycle oscillation, thermal waves due to periodic surface heating will traveling down the beam and be sunk into the underlying oxide layer at the anchor point causing deflection in the singly-supported beam (see Section 4.1). The phase lag of this thermal wave and corresponding stress at the anchor will depend on the distance to the anchor. As a result, we might expect that P_{Hopf} is a periodic function of location of illumination whose period matches that of the thermal wave in the beam. For this device, the characteristic thermal length of δ =12.6 μm (see Section 4.5)is much longer than the length associated with changes in P_{Hopf} suggesting that the variation in P_{Hopf} is due to out-of-plane displacement and not the phase of thermal waves.

It was observed by Sekaric et al. [112], that in optically transduced devices exhibiting limit cycle oscillation, an increase in the laser power of illumination leads to an increase in quality factor for $P < P_{Hopf}$. As a result, the slope of the Q vs. P curve is an indicator of the possibility of limit cycle oscillation. This fact was born out by our data. Thus, for illumination of devices where quality factor increased with laser power, though LCO was not observed at the maximum

[1]Note that the laser spot is of finite extent, leading to a range of out-of-plane displacements and at the location of illumination particularly away from the beam anchor and midline where the beam angle is the highest. The 5 μm diameter spot leads to a variation in out-of-plane displacement of ± 50 nm at points **e** and **f**.

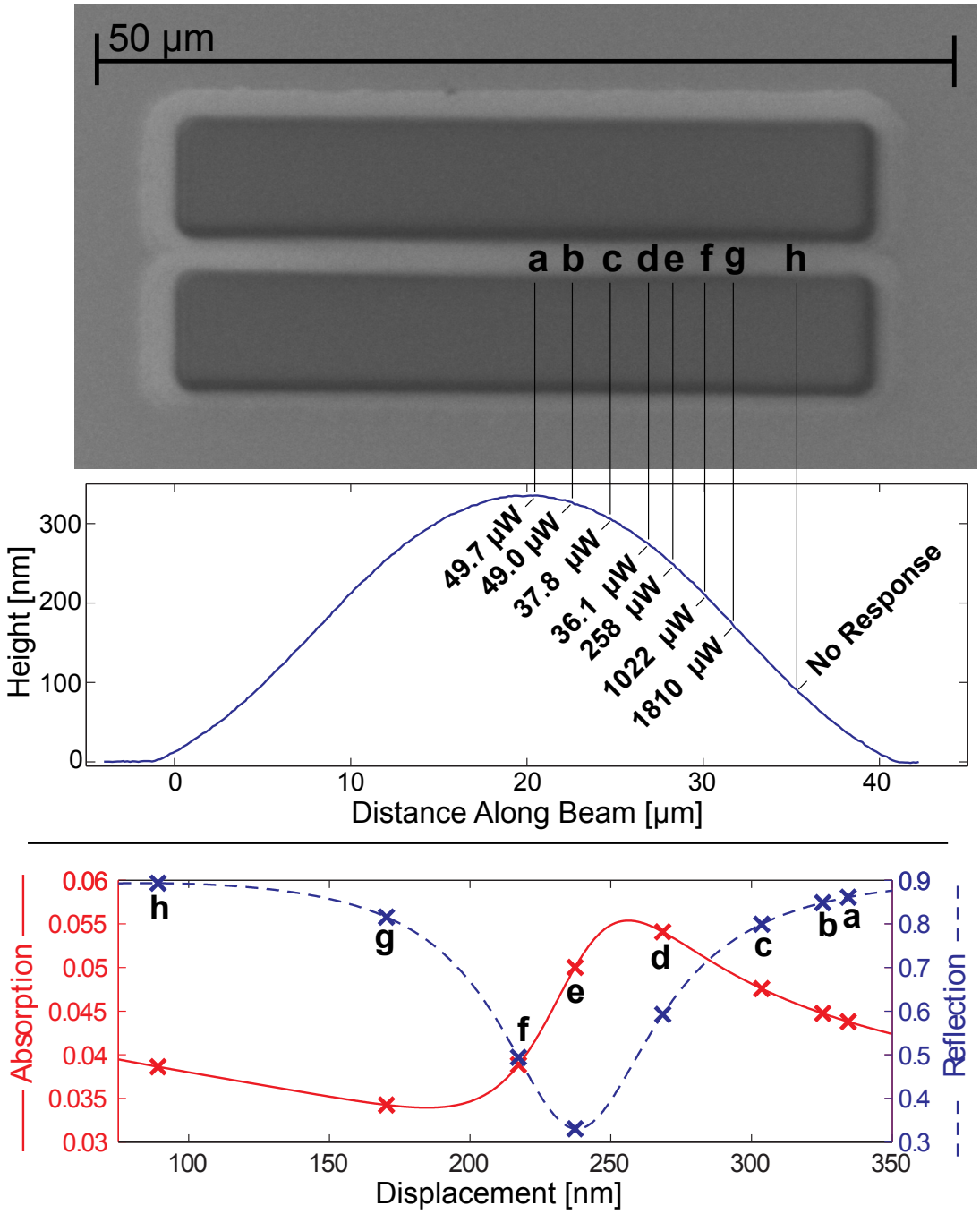

Figure 3.5: P_{Hopf} as a function of spot location in a 40 μm doubly-supported device from Chip II (top). Included is a plot of the beam displacement based on optical profilometry data (middle) and the corresponding location in the calculated interference field for each point of illumination (bottom).

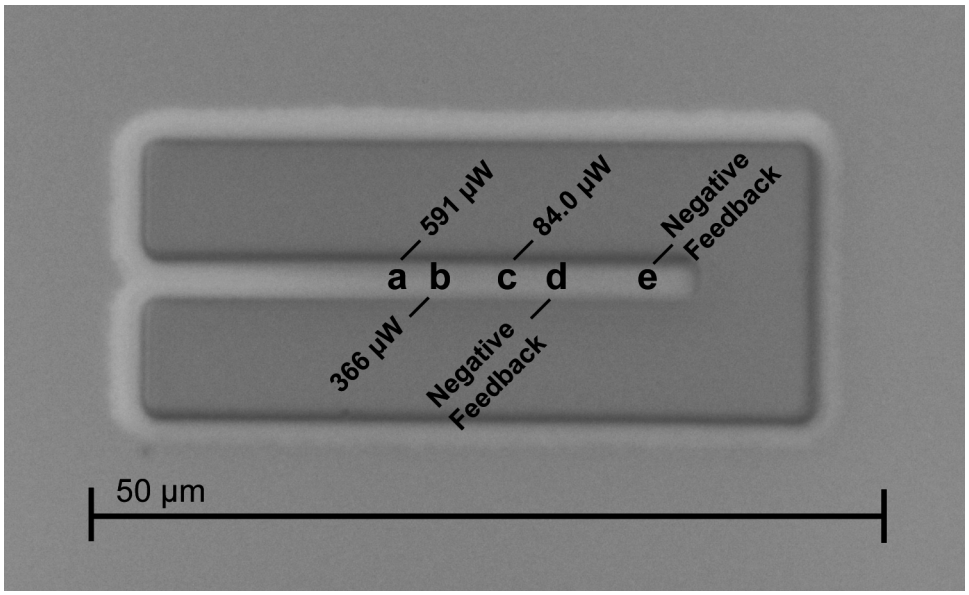

Figure 3.6: P_{Hopf} as a function of spot location on 35 μm singly-supported device.

possible power on sample, we predict that LCO would occur at higher laser powers.

Device, Chip II	P_{Hopf} [μW]	P_{SNBC} [μW]	Notes
20 [μm]	N/A	N/A	Q decreases as P increases
25 [μm]	N/A	N/A	Q decreases as P increases
30 [μm]	128	117	
35 [μm]	32	32	No hysteresis observed
40 [μm]	50	39	
Device, Chip I	P_{Hopf} [μW]	P_{SNBC} [μW]	
30 [μm]	93	91	

Table 3.1: Laser power on sample at onset of LCO (P_{Hopf}) and destruction of LCO (P_{SNBC}) in doubly-supported beams illuminated at their midline.

In most cases, the Hopf bifurcation is sub-critical and hysteresis is seen whereby the LCO persists as the laser power is reduced from P_{Hopf} to a lower power P_{SNBC} at which point the limit cycle is lost in a saddle node bifurcation of cycles [7]. The width of such hysteresis loops was observed to be small in com-

Device, Chip II	P_{Hopf} [μW]	P_{SNBC} [μW]	Notes
20 [μm]	> 2,100	> 2,100	Q increases as P increases
25 [μm]	56	48	
30 [μm]	341	341	
35 [μm]	N/A	N/A	Q decreases as P increases
40 [μm]	N/A	N/A	All devices stuck

Table 3.2: Laser power on sample at onset of LCO (P_{Hopf}) and destruction of LCO (P_{SNBC}) in singly-supported beams illuminated at their tip.

parison with P_{Hopf}. The values of P_{Hopf} and P_{SNBC} are summarized for doubly-supported beams subject to centerline illumination in Table 3.1 and for singly-supported beams subject to illumination at their free end in Table 3.2.

It is difficult to confirm or invalidate past theoretical work based on our measured values of P_{Hopf}. Due to their large out-of-plane displacements in comparison to laser wavelength as well as destructive testing for entrainment, accurate determination of the location within the laser interference field of spots on singly-supported beams is infeasible. This determination is possible in doubly-supported beams, though strong conclusions cannot be drawn from the data. Based on centerline illumination, negative absorption contrast seems to lead to LCO, though this conclusion is not borne out by testing with laser focus at differing locations along a beam.

3.2 Frequency Tuning

In this section, we present results on the frequency of LCO oscillators. Membrane stresses in doubly-supported beams are a source of non-linearity which allow for tuning of the linear frequency and give rise to an amplitude-frequency

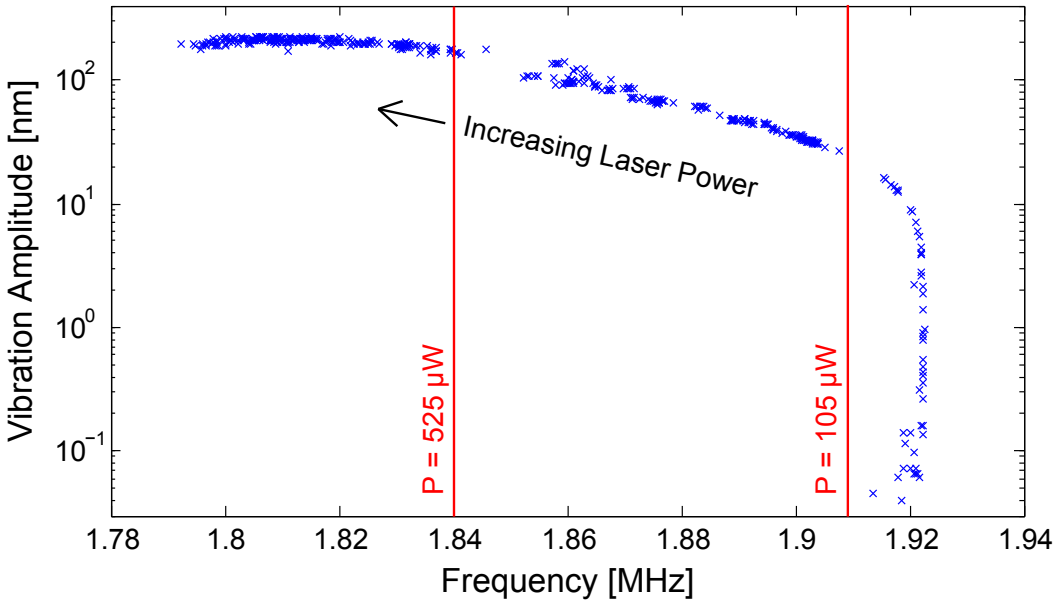

Figure 3.7: Amplitude-frequency relationship in a 35 μm beam from Chip I, subject to centerline illumination. The cross polarizing filter was slowly adjusting during data collection to vary the laser power attenuation. Each "x" represents the amplitude and frequency measured during a single sweep of the spectrum analyzer (see Figure 2.10). Since oscilloscope traces are not available for each data point, vibration amplitude was determined using the low-amplitude scale-factor and is approximate.

relationship (see Figure 3.7). We find that linear and non-linear tuning mechanisms compete in these devices. Singly-supported devices are seen to exhibit frequencies which are stable over a large range of amplitudes and laser powers.

To begin with, doubly-supported beams are illuminated at their midline at various laser powers below P_{Hopf}, and driven with the piezo at low amplitude to measure their linear resonant frequency - results are shown in Figure 3.8. In the region of interest, the relationship between linear frequency and power on sample is highly linear, with least squares fit slopes given in Table 3.3.

Note in Figure 3.8 that the linear resonant frequency decreases with laser power in the 7 and 10 μm beams which are amplitude hardening, and increases with laser power in the 15 μm and longer beams which are amplitude softening (see Table 2.5). Increasing laser power increases device heating, adding thermal compressive stress. Ignoring imperfections, the linear frequency decreases with compressive stress in pre-buckled beams, while it increases with stress in post-buckled beams [11]. Thus, our measured slope of frequency vs. laser power is consistent with classification of buckling based on nonlinear behavior from Section 2.2.3. Longer beams will develop greater average temperature per unit heat flux, however the frequency shift per unit compressive stress is highest near the buckling length. Thus, the longest and shortest beams have the strongest and weakest relationship respectively between laser power and linear frequency, though the strength is not a strictly increasing function of length. Finally, we note that the 30, 35, and 40 μm beams transition to large amplitude limit cycle oscillations at 128, 32, and 50 μW on sample respectively, making measurement of the linear resonant frequency infeasible. Thus no high power data is plotted for these beams.

Once the doubly-supported beams are in limit cycle motion the LCO fre-

L [μm]	7	10	15	20
"m" $\left[\frac{\Delta f}{f_o \mu W}\right]$	-7.5×10^{-7}	-1.1×10^{-6}	$+1.8 \times 10^{-6}$	$+7.9 \times 10^{-6}$
L (*cont.*)	25	30	35	40
"$m_p re$" (*cont.*)	$+6.2 \times 10^{-6}$	$+6.2 \times 10^{-5}$	$+1.1 \times 10^{-4}$	$+9.5 \times 10^{-5}$

Table 3.3: Change in (linear) frequency per unit power on sample normalized by the (linear) frequency at lowest power on sample measurable. Data is for doubly-supported devices from Chip II. See Figure 3.8 for a plot of measured frequency vs. power in the pre-Hopf regime from which slopes are curve fit.

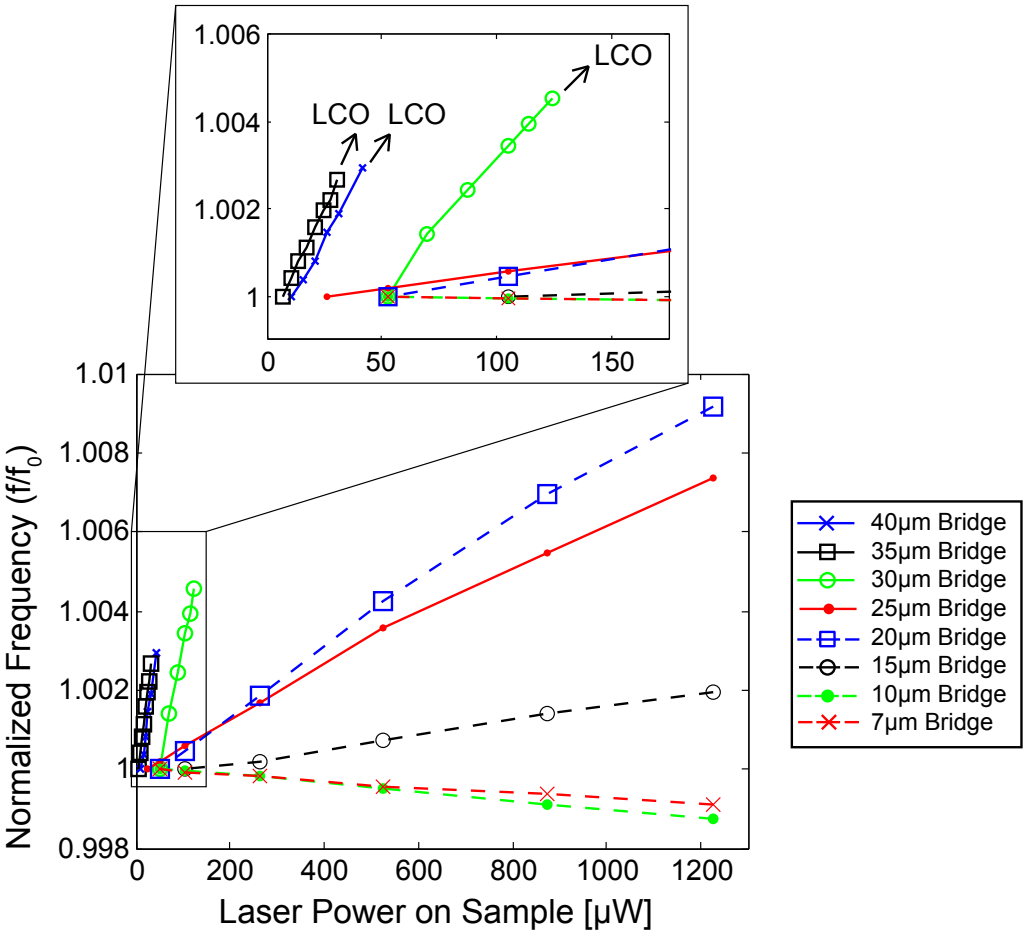

Figure 3.8: Linear resonant frequency as a function of laser power on sample in doubly-supported devices from Chip II. Frequencies are normalized by the frequency at low drive and low laser power. Longer beams (zoom view) transition to large amplitude LCO at $P = P_{Hopf}$ making measurement of the *linear* resonant frequency infeasible for $P > P_{Hopf}$. The minimum power needed to discern resonant behavior is larger for shorter devices, and data points were equally spaced over the relevant range of powers for the device under test.

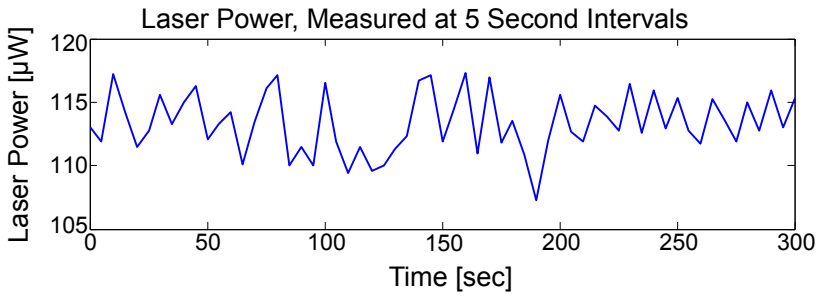

Figure 3.9: Noise in laser power measured at 5 second intervals over 5 minutes. Laser power noise leads to frequency noise through the power-frequency relationship.

quency can be tuned by varying the laser power, i.e. increasing the amplitude of motion. Figure 3.10 plots the frequency vs. laser power for doubly supported beams that are 30, 35 and 40 μm long as well as the 35 μm singly-supported beam. All frequencies are normalized by resonant frequency at low drive amplitude and low laser power, i.e. their linear frequency with negligible thermal stress. Below P_{Hopf} the plotted value is the low amplitude driven resonant frequency, above P_{Hopf} the large amplitude LCO frequency is plotted. In all cases the linear frequency of doubly-supported beams increases slightly as laser power is increased towards P_{Hopf} due to the additional compressive stress from thermal expansion which further arches the already buckled beams [11]. Above P_{Hopf} the amplitude of oscillation increases dramatically and contributes to frequency tuning. First mode vibrations of post-buckled beams are amplitude softening, i.e. the frequency of vibration of a post-buckled beam decreases with increasing amplitude of motion. As was predicted in [9], once in limit cycle oscillation, these tuning mechanisms can compete. Thus, for our post-buckled beams, as the laser power is increased beyond P_{Hopf} the frequency decrease due to amplitude softening competes with the increase in the linear frequency due to thermal stresses.

Considerable frequency noise ($\Delta f/f \approx 4 \times 10^{-3}$) is observed in doubly-supported devices while in limit cycle oscillation due to noise in the laser power combined with a strong relationship between power and frequency. Less than a 0.03% change in the LCO frequency with laser power is seen in the singly-supported beams which do not support membrane stresses and are thus highly linear. As a result they are less affected by noise in the laser power and we observe frequency noise as low as $\Delta f/f \approx 3 \times 10^{-5}$. See Figure 3.9 for a plot of measured laser power - note that the deviation from the mean has a spectral distribution. It is expected that measurement of the Allan variance of the MEMS limit cycle oscillator would reveal a similar structure in the frequency noise, though our spectrum analyzer is not equipped to make these measurements. In addition, we note that variation in the laser power at a frequency greater than the thermal critical frequency (see Section 4.5) should be integrated out by the temperature field and have negligible effect on the frequency noise of the mechanical oscillator.

While the low amplitude frequency of driven oscillation was linear in the power on sample, this is not the case for high amplitude limit cycle oscillations. Generically, the amplitude of a limit cycle should grow with the square-root of the bifurcation parameter past the Hopf bifurcation in a small neighborhood of the bifurcation[121], i.e. $A = c\sqrt{P - P_{Hopf}}$ for $P \approx P_{Hopf}$ with $P > P_{Hopf}$. In addition, the normalized frequency of a Duffing oscillator shifts with the square of the amplitude for small amplitude [101], i.e. $f = 1 + kA^2$ for $A \approx 0$ with $A > 0$. Combining these two equations gives us a linear relationship between amplitude and power: $f = 1 + k\,c(P - P_{Hopf})$. However it is clear from Figure 3.10 that this relationship is not present in the data for the 35 and 40 μm beams except in a *very small* region near $P = P_{Hopf}$. For laser powers greater than P_{Hopf} in

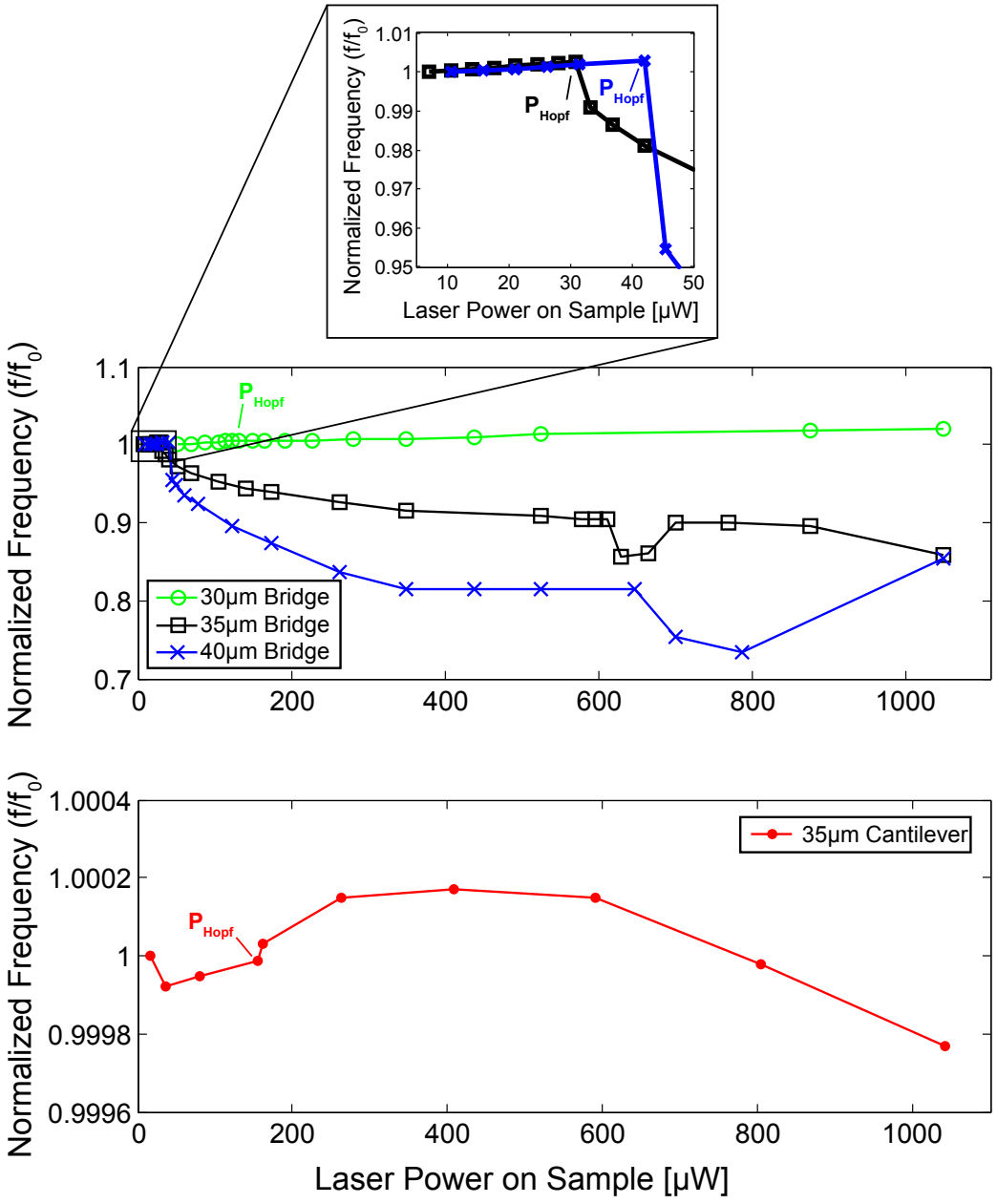

Figure 3.10: Resonant frequency as a function of laser power on sample in doubly-supported devices (top) and a singly-supported device (bottom) from Chip II. Frequencies are normalized by the frequency at low drive and low laser power. For $P < P_{Hopf}$ the linear resonant frequency is plotted, and for $P > P_{Hopf}$ the non-linear frequency is plotted.

these beams, the frequency initially decreases very rapidly, and then begins to level out to a limiting value when P~400 μW on sample. At powers greater than 600μW both the 35 and 40 μm beams have small deviations in their amplitude which are mirrored in the frequency. At this point, movement through the interference field produces strong harmonics, which may be responsible for this small deviation. Taking the first point before and first two after the Hopf, we get a least squares fit change in frequency per unit power in the post-Hopf region given in Table 3.4. Comparing this to the pre-Hopf data from Table 3.3 we note that the change in frequency per unit power in the 30 μm beam decreased slightly post-Hopf, while it changed signs and increased in magnitude by 1 or 2 orders of magnitude in the 35 μm and 40 μm beams respectively.

L [μm]	30	35	40
"m_{post}" $\left[\frac{\Delta f}{f_o \mu W}\right]$	$+1.4 \times 10^{-5}$	-2.6×10^{-3}	-7.9×10^{-3}

Table 3.4: Change in (non-linear) frequency per unit power on sample normalized by the (linear) frequency at lowest power on sample measurable. Data is for doubly-supported devices from Chip II. See Figure 3.10 for a plot of measured frequency vs. power in the post-Hopf regime from which slopes are curve fit.

The observed frequency tuning behavior was consistent between doubly- and singly-supported devices of the same length from Chips I and II for all but the 30 μm doubly-supported beams. As noted in Section 3.1, because of their location near a peak in the absorption curve, devices of this length are most sensitive to differences in out-of-plane displacement due to variations in chip device layer thickness. Despite a relative difference of only 1.4% in device thickness (see Table 2.1), limiting amplitudes of oscillation in these devices were seen to have a relative difference of ~40% (see Figure 3.4). Figure 3.11 plots the frequency vs. laser power for 30 μm beams from Chips I and II. For both beams,

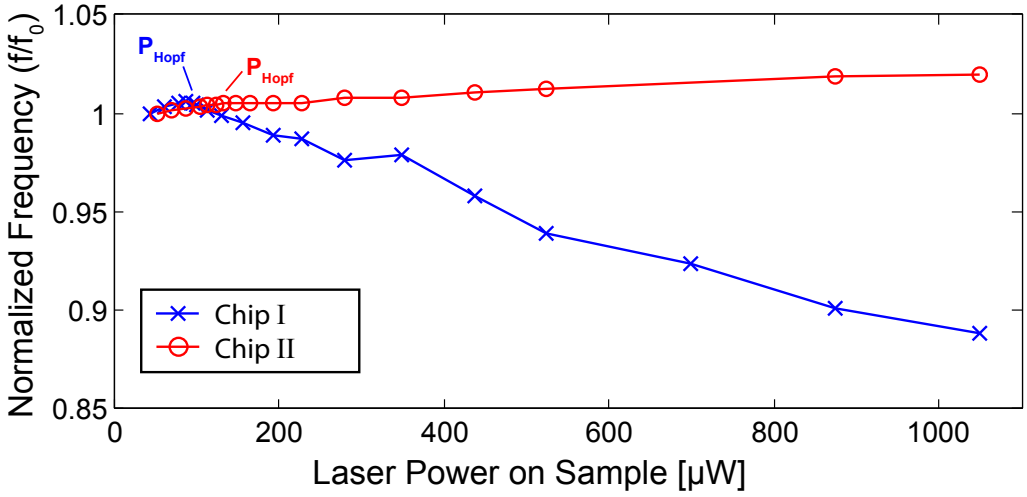

Figure 3.11: Resonant frequency as a function of laser power on sample in 30 μm doubly-supported devices from Chips I and II. Frequencies are normalized by the frequency at low drive and low laser power.

the frequency of oscillation increases slightly with laser power for $P < P_{Hopf}$. For the 30 μm beam from Chip II post-Hopf, the amplitude of oscillation increases to ~90 nm, and the frequency increases slightly, while for the 30 μm beam from Chip I, a higher limiting amplitude of ~ 140 nm allows amplitude softening to dominate leading to a frequency which decreases with laser power. For laser powers on sample greater than 700 μW, the amplitude of oscillation was seen to begin to decrease in the 30 μm beam from Chip I, though the frequency appears unaffected.

3.3 Frequency Entrainment

In this section, we present experimental results on entrainment for singly- and doubly-supported beams. We start by showing the statistics of entrainment for low drive amplitudes, A_D. Then we illustrate how the laser power changes the region in $f_D - A_D$ parameter space for which devices are 1:1 entrained. Finally we map out the region of 1:1 entrainment in a singly-supported beam and regions of 1:n and n:1 entrainment in a doubly-supported beam. A general overview of this phenomenon is presented in Section 1.4, and experimental procedures are discussed in Section 2.4.4.

Entrainment Statistics, 35 μm Doubly-Supported Beams:

Due to the high level of frequency noise in our doubly-supported beams[2], a self-oscillating device may jump in and out of entrainment for fixed drive frequency and amplitude, causing entrainment to be an inherently statistical phenomenon. To study the statistics of entrainment, we subject a 35 μm beam from Chip I to centerline illumination with fixed the laser power of 1050 μW, leading to $f_{LCO} = 1.63 \pm 0.0065$ MHz. We measured the region of entrainment for 100 successive sweeps up and down using a filtered sweep (see Section 2.4.4) with sweep rate of $1 \frac{kHz}{sec}$. Using $\tau = \frac{Q}{\pi f}$ as the settling time, at this sweep speed, the drive frequency changes by ~ 6 Hz during one settling span, well below our minimum detectable entrainment span. Thus we can assume the change in the drive frequency to be quasi-static.

[2]One standard deviation of the frequency measured between successive 161ms sweeps is $\frac{\Delta f}{f} \approx 4 \times 10^{-3}$ at 1050 μW for a 35 μm doubly-supported beam subject to centerline illumination.

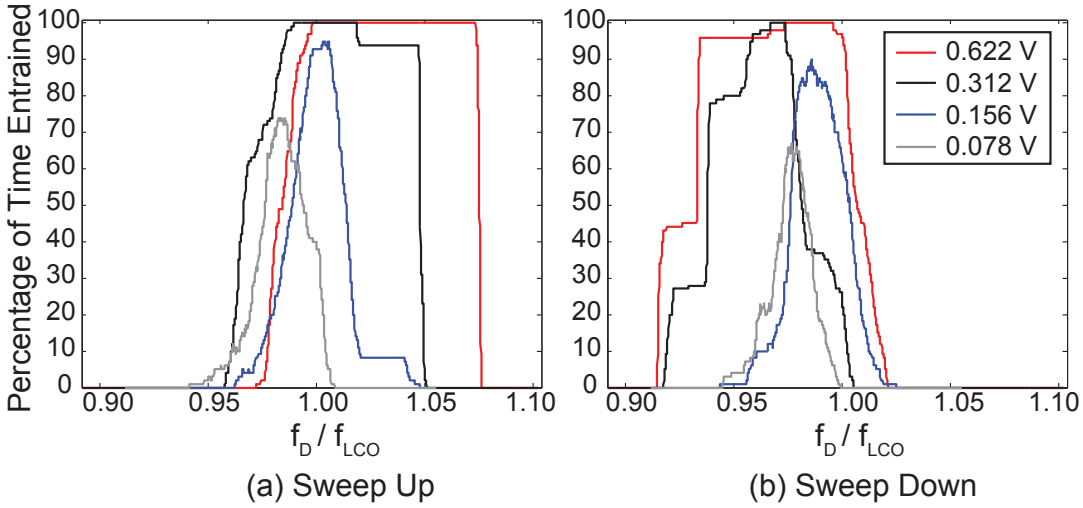

Figure 3.12: Statistics of entrainment for a $35\mu m$ doubly-supported beam from Chip I under 1050 μW laser power, measured using the spectrum analyzer as a drive source. Drive frequency, f_D is normalized by the undriven limit cycle frequency f_{LCO}.

The points at which locking starts and stops varies from sweep to sweep. In addition, on a given sweep, the oscillator moves in and out of entrainment. Statistics of entrainment are given in Figure 3.12. For low drive amplitudes the limit cycle is only entrained part of the time even when $f_D \approx f_{LCO}$, i.e. for the lowest drive amplitude shown, $V_D = 0.078V$, there was no drive frequency at which the oscillator was entrained on every sweep. This is in sharp contrast to the typical entrainment scenario (see Figure 1.3). Increasing the drive amplitude increases the width of the entrainment region on any given sweep, sharpens the edges of the region of entrainment and allows for "strong locking", where the limit cycle is seen to be entrained at a given frequency on every sweep. Note that the entrainment region depends on sweep direction due to asymmetry and hysteresis in the system. For example, when sweeping up in frequency with $A_D = 0.622V$, locking occurs when f_D is 2% below f_{LCO}, but is maintained up to 7% above f_{LCO}. Sweeping down, locking occurs when f_D is 2% above f_{LCO} and

is maintained down to 7% below f_{LCO}.

1:1 Region of Entrainment, 35 μm Doubly-Supported Beams:

The region of 1:1 entrainment in the 35 μm doubly-supported beam was measured using an unfiltered sweep, with the laser power set to P=105, 525 and 1050 μW. See (Figure 3.13) for a plot of the results. Data is un-averaged leading to a non-smooth boundary of the entrainment region due to frequency noise, i.e. statistics. Note from Section 3.2 that changing the laser power changes the operating point on the backbone curve. Thus, by selecting a laser power we select both the frequency of oscillation, f_{LCO}, and amplitude-frequency relationship in the neighborhood of f_{LCO}: for P=105 μW we have f_{LCO} = 1.91 MHz and a locally steep amplitude-frequency relationship (see Figure 3.7); for P=525 μW we have f_{LCO} = 1.84 MHz and a moderately steep amplitude-frequency relationship; and for P=1050 μW we have f_{LCO} = 1.63 MHz with fairly flat amplitude-frequency relationship (not shown in Figure 3.7).

It has been shown that an amplitude-hardening limit cycle oscillator is constrained to the backbone curve when entrained, giving asymmetry in the region of entrainment with a right-tilted V shape [91, 142]. In this work we see that the same is true for amplitude-softening limit cycle oscillators, with the direction of tilt switched - higher amplitudes of forcing result in higher amplitude oscillations which push the oscillator up the backbone curve, decreasing the frequency at which the oscillator entrains. This effect is most evident in the data for P=1050 μW. A shift in the entrainment frequencies for high amplitude forcing has also been demonstrated in models with no softening or hardening behavior [120].

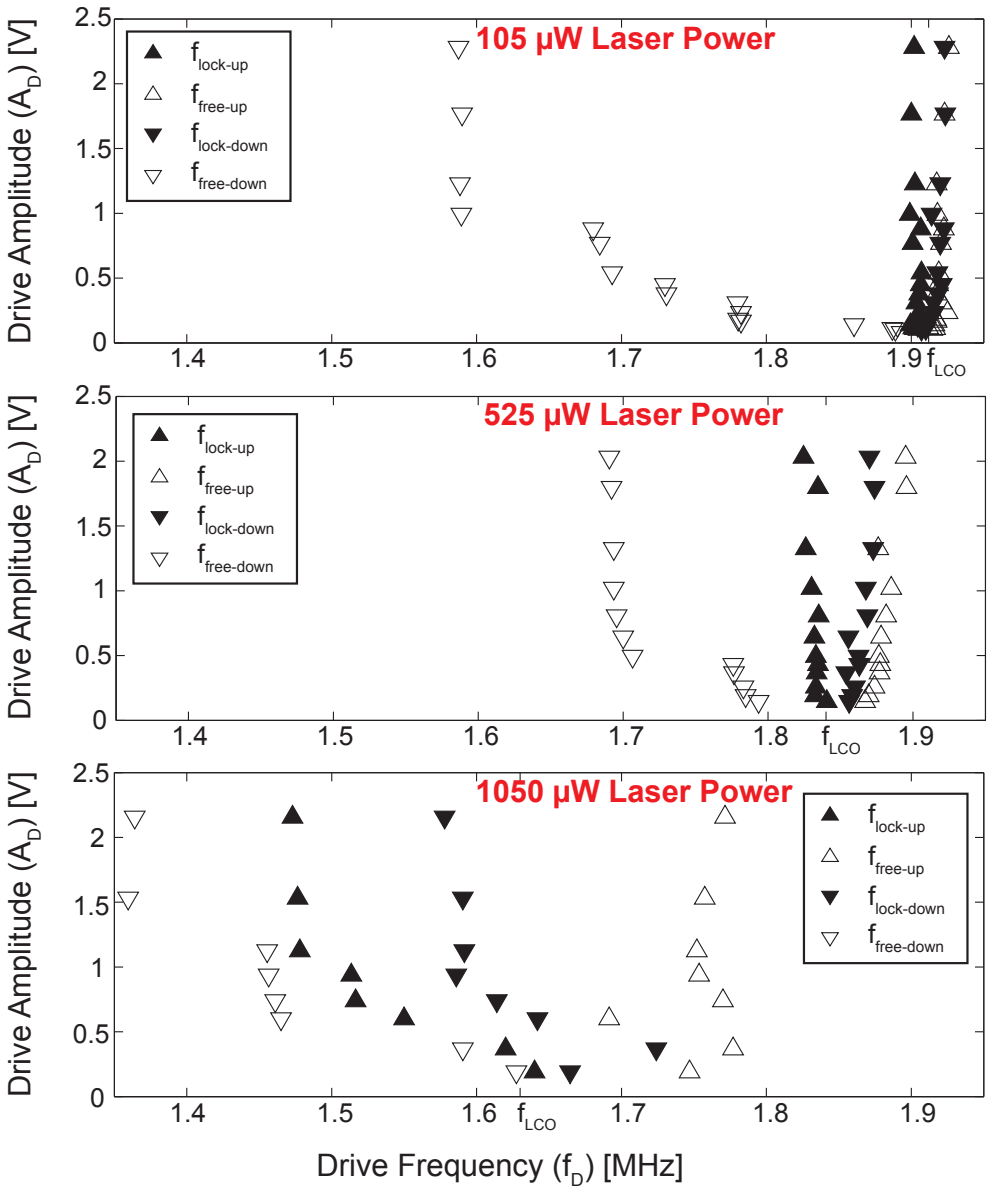

Figure 3.13: Regions of 1:1 entrainment in a 35μm doubly-supported beam from Chip I as a function of laser power on sample.

In addition, by selecting our operating point, we can tune the asymmetry in the region of entrainment. Examining the data for P=105 μW we see that when sweeping up in frequency, locking does not occur until f_D is very close to f_{LCO} but then is quickly lost, since the amplitude is driven down to zero at the base of the backbone curve at $f \approx 1.92$ MHz (see Figure 3.7). When sweeping down in frequency, f_D must be similarly close to f_{LCO} in order to lock, however once locked the limit cycle may be pushed up the backbone curve by as much as 15% (see Figure 3.13).

Regions of 1:n and n:1 Entrainment, 35 μm Doubly-Supported Beams

Preliminary results showed that the order of sub- and superharmonic entrainment possible did not depend on the laser power selected, thus regions of superharmonic (Figure 3.14), and subharmonic (Figure 3.15) entrainment were measured at a single power of P=1050 μW for the same 35 μm doubly-supported device.

Note that for the same forcing amplitude, A_D, the width of the entrainment region is lower for higher order superharmonic entrainment (Figure 3.14). This is likely due to a combination of two factors. First of all, when superharmonically entrained at 1:n, if the drive frequency, f_D, increases by 1 Hz then the limit cycle frequency, f_{LCO}, increases by n Hz. Thus a small width of entrainment measured in terms of changes in f_D is large when measured in terms of f_{LCO}. In addition, the efficiency of energy pumping decreases for increasing order of entrainment, transfer being most efficient when the frequency of response matches the drive frequency. In the language of perturbation theory: primary entrainment may be obtained with "soft" excitation where the amplitude of excitation

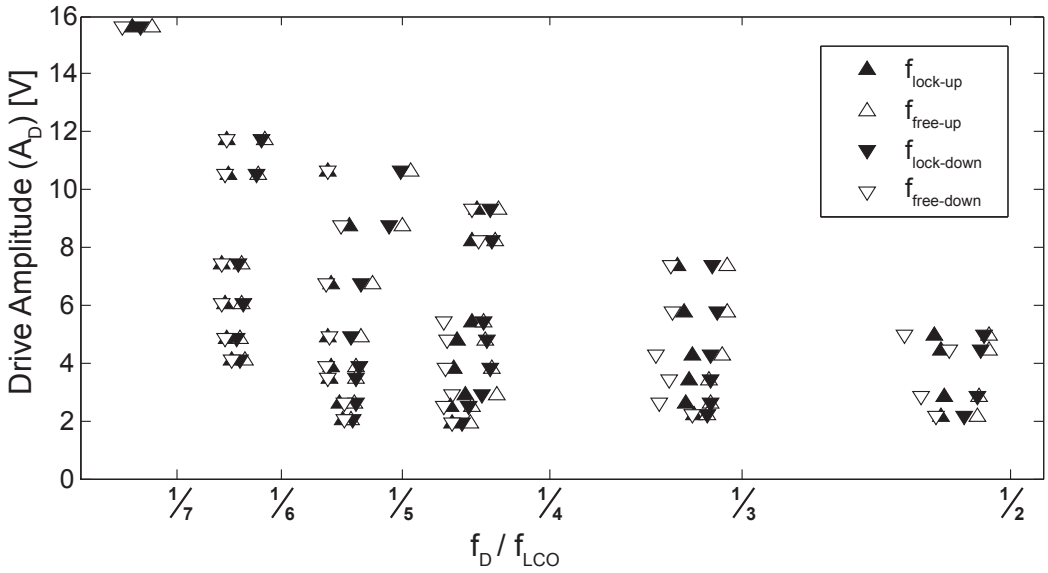

Figure 3.14: Regions of superharmonic entrainment for a 35μm doubly-supported beam under 1050 μW laser power. The drive frequency, f_D, is normalized by the undriven limit cycle frequency f_{LCO} = 1.63 MHz. A logarithmic frequency scaling is used in order to display all measured regions on the same plot.

is the same order as the damping and nonlinear terms; however, sub- or superharmonic entrainment require that the excitation be "hard," i.e. scaled one or more orders higher than the damping and nonlinear terms [86]. Superharmonic entrainment of order 1:7 is only observed in our devices at the highest achievable drive amplitude, and 1:8 entrainment is not observed. See Figure 3.16 for oscilloscope traces of 1:3 superharmonic, 1:1 primary, and 3:1 subharmonic entrainment.

In the subharmonic case, the width of entrainment at 3:1 appears to be slightly larger than for 2:1 at the same forcing amplitude (see Figure 3.15). This is likely due to the fact that for n:1 subharmonic entrainment, an increase in f_D by 1 Hz leads to a (1/n) Hz increase in f_{LCO}, artificially increasing width of

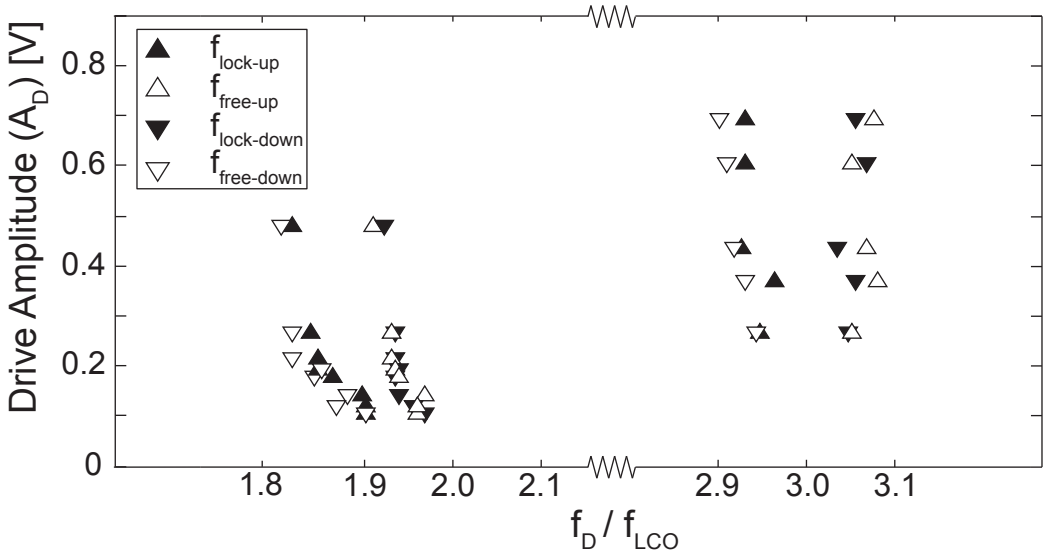

Figure 3.15: Regions of subharmonic entrainment for a 35μm doubly-supported beam under 1050 μW laser power. The drive frequency, f_D, is normalized by the undriven limit cycle frequency f_{LCO} = 1.63 MHz.

entrainment for subharmonic forcing when measured with respect to the drive frequency. Subharmonic entrainment at 4:1 or higher was not observed. Measured by changes in f_D or f_{LCO}, the largest region of entrainment is seen for 1:1 forcing. For primary, sub- and superharmonic entrainment, the width of the entrainment region increases with A_D as expected - stronger forcing can entrain the limit cycle at larger frequency detuning. Finally we note that 1:n superharmonic entrainment is seen to occur at frequencies slightly less than $(1/n)f_{LCO}$. This may also be related to the amplitude-frequency relationship though more work is needed to determine the exact cause.

1:1, 1:n, and n:1 Entrainment, 35 μm Singly-Supported Beams

We also examined entrainment in a 35 μm singly-supported beam on Chip

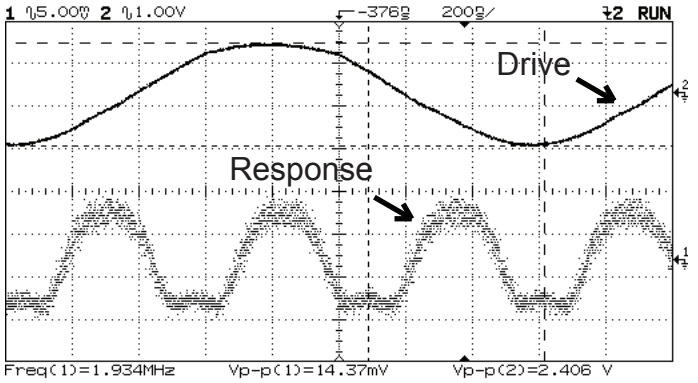

(a) 1:3 Superharmonic Entrainment

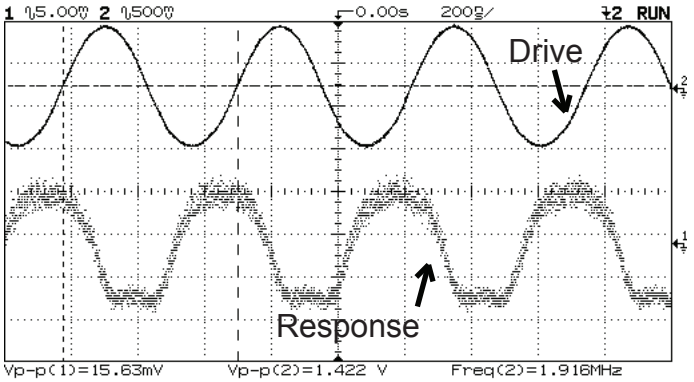

(b) 1:1 Entrainment

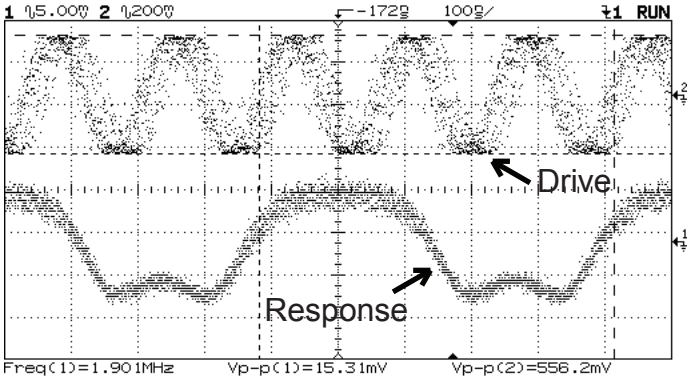

(c) 3:1 Subharmonic Entrainment

Figure 3.16: Oscilloscope traces showing 1:3 superharmonic, 1:1 primary, and 3:1 subharmonic entrainment for a 35μm doubly-supported beam under 1050 μW laser power. Note that for subharmonic entrainment, we trigger on the return signal rather than the drive (see Section 2.4.4). As a result, the drive signal appears noisy due to noise in the (triggered) response signal.

I at P=700 μW laser power. Since singly-supported beams do not support in-plane tension, they are highly linear. Significantly less frequency noise was observed[3], in addition to a much smaller region of 1:1 entrainment: compare a relative frequency width of $\sim 0.45\%$ in the singly-supported device versus $\sim 25\%$ in the doubly-supported device[4], both at the same forcing level of $A_D = 1.5V$. The frequency at which entrainment was lost when sweeping down ($f_{free-down}$) was seen to be roughly independent of drive amplitude. For these negative detunings, even when the drive amplitude is low, traces of the response seem to indicate quasi-periodic motion - i.e the response signal appears to have two frequency component (see Figure 3.18), with the lower frequency equal to the drive frequency. However, note that in our experimental setup we do not measure the displacement directly, but rather the convolution of reflectance as a function of position with position as a function of time (see Section 2.4.5). The former is periodic in $\frac{\lambda}{2} \approx 316$ nm. As a result high amplitude oscillation at a frequency of f_0 introduces strong $n \times f_0$ components in the reflected signal. Given cantilever tip deflections of $O(1000)$ nm (see Section 2.2.3), it is possible that these traces are due to high amplitude motion of the device through multiple periods of the interference field. However trace data cannot be accurately produced by the methods outlined in Section 2.4.5 even for high amplitude motion.

Finally we note that neither subharmonic nor superharmonic entrainment were seen in any of the singly-supported devices, perhaps due to their lack of an amplitude-frequency relationship. Prior experimental work on subharmonic entrainment suggests that non-sinusoidal motion found in relaxation

[3]We measure $\frac{\Delta f}{f} \approx 3\times10^{-5}$ at 700 μW in the 35 μm singly-supported beam versus $\frac{\Delta f}{f} \approx 4\times10^{-3}$ at 1050 μW in a doubly-supported beam of the same length.

[4]Direct comparison is challenging due to the frequency dependent electrical and mechanical impedance of our piezo-drive (see 2.4.4), and the order of magnitude difference in resonant frequencies between the 2 devices.

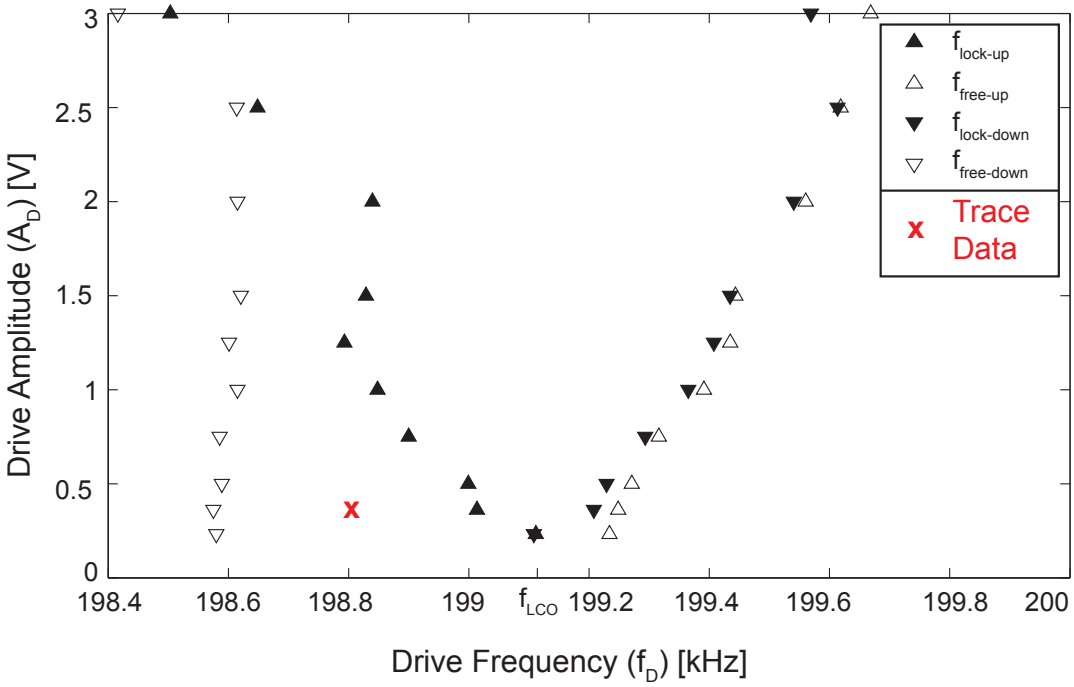

Figure 3.17: Region of 1:1 entrainment for a 35 μm singly-supported beam under 700 μW laser power. See Figure 3.18 for an oscilloscope trace data at the point in parameter space indicated.

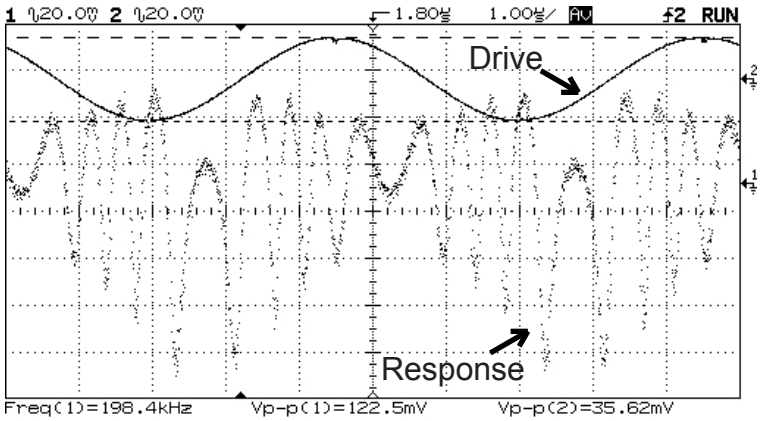

Figure 3.18: Oscilloscope trace showing primary entrainment for a 35 μm singly-supported beam under 700 μW laser power in the region of negative detuning. See Figure 3.17 for the drive frequency, f_D, and amplitude, A_D used here.

oscillations or large amplitude motion of a Duffing oscillator allow for higher order entrainment and large regions of 1:1 entrainment: Van der Pol's original work demonstrating 200:1 subharmonic entrainment was on a relaxation oscillator - a highly nonlinear oscillator with two-time scale motion; Shim et al.'s demonstration of high order superharmonic resonance was also in doubly-supported beams which support mid-plane stretching; Finally, Zalalutdinov et al. [142] worked on mushroom-like resonators supported by a central pillar, which should be less affected by midplane stretching and thus linear. They were only able to demonstrate 2:1 subharmonic entrainment, not superharmonic entrainment nor higher order subharmonic entrainment.

CHAPTER 4

MODELING AND ANALYSIS

For interferometric transduction of MEMS resonators to be a viable means of producing periodic motion, first the mechanisms and conditions for self-oscillation must be understood, and then models developed that predict the minimum laser power needed for self-oscillation. In this chapter, we analyze the thermo-optical forces underlying limit cycle oscillations in doubly-supported beams. Model equations are then derived and analyzed to: predict the threshold power for self-oscillation; and understand the frequency tuning in large amplitude vibrations. Modeling of experimental results on entrainment is forthcoming.

Anchor Deformations and Thermo-Mechanical Coupling

Prior analyses of self-oscillation in optically-transduced MEMS devices agree that feedback is due to coupling between heating, displacement, and absorption (see 1.2 for a review). In particular Langdon and Dowe describe the feedback gain as a product of: laser power; displacement per unit power absorbed (thermo-mechanical coupling); and change in percentage absorption per unit displacement (absorption contrast). Initial work focused on beams with metallic surface coatings which confined absorption to the top surface creating thermal gradients which drove deformation. However, it is not clear how heating leads to displacement (i.e. the cause of thermo-mechanical coupling) in initially flat, un-coated beams.

In Section 4.4 we analyze reflection, transmission and absorption within a

thin film stack, and show that for thin uncoated devices laser absorption is periodically distributed throughout the interior of the device, and not confined to the surface. A finite element model of a doubly supported beam subject to steady state heating across it's midline interior is then analyzed in Section 4.1 using the commercially available software package, ANSYS. Results show that deflection due to heating comes from a combination of: thermal gradients at the support which tend to bend the device down towards the substrate due to the "thermostat effect"; and compressive stresses at the beam's support which tend to bend the device up away from the substrate due to asymmetry in the support geometry. In doubly-supported beams the latter out-competes the former, and thus beams bend away from the substrate when heated, with deformation driven by the in-plane average temperature. This result allows us to interpret the direct thermo-mechanical coupling as the slope of the (thermal) load curve, and later model the temperature field using a 1D continuum. In addition, it indicates that the phase of feedback (direction of deflection) for doubly- and singly-supported beams at the same location within the interference field differs by 180°.

Calculated thermo-mechanical couplings are then incorporated into an existing ad-hoc model of laser-interference transduced MEMS built using a nonlinear oscillator model coupled to a lumped thermal parameter model. Results suggest that barely post-buckled beams should have low threshold powers for self-oscillation. Finally the limitations of lumped parameter modeling are investigated in Section 4.5.

Continuation of Model Equations

Previous work [7, 144] on modeling the dynamics of limit cycle oscillations in optically driven MEMS resonators has assumed small displacement and expanded the function describing the interference field in a power series, losing the periodicity in the process. In Section 4.2, we treat the case where displacement is not small and show that a periodic interference field suggests the coexistence of multiple stable limit cycles. To our knowledge, multiple *stable* limit cycles have not been predicted or seen experimentally in previous work on MEMS. Devices exhibiting multiple stable limit cycles would allow for tuning between distinct frequency bands, and within them in applications such as GPS receivers.

Numerical continuation allows us to calculate the frequency of large amplitude vibrations in the model, and results show competition between linear frequency tuning and non-linear frequency tuning as is seen in the experimental data presented in Section 3.2. Conditions necessary for observing multiple stable limit cycles are outlined and include: temperature dependent stiffness; high quality factor; and large gap-to-substrate. Predicted amplitudes of oscillation for higher order limit cycles are greater than the gap-to-substrate in our actual devices, and thus these motions were not observed experimentally. Finally, we also find that the small displacement assumption suppresses other behavior such as secondary Hopf bifurcations, and period doubling which are picked up using numerical continuation.

First Principles Model

Models of device dynamics have also been constructed by prior researchers. Variations of a coupled oscillator model are used to model device dynamics in [7, 144, 145, 91]. Perturbation theory is used to estimate the threshold power

for self-oscillation in [7, 144]. While the past models prove to be accurate, they requires extensive finite element analysis (FEA) to compute model parameters which are specific to a single device. As such, it is difficult to make predictions based off the model since parametric FEA must be performed if any device property such as length or thickness were to be varied.

Motivated by the need to understand the contributors to low power self-resonant devices at the level of device design, and build predictive models, in Section 4.3 we sacrifice accuracy for ease of use and present an (almost) parameter free model of interferometrically driven self-resonant doubly-supported beams. Perturbation analysis is used to predict the threshold power for self-oscillation, and compared with the results of numerical continuation, and experimental results. Scalings of threshold power with device geometry and pre-stress are discussed.

In addition, the mechanical model derived provides the basis for discussion of stiffness non-linearities of doubly-supported beams exhibiting "imperfection" buckling. Analysis of the amplitude-frequency relationship as a function of device pre-stress discussed in Section 1.3 is backed up with theoretical predictions of linear frequency tuning and stiffness non-linearities in Appendix B.

4.1 Anchor Deformations and Thermo-Mechanical Coupling

Prior models show that the threshold power for self-oscillation in MEMS devices depends on the direct feedback between static heating and displacement [19, 67, 63, 35, 55, 54, 7, 45, 145, 144] , yet it is unclear what mechanism causes

the displacement in initially straight doubly-supported beams. In this section, a finite element method (FEM) model of a doubly-supported beam subject to steady state heating[1] is analyzed using the commercially available software package, ANSYS. Results show that deflection due to heating comes from a combination of thermal gradients and compressive stresses at the beam's support. We then illustrate the importance of this direct thermal-mechanical coupling mechanism in driving interferometrically transduced self-oscillation. Material from this section is drawn from work published in Finite Elements in Design and Analysis [10].

4.1.1 Materials and Methods

The analysis will model doubly-supported beams fabricated out of silicon-silicon dioxide-silicon (SOI) wafers. The beams are 7,10,15 or 20 μm long, 201 nm thick, 2 μm wide with 2 μm of undercutting, and a 400 nm gap to substrate. Resonant frequencies are measured to be 17.2, 10, 5.0 and 3.6 MHz respectively[2]. SEM images show that the 20 μm beams are post-buckled, indicating a residual compressive pre-stress σ_{res} in the device layer that is greater than the buckling load (σ_b) of the 20 μm beam and less than that of the 15 μm beams (see Section 2.2.3). Thermal-mechanical coupling is found to be highly dependent on the pre-stress, so a careful analysis of the buckling loads is done to bracket the pre-stress in the devices. To estimate the buckling loads and study the thermal-mechanical coupling, FEM models of each beam were built incorporating the beam and a large portion of the surrounding substrate. Quarter symmetry was

[1] See Section 4.5 for rationale behind steady-state analysis and subsequent lumped parameter modeling.

[2] These frequencies were measured on Chip 0, and are comparable to those from Chips I and II. See Section 2.2.2 for a list of measured resonant frequencies.

used to reduce the problem size.

Thermal and mechanical boundary conditions for the model are shown in Figure 4.1(a). In order to account for the estimated pre-stress, the corresponding strain was calculated and equivalent step displacement Δy_{eq} applied to the midline cross section. Symmetry, clamped, or free boundary conditions were applied to the remaining surfaces of the model. We assume that the laser is focused on the center of the beam. Given that the devices are optically thin, absorption is not confined to the top surface (see Section 4.4). Thus we consider the power to be evenly absorbed throughout the thickness of the beam, and apply a heat flux H_0 equivalent to 1mW of incident laser power (4.4% absorbed) to the midline cross section. The substrate outside the model is assumed to be an infinite heat sink. Since devices operate in vacuum, with small temperatures above ambient, convective and radiative heat loss are negligible. A representative mesh is depicted in Figure 4.1(b), and the material properties used are listed in Table 2.2. Note the two order of magnitude difference between the thermal conductivity of Si and SiO_2.

Recall that pre-stress in our devices is bracketed by the buckling loads (σ_b) of the 15 μm and 20 μm beams. In order to calculate σ_b for each beam, the temperature is fixed at zero and the (horizontal) midline displacement is varied in a large deflection static analysis (NLGEOM ON, PSTRES ON) to produce a load curve. Note that the top of the device layer is surrounded by vacuum, while the bottom of the device layer is bonded to the underlying oxide layer. This geometric asymmetry of the anchor support is captured in the boundary conditions imposed in the model and causes imperfection buckling[3]. Since the

[3]Optical profilometry data available after this FEM analysis was published showed that imperfection levels in our actual devices where 40-55× higher than those predicted here, and pointed to residual stress gradients as a large contributor to device imperfection. See Section

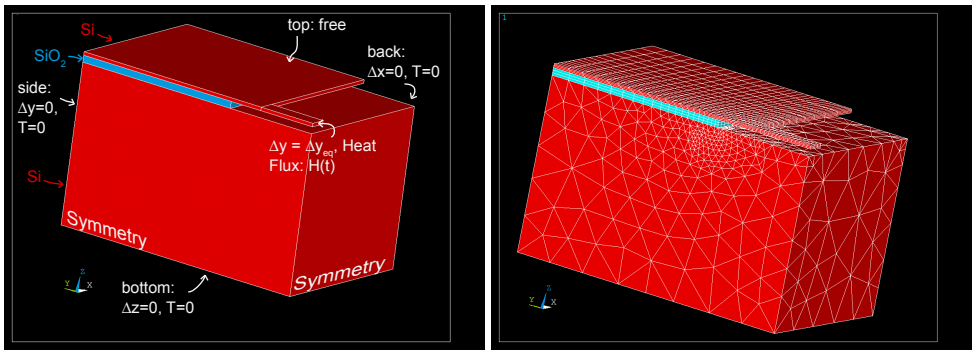

(a) Boundary Conditions (b) Mesh

Figure 4.1: Structural and thermal boundary conditions as well as mesh for a FEM model of a 7 μm beam. For each model, the precise temperature field and displacement due to steady state heating was calculated using a very fine mesh. Then the mesh coarsened such that maximum temperature and vertical component of the midline displacement were accurate to within 2%. This mesh convergence study indicated the need for a high density of elements at the support.

top surface of the device layer is free, shear stresses develop along the bottom of the device layer in the region of the support to counteract axial compressive stresses due to pre-stress. These shear stresses act below the beam centerline and tend to arch the beam up away from the substrate. Once the compressive stress reaches a critical load, (σ_b), the growth becomes dramatic (see Figure 4.2). This load is slightly less than the buckling load predicted by a Euler-Bernoulli beam theory model of an initially straight clamped-clamped beam. Analysis of the 15 μm and 20 μm beams indicates the presence of 55±10 MPa of compressive pre-stress.

Having estimated the pre-stress, we apply equivalent step displacements Δy_{eq} to each beam, and calculate the midline displacement due to pre-stress alone using a large-deflection static analysis (NLGEOM, ON) which accounts

2.2.3 for optical profilometry data and Appendix A for a quantitative analysis.

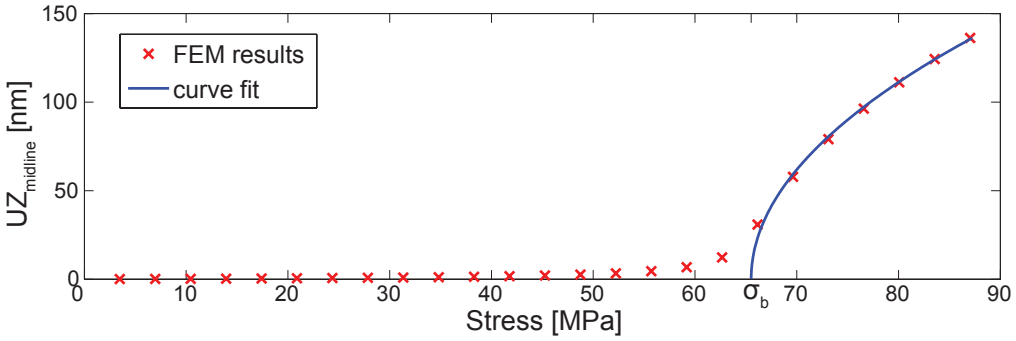

Figure 4.2: Load curve for the 15 μm beam. Note that undercutting artificially softens the beam support reducing the buckling load and resonant frequency, thus making the beam "effectively" longer. The equivalent length (see Section 2.2.2) is used to relate stress to displacement from $\Delta y = \frac{\sigma L}{2E}$ and to approximate the buckling stress for the 7,10 μm beams where a full non-linear FEM buckling analysis was not done. Thermal-mechanical coupling is found to depend critically on residual pre-stress, particularly in the neighborhood of σ_b (see Section 4.1.4). Thus careful analysis of σ_{res} is required. To find the buckling load (σ_b), we curve fit the post-buckled load curve to a square root.

for geometric non-linearities. In addition, we select (PSTRESS, ON) so that the stiffness matrix is recalculated in the deformed configuration. Next we turn our attention to the thermal model. A steady state thermal analysis is performed to calculate the temperature distribution in the beam. Equivalent structural loads are applied by switching the element type from thermal to structural and the large deformation static problem including pre-stress effects is solved to find the vertical component of the midline displacement due to pre-stress and heating. The difference between these displacements, ΔUZ, provides us a measure of the thermal-mechanical coupling.

4.1.2 Results

In doubly-supported beams, deflection due to heating is the result of two competing effects. First of all, heat propagates more efficiently in the device layer because the thermal conductivity of silicon is two orders of magnitude higher than that of the underlying silicon dioxide layer [55, 54]. Heat from the laser, applied at the center of the beam travels along the beam and is sunk at the anchor by flowing into the low conductivity oxide. This sets up a large vertical temperature gradient in the oxide near the support (Fig. 4.3(a)). The device layer, being hotter than the oxide layer expands more, and the mismatch in thermal expansion coefficients between the layers (see Table 2.2) augments this affect to create a bending moment that tends to rotate cantilevered beams down toward the substrate via the "thermostat effect". Secondly, in doubly-supported beams compressive stresses across the length of the device due to pre-stress *or* thermal expansion have the opposite effect: a phenomenon noted in the previous section. For the beams studied, the effect of the thermal compressive force dominates the effect of the vertical thermal gradients, causing the beams to arch up away from the substrate when heated. Note that the direction of deflection due to heating is particularly important since a change in direction is a 180° phase shift within the feedback loop. Assuming small displacements, we define the thermo-mechanical coupling coefficient as

$$D = \frac{\Delta UZ}{T_{ave}} \tag{4.1}$$

where ΔUZ is the vertical component of the displacement at the center of the beam and T_{ave} is the average temperature in the beam. In calculating the coupling, we include only the displacement due to heating, not the portion due to

pre-stress. This coefficient is roughly equivalent to the local slope of the load-displacement curve in Figure 4.2 where excess temperature is transformed to thermal stress load. Note that the analysis is inherently non-linear in both the initial stress state, σ_{res}, and applied heat flux H_0. See Table 4.1 for a list of results. The 20 μm beams being post-buckled, have the greatest thermal-mechanical coupling (highest slope), while the 15 μm beams being nearly buckled have the second greatest thermal-mechanical coupling.

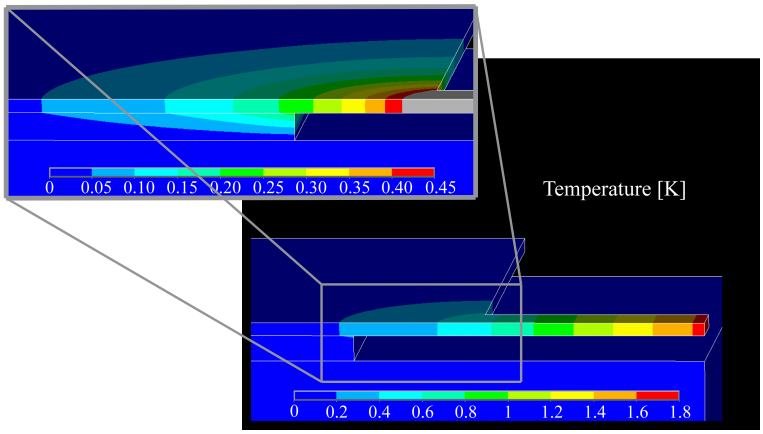

(a) Temperature

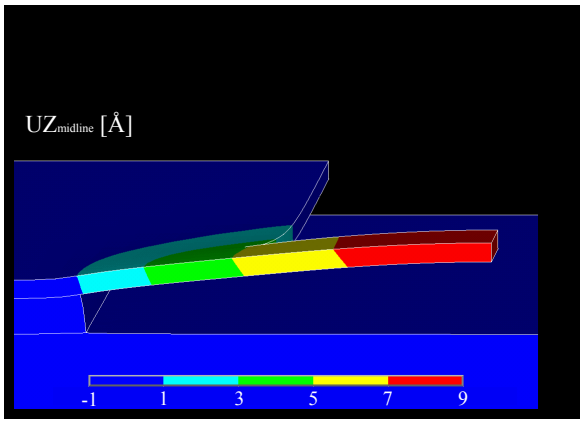

(b) Deflection

Figure 4.3: Temperature distribution and deflection for the 7 μm beam under steady state heating - note that a portion of the displacement is due to pre-stress.

4.1.3 Discussion

We do not vary the laser power in the FEM model directly in order to determine the threshold power for self-oscillation because of the computational cost of solving the coupled thermal-mechanical problem[4]. Rather, we build on past work by using our finite element analysis (FEA) results to populate parameters in a simple analytic model which has already been studied. Variations of the model have been presented in [7, 106, 91, 145, 144], and the interested reader should refer there for more details on its derivation. Below, the model is discussed and model parameters estimated. We note the two differences between the following model and that presented later in Section 4.3 of this dissertation: extensive FEA is needed in order to determine model parameters here; and the periodicity in the interference field is included here[5].

Although physical devices have spatially varying fields, first mode vibration is assumed and the midline displacement (z) is modeled as a one degree-

[4]Such an approach has been applied to a similar problem by Salinger et al. [107] who perform bifurcation theory within the context of large scale models arising from coupled partial differential equations. Their test-problem is that of Rayleigh-Bénard convection. Software is available from Sandia National Laboratories in the `Library of Continuation Algorithms`.

[5]Periodicity of the interference field is neglected in Section 4.3, since the objectives of that work are to: predict P_{Hopf}, a quantity which depends only on the local slope of the interference field; and formulate model parameters without the need for extensive FEA analysis.

Length	7 μm	10 μm	15 μm	20 μm
ΔUZ [Å]	0.0364	0.0930	2.17	33.6
T_{ave} [K]	0.831	1.07	1.48	1.88
D [$\frac{\text{Å}}{K}$]	0.0219	0.0434	0.734	8.96

Table 4.1: FEM results of thermal-mechanical analysis. $\Delta UZ_{midline}$ is the vertical component of the displacement at the center of the beam due to heating with reference to the pre-stress configuration. Note that the thermal-mechanical coupling coefficient (D) increases with length.

of-freedom oscillator. The average temperature in the device (T) is modeled using a lumped thermal model. Note that heating causes compression which changes the stiffness to out-of-plane deflection giving us a temperature dependent linear stiffness $k = k_0(1 - \frac{T}{T_{buckle}})$, with $T_{buckle} = \frac{\sigma_b - \sigma_{res}}{\alpha_e E}$, the temperature at which a Euler-Bernoulli beam buckles due to thermal stresses. This relationship recovers exactly the frequency-compression relationship for pre-buckled beams [131] and is approximately correct for post-buckled beams [11]. Furthermore, the slope of a load vs. displacement curve increases with displacement due to membrane stresses, giving a cubic stiffness βz^3 [29]. Including damping and the thermal-mechanical coupling term, as well as non-dimensionalizing time by the beam's measured resonant frequency and non-dimensionalizing displacement by the laser wavelength, we get the following model of the first translational mode of vibration:

$$z'' + \frac{z'}{Q} + \left(1 - \frac{T}{T_{buckle}}\right) z + \beta z^3 = DT \tag{4.2}$$

The average temperature is assumed to change according to Newton's law of cooling, giving

$$T' = -BT + HP_{absorbed}(z) \tag{4.3}$$

where H is the inverse of the lumped thermal mass, B is the cooling rate due to conduction, and $P_{absorbed}(z)$ is the laser energy absorbed as a function of deflection. This final term describes the Fabry-Pérot interferometer and has been previously modeled as

$$P_{absorbed}(z) = P(\alpha + \gamma \sin^2(2\pi(z - z_0))) \tag{4.4}$$

with α,γ and z_0 fitting parameters that depend on the device thickness and material properties, and P the incident CW laser power[6].

Estimation of the physical, thermal, and optical parameters is done using a number of different analyses. The optical parameters α, γ, and z_o are least squares fit to the numerical results from the model presented in [111]. Given the complex index of refraction of the materials as well as the resonator thickness and gap to substrate, the algorithm given in [111] solves Maxwell's equations to determine the percentage of laser energy absorbed in and reflected from the resonator. The gap to substrate is varied to account for deflection of the device, giving absorption curves similar to that seen in Figure 1.1. For the 201 nm thick silicon device with 400 nm un-deflected gap to substrate, we estimate $\alpha \simeq 0.035, \gamma \simeq 0.011, z_o \simeq 0.18$.

The mechanical parameters are fit as follows: first the devices under test are driven at low amplitude in vacuum and their resonance curve is measured. The quality factor (Q) is determined by fitting the resonance curve to a Lorentzian, and is estimated to be between 10,000 and 14,000 for different beams. Given the low damping, the natural frequency (ω_0) is taken to be equal to the measured angular resonant frequency (ω_r) which is used to non-dimensionalize the equations. The spring stiffness temperature coefficient ($\frac{1}{T_{Buckle}}$) is determined by taking a Taylor series expansion of the frequency-compression relation given in [131], using linear thermoelasticity to convert between temperature above ambient and compression. The cubic stiffness (β) is estimated using an FEM analysis

[6]Note that in this section γ is related to the absorption contrast, *not* the imperfection level.

in which a normal load of $0-10\ \mu N$ is applied at the center of a clamped-clamped beam. The load-displacement curve is least squares fit to $F = kz + \beta z^3$ using the appropriate non-dimensionalization.

The thermal parameters are also fit using the FEM analysis. The beam and a large volume of the surrounding substrate are modeled in 3D. The temperature is assumed to be zero at the outer boundary and a Heaviside unit flux is applied at the center of the beam. The inverse lumped thermal mass[7] (H) is related to the slope of the temperature at time $t = 0$ ($\dot{T}|_{t=0} = H$) and the cooling rate due to conduction (B) is related to the steady state average temperature ($\lim_{t\to\infty} T(t) = \frac{H}{B}$).

The imperfection level, D, is taken to be the normalized centerline deflection per unit temperature rise. See Table 2.2 for a full list of material properties used in parameter estimation and Table 4.3 for estimated model parameters for the 15 μm beam subject to 55 MPa pre-stress.

Finally, we examine the nature of solutions to equations (4.2,4.3,4.4) to identify the laser power at which self-oscillation is first seen (P_{Hopf}) and at which self-oscillation ceases when reducing power (P_{SNBC}). Equilibrium and periodic solutions are calculated using numerical continuation with AUTO2000 [24, 23]. Numerical continuation allows us to efficiently determine whether self-oscillation is possible in the model for a given laser power. Using AUTO, we track changes in the equilibrium solution as the laser power, P, is varied, monitoring for a Hopf bifurcation. Then we restart the continuation at the Hopf bifurcation, tracking the periodic solution that emerges. As an example, continuation results are depicted in Figure 4.4 using the parameters listed in Table 4.3.

[7] Note that the lumped thermal mass H is not related to the applied heat flux H_0.

Interferometric transduction depends on the feedback between heating and displacement, yet with no direct thermal-mechanical coupling term, $D = 0$, as laser power (P) increases, the displacement is zero until the beam thermally buckles at $T = T_{buckle}$. Direct thermal-mechanical coupling due to deformation of the beam at its supports couples heating and displacement at all temperatures making pre-buckling feedback oscillations possible. As an example calculation, for the 15 μm beams the reduction in the laser power when $D \neq 0$ at Hopf bifurcation (P_{Hopf}) is from P_{Hopf} = 19.4 mW to P_{Hopf} = 1.12 mW.

Parameter	Value	Parameter	Value
Q	10,900	ω_r	4.975 [MHz]
H	5,570 [$\frac{K}{W}$]	B	0.112
α	0.035	γ	0.011
β	6.72	T_{buckle}	28 [K]
D	2.32 $\times 10^{-4}$ [$\frac{1}{K}$]	P	Continuation Parameter

Table 4.2: Parameters for 15 μm beam given in non-dimensional units.

We have used continuation to calculate P_{Hopf} and P_{SNBC} for the 7,10,15 and 20 μm long beams: the results are presented in Table 4.3. Predicted threshold powers for self-oscillation are consistent with those measured in similar sized beams [111], paddles [113], disks [145], and the predictions of Langdon and Dowe [67]. Experimental results from the actual devices are presented in Section 3.1. Self-Oscillation was not seen in any of the devices modeled here up to the maximum obtainable laser power on sample of $\simeq$ 2 mW. Optical profilometry results available after completion of this study showed a large initial deformation, which shifted the location of the beam centerline within the interference field, altering the thermo-mechanical feedback from that predicted here. This greater than predicted imperfection level is believed to be due to vertical gradients in the pre-stress.

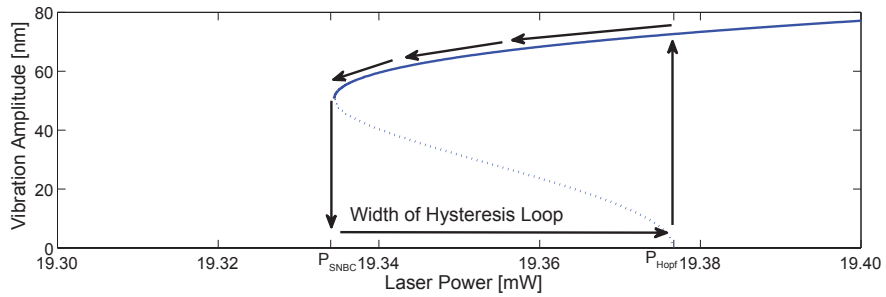

(a) No opto-thermal forcing, i.e. $D = 0$ in equation (4.2)

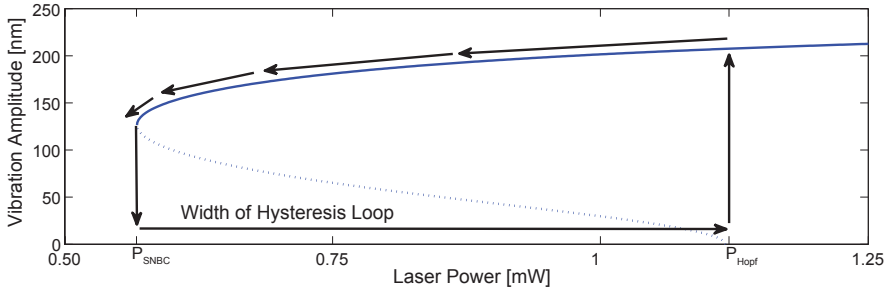

(b) With opto-thermal forcing, i.e. $D \neq 0$ in equation (4.2)

Figure 4.4: Continuation of periodic solutions. Incident laser power (P) is plotted along the x-axis and the amplitude of oscillation is plotted along the y-axis. P_{SNBC} is the lower threshold of self oscillation, and P_{Hopf} is the point at which the steady state solution becomes unstable giving rise to self-oscillation. Note the hysteresis loop. In addition to reducing P_{Hopf}, direct thermal-mechanical coupling reduces P_{SNBC} and thus increases the width of our hysteresis loop.

In order to illustrate the sensitivity of this analysis to the pre-stress values, the thermal mechanical coupling coefficient is re-calculated, and continuation performed assuming 35 MPa of pre-stress. For this pre-stress value, all beams are pre-buckled. Note the sensitivity of (P_{Hopf}) to the pre-stress value, particularly in the neighborhood of the buckling length. Parameters used are listed in Tables 4.5 and 4.4 for beams subject to 35 MPa and 55 MPa compressive pre-stress respectively. Note that out-of-plane displacement due to compres-

sive stress was not taken into account when calculating optical parameters. In addition, lumped thermal parameters (H, B) were calculated based on the temperature at midline rather than the average temperature. As a result the listed values of H are high by a factor of $\sim 2\times$.

	No DT, σ_{res} =55 MPa		With DT, σ_{res} =55 MPa		With DT, σ_{res} =35 MPa	
Length	$P_{Hopf}[mW]$	$P_{SNBC}[mW]$	$P_{Hopf}[mW]$	$P_{SNBC}[mW]$	$P_{Hopf}[mW]$	$P_{SNBC}[mW]$
7μm	482	467	64.7	19.1	76	22
10μm	239	233	18.2	4.46	26	5.8
15μm	19.4	19.3	1.12	0.568	7.0	2.0
20μm	N/A	N/A	0.0798	N/A	0.29	0.22

Table 4.3: Model predictions of power at which self oscillation is first seen (P_{Hopf}) and lowest power for which self oscillation is possible (P_{SNBC}). For 55 MPa of pre-stress, the 20 μm beams are already buckled. For post-buckled beams, the Hopf bifurcation in the model is seen to be supercritical and there is no hysteresis. For 35 MPa pre-stress, all of the beams are pre-buckled. As a result their thermal-mechanical coupling coefficients (D) are lower and threshold power for self-oscillation (P_{Hopf}) higher.

Model Parameters

Length [μm]	7	10	15	20
Q	10300	13800	10900	12400
T_{buckle} $[K]$	427	211	27.7	-48.3
D $[K^{-1}]$	6.94×10^{-6}	1.37×10^{-5}	2.32×10^{-4}	2.84×10^{-3}
β	4.09	4.65	6.72	15.5
H $[\frac{K}{W}]$	2670	4410	5570	6780
B	0.0931	0.152	0.112	0.112
γ	0.011	0.011	0.011	0.011
α	0.035	0.035	0.035	0.035
z_0	0.18	0.18	0.18	0.18

Table 4.4: Estimated parameters used in continuation and integration of model equations with 55 MPa of compressive pre-stress. The 20 μm beams are buckled leading to a negative T_{buckle}.

Model Parameters

Length [μm]	7	10	15	20
Q	10300	13800	10900	12400
T_{buckle} $[K]$	489	272	89.3	13.2
D $[K^{-1}]$	5.66×10^{-6}	9.37×10^{-6}	3.08×10^{-5}	6.82×10^{-4}
β	4.09	4.65	6.72	15.5
H $[\frac{K}{W}]$	2670	4410	5570	6780
B	0.0931	0.152	0.112	0.112
γ	0.011	0.011	0.011	0.011
α	0.035	0.035	0.035	0.035
z_0	0.18	0.18	0.18	0.18

Table 4.5: Estimated parameters used in continuation and integration of model equations with 35 MPa of compressive pre-stress. All beams are pre-buckled.

4.1.4 Conclusion

When illuminated with a CW laser, MEMS resonators have been shown to go into self-oscillation for sufficiently high laser power. Such interferometric transduction is driven by the coupling of heating to displacement and provides a means to achieve vibration in MEMS sensors without the need for externally modulated drive signals or extra fabrication steps which reduce the mechanical quality factor. We have shown that the threshold laser power needed for self-oscillation (P_{Hopf}) depends intimately on the static deflection due to steady state heating, and calculated that deflection for doubly-supported beams of various lengths. Unlike cantilevered beams, doubly-supported beams are seen to deflect away from the substrate when heated due to compressive stress across the length of the device. We have interpreted the thermal-mechanical coupling as the slope of a imperfection buckling load curve, and shown that the power needed for self oscillation decreases for increasing coupling. Thus, the amount of pre-stress provides a control parameter in designing low-power devices. Barely post-buckled beams should have the lowest threshold power for

self-oscillation, though that power (and the operating frequency) are sensitive to changes in pre-stress near the buckling load.

4.2 Continuation of Model Equations

In the following sections continuation and direct integration results are presented and discussed for large amplitude motion. Results indicate that multiple stable limit cycles are possible in interferometrically transduced devices, which are periodically spaced in amplitude due to periodicity in the interference field. Since small displacement is not assumed, approximate analytic methods (Lindstedt's method, harmonic balance) give poor predictions, thus no analytic results are presented. Lastly, conclusions are drawn about the properties of corresponding physical devices in which multiple stable limit cycles would be possible. Material from this section is drawn from work discussed at the ASME International Design Engineering Technical Conference 2011 [9] which is currently under review for journal publication.

4.2.1 Theoretical Model

The equations that follow are applicable to any interferometrically-driven MEMS device with a temperature dependent stiffness and direct thermal-mechanical coupling, but here a clamped-clamped beam is modeled to illustrate the phenomenon. A similar model has been used to describe the motion of optically excited disks, dome oscillators, and beams [106, 7, 92, 91]. See [106] for a more detailed discussion. These same equations are discussed in Section 4.1

in more detail, and are merely re-stated here[8]. Assuming first mode vibration gives us the following mechanical model:

$$z'' + \frac{z'}{Q} + \left(1 - \frac{1}{T_{Buckle}}T\right)z + \beta z^3 = DT, \tag{4.5}$$

where z is the centerline displacement scaled by the laser wavelength ($z = \frac{x}{\lambda}$), time is rescaled by the linear resonant frequency ($\tau = t\omega_0$), and primes denote derivatives with respect to non-dimensional time τ. The device quality factor is Q, cubic stiffness β, thermo-mechanical coupling D, and T_{Buckle} determines how sharply the linear frequency changes with temperature.

The resonator is assumed to heat up due to laser absorption and cool down due to Newton's law of cooling, giving the following equation governing the average temperature in the beam (T)

$$T' = -BT + HP_{absorbed}(z), \tag{4.6}$$

where B is the cooling rate due to conduction, H is the inverse of the lumped thermal mass, and $P_{absorbed}(z)$ is the energy absorbed due to interferometric heating. The absorption function $P_{absorbed}(z)$ depends on the properties of the interferometer for a given deflection (z), is proportional to the applied laser power, is periodic with period $\frac{\lambda}{2}$ in x (or $\frac{1}{2}$ in z), and is approximated by

$$P_{absorbed}(z) = P[\alpha + \gamma \sin^2(2\pi(z - z_o))] \tag{4.7}$$

[8]Parameters from [9] have been re-labeled in order for notation to be consistent that used in Section 4.1

with fitting parameters α, γ, and z_o[9]. Equations (4.5, 4.6, 4.7) form a system of two coupled ordinary differential equations and one algebraic equation to model the first mode of vibration of a MEMS resonator. In the next section, the parameter estimation process is described and parameters are established for a 201 nm thick, 10 μm long clamped-clamped silicon beam with 400 nm gap to substrate, subjected to 55 MPa of pre-compression, with measured resonant frequency of $2\pi\omega_r$ =9.96 MHz.

Optical parameters (α,γ,z_0) are fit using a physics based model of reflection, transmission and absorption in thin films given in [111] and expanded on in Section 4.4. Thermal parameters (H,B) are fit using an FEM thermal model of the beam and surrounding substrate. Structural parameters (Q,T_{buckle} and β) are fit using a mixture of experimental results, analytic results, and FEM modeling. See [106] or Section 4.1 for a detailed description of the parameter estimation techniques. Parameters used here are for the 10μm long beam subjected to 55 MPa of compressive pre-stress and are listed in Table 4.4.

4.2.2 Continuation Results

The continuation tool AUTO 2000 [24, 23], is used to examine the structure of solutions to equations (4.5,4.6,4.7). This software package is commonly used in the bifurcation analysis of differential equations and algebraic systems. Using AUTO 2000 we track the change in the equilibrium and periodic solutions as the laser power is varied.

We begin with $P = 0$ which has known equilibrium solution ($z = 0, z' = 0, T =$

[9] Again, here γ is related to the absorption contrast, not the imperfection level.

0). This equilibrium solution is continued in P, monitoring the eigenvalues of the Jacobian of the linearized system for Hopf-bifurcations. For low laser power, there is a unique stable equilibrium solution with small centerline displacement. As the laser power is increased to $P \simeq 18mW$, this equilibrium solution loses stability in a Hopf bifurcation leading to self-oscillation. As the power is increased further, the equilibrium solution branch begins to lift up from $z_{eq} = 0$ and a second branch of equilibrium solutions is born at $P \simeq 168mW$ in a fold of equilibrium points. An equilibrium point along this branch is computed numerically using a root finding method and then is used as a starting point for continuation of the branch. See Figure 4.5 for a plot of the equilibrium branches along with Hopf-bifurcation points at which limit cycles are born. This behavior in the position and number of equilibria is caused by imperfection buckling in the model (see Section 4.1). Hopf bifurcations along the branches of equilibria alter the usual buckling stability result - that the unbuckled state is unstable and the buckled states stable. Two directions of stability are lost or gained in a Hopf bifurcation and one direction in a fold.

Next, we turn our attention to the limit cycle oscillations born in Hopf bifurcations. The continuation is restarted at each Hopf bifurcation and the emerging limit cycle is followed, allowing the power, P, and frequency of oscillation, $2\pi\omega$, to vary. Following the limit cycle branch born in the first Hopf bifurcation, we see a series of folds of limit cycles in which stable and unstable limit cycles coalesce or divide (see Figure 4.6), in addition to regions of period doubling which are discussed later. To display equilibrium points and limit cycles on the same bifurcation diagram, the maximum displacement attained during one cycle (z_{max}) is used as the dependent variable for limit cycles. This measure includes the amplitude plus a small mean value roughly equal to the displace-

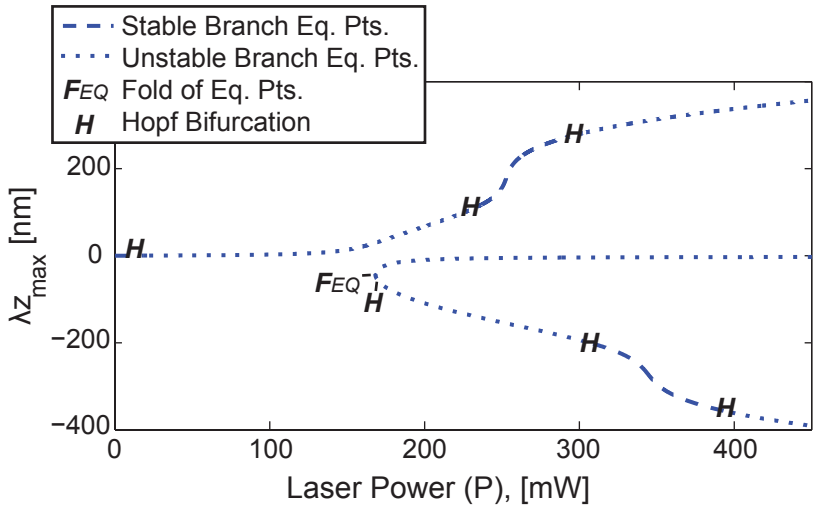

Figure 4.5: AUTO generated bifurcation diagram of the system, showing location and stability of equilibrium solutions as a function of laser power (P). Limit cycle branches emerging from Hopf bifurcations (*H*) are shown in Figure 4.12.

ment of the equilibrium solution from which the motion was born. Note the limiting value of LCO amplitude as laser power is increased. Amplitude saturation was initially observed by [46], and is supported by our data presented in Section 3.1.

For a given laser power, the amplitudes of stable limit cycles differ by roughly the period of the interferometer, $\frac{\lambda}{2} \sim 316\ nm$. Thus the multiplicity of stable limit cycles is due to periodicity in the interference field, and each higher amplitude stable limit cycle shows motion between similar points in the phase of the interference field, but includes more or less periods. For example, if the lowest amplitude limit cycle shows motion between one peak of absorption in the interference field and the first subsequent peak in the interference field, then the second lowest amplitude limit cycle shows motion between one peak of the absorption in the interference field, and the second subsequent peak (see Figure

1.1). See Figure 4.7 for a phase portrait of the equilibrium solution and limit cycles for $P = 135mW$ when a stable and unstable limit cycle have just been born in a fold of limit cycles.

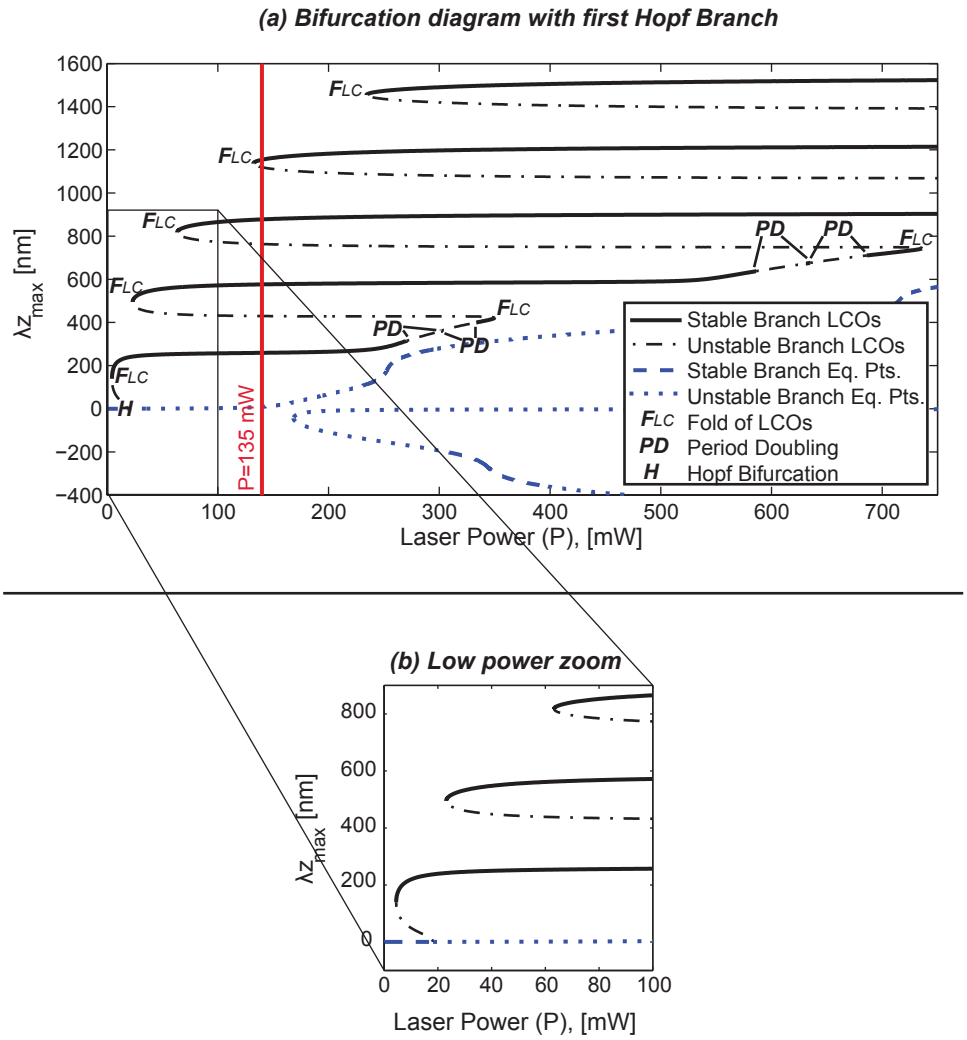

Figure 4.6: AUTO generated bifurcation diagram (a) showing the two branches of equilibrium solutions as well as the branch of limit cycles born in the first Hopf bifurcation. Included is a zoom view (b) of the bifurcation diagram for low laser power. The intersection of a vertical line with the equilibrium or limit cycle branches indicates the solutions possible at a given laser power. See figure 4.7 for a phase portrait of the limit cycles and equilibrium solutions for $P = 135mW$.

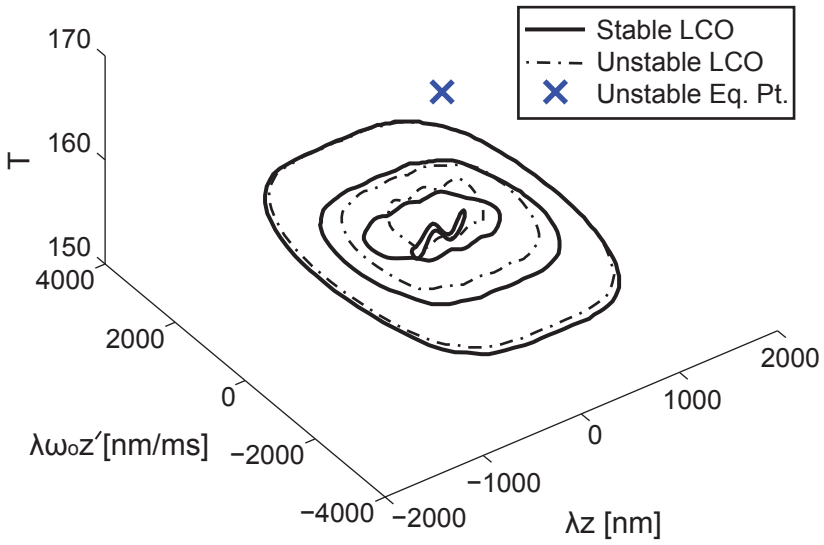

Figure 4.7: Plot of the equilibrium and periodic solutions for $P = 135mW$. Note that large amplitude stable and unstable motions have just been born in a fold of limit cycles. See figure 4.6 for the accompanying bifurcation diagram.

The period of oscillation along the first Hopf branch is depicted in Figure 4.8. Note that the limit cycle initially has non-dimensional period of $\sim 2\pi$. As the laser power is increased two competing factors influence the period of oscillation. The temperature dependence of the linear stiffness causes the period to increase with temperature and so the period increases with laser power for a given stable limit cycle. At the same time, the cubic stiffness due to membrane stresses causes the period to decrease with increasing amplitude of oscillation. Thus at a fixed laser power, high amplitude limit cycles have lower periods. The interplay of these tuning mechanisms in post-buckled beams was explored experimentally in Section 3.2, while analysis here is for pre-buckled beams.

It is numerically observed that as damping is increased, high amplitude limit cycles become unattainable at low laser power. Increased damping flattens out

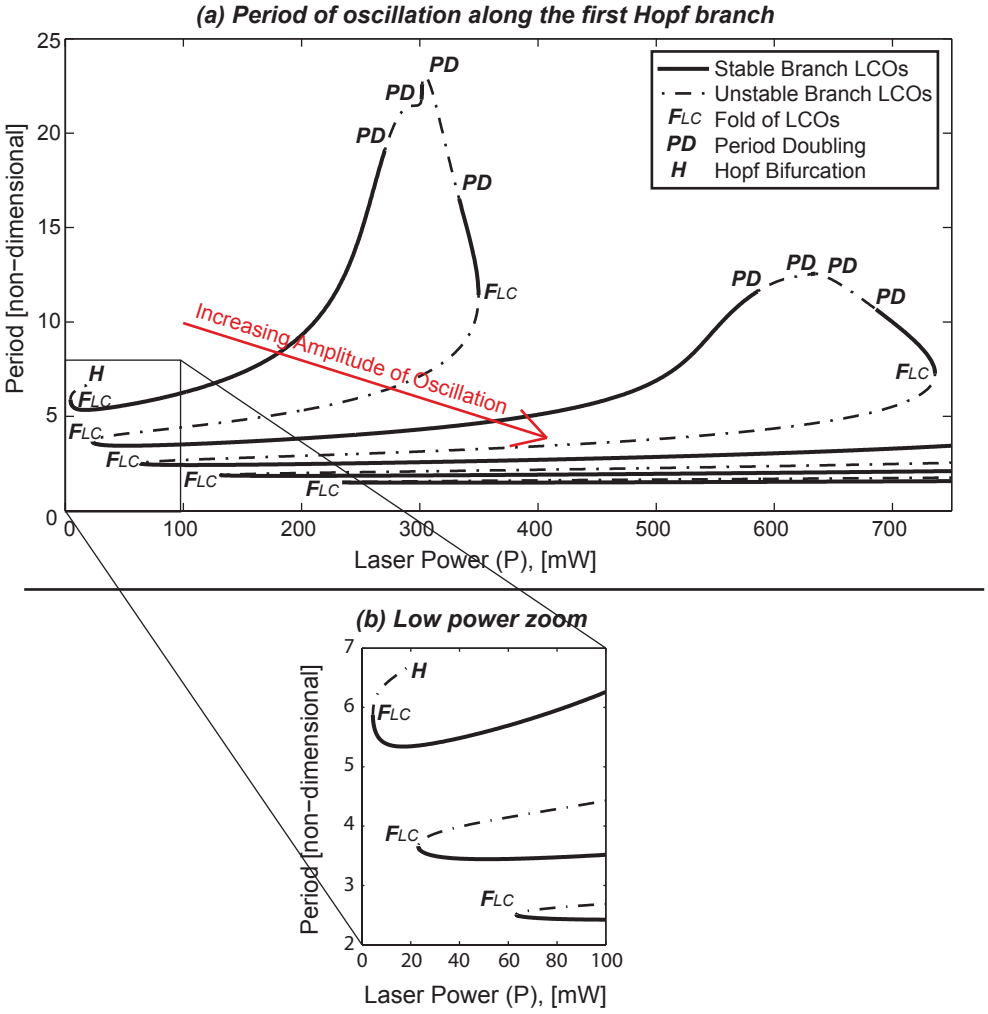

Figure 4.8: The period of oscillation (a) along the branch of limit cycles born in the first Hopf. Included is a zoom view (b) of the period for low laser power. Note that the limit cycle is born with non-dimensional period $\sim 2\pi$ at the point marked H.

these curves in the first Hopf branch, reducing the number of stable limit cycles accessible at a given laser power (see Figure 4.9). For sufficiently high damping, the Hopf bifurcation becomes supercritical and a unique stable limit cycle exists in this branch for $P > P_{Hopf}$.

Although the results presented here are for 10 μm beams subject to 55 MPa of pre-compression, we have estimated parameters for beams of length 7,10,15, and 20 μm with varying amounts of pre-compression. Continuation of the model equations using these parameters shows that multiplicity of stable limit cycles in the first Hopf branch is a *robust feature of the model* for lightly damped pre-buckled beams, and occurs at laser powers which are realizable in experimental setups. In the following section, we describe the rest of the bifurcation structure for 10 μm beams, including bifurcations occurring at laser powers above the thermal buckling power. We also describe the jump phenomenon associated with destruction of stable limit cycles.

4.2.3 Complete Bifurcation Diagram

In this section we build up the complete picture of the bifurcation structure, by describing each additional bifurcation separately. To begin with, we return to the regions of period doubling along the first Hopf branch (see Figure 4.6). Here we see that as we increase the laser power, our original limit cycle goes unstable and a new stable limit cycle is born with twice the period of the original. Continuing this new limit cycle, there is a cascade of period doubling where this process continues with increasing frequency as we increase the laser power (see Figure 4.10). Direct numerical integration is used to verify the existence of these

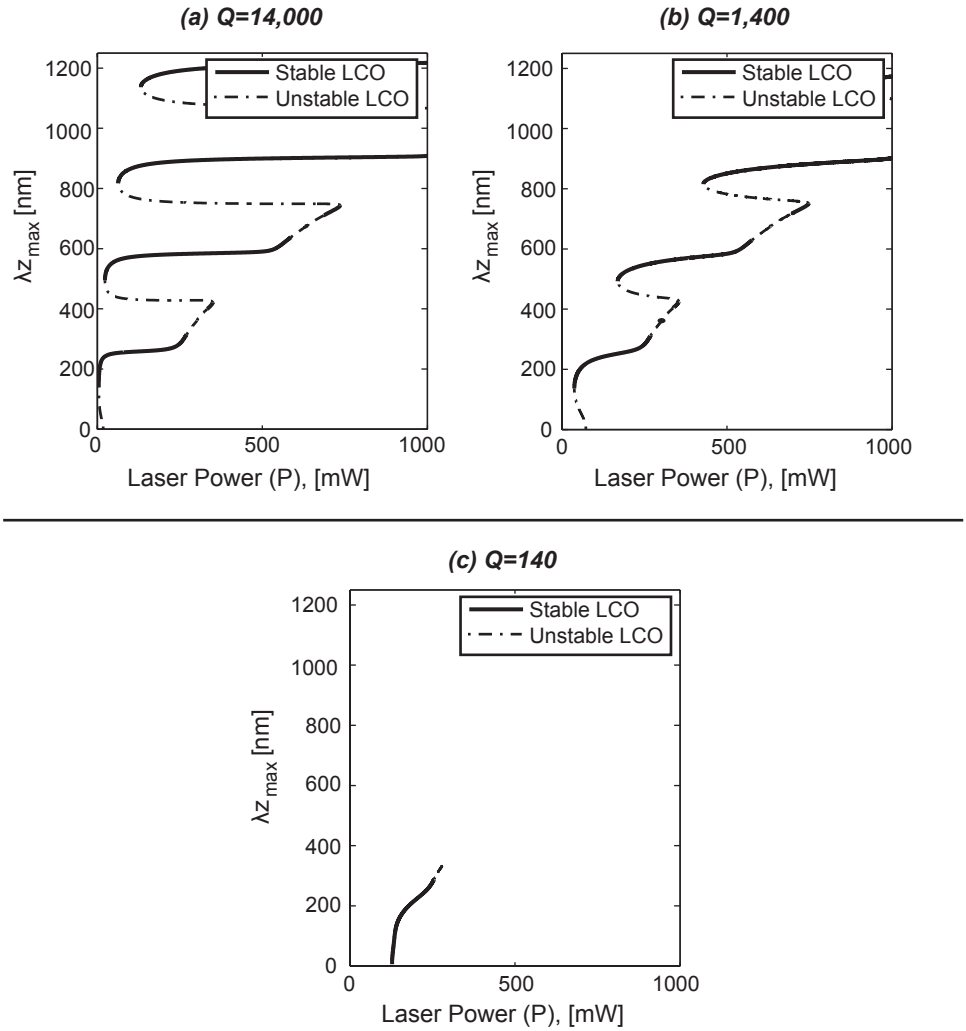

Figure 4.9: Effect of damping: AUTO generated bifurcation diagram showing the branch of limit cycles born in the first Hopf bifurcation. The same model parameters are used as before, except the quality factor (Q) is reduced by a factor of 10 between each subplot. Note that the increased damping increases the laser power at which self-oscillation becomes possible and also flattens out the curves in the first Hopf branch. For $Q = 140$, the Hopf bifurcation has become supercritical and there is a unique stable limit cycle, which quickly leads to period doubling and dies in a homoclinic bifurcation (*not shown*).

special solutions. Period doubling is a well-known route to chaos, and chaos has been experimentally observed in the forced vibration of buckled beams [81], thus it is likely that chaos exists in the model in this range of laser powers.

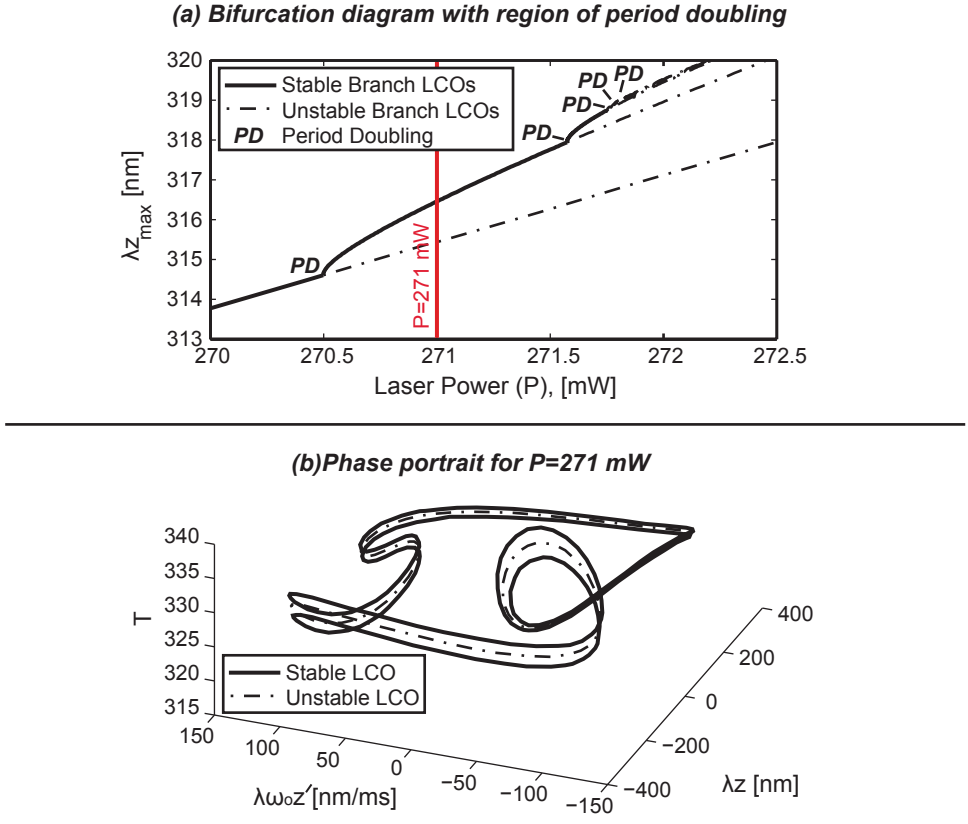

Figure 4.10: Bifurcation diagram (a) of a cascade of period doubling for high laser power. Only the first five period doubling bifurcations are tracked numerically, though more are believed to exist. A phase portrait (b) just after the first period doubling bifurcation shows that the original limit cycle (one-loop) has gone unstable, and a new stable cycle is born which traverses two loops before closing.

For all of the parameter sets studied, there were additional Hopf bifurcations from the equilibrium branches for laser powers above the buckling power. Following the limit cycle emerging from the second Hopf bifurcation, we see a fold of limit cycles, and then the cycle coalesces with an unstable equilibrium point

in a homoclinic bifurcation. See Figure 4.11 for a bifurcation diagram of this region and a phase portrait just before the homoclinic bifurcation. Accounting for the limit cycles born in the other Hopf bifurcations gives a complete bifurcation diagram shown in Figure 4.12.

4.2.4 Jump Phenomenon

Finally, direct integration is used to illustrate the hysteresis possible in the system. Although the bifurcation structure illustrates the types of stable and unstable behaviors possible in the model, it does not tell us which behaviors would be seen experimentally as we change the laser power - a question dealing with the basins of attraction for different stable behaviors. For each Hopf bifurcation or fold of limit cycles where an equilibrium solution loses stability or stable motion disappears, respectively, we use a point along that motion as an initial condition, increase or decrease the laser power slightly beyond the bifurcation and integrate until the trajectory settles onto a new steady behavior. See Figure 4.13 for a plot of the jump phenomenon. As we quasi-statically increase the laser power from zero beyond the first Hopf bifurcation at $P \sim 18mW$, the beam begins to oscillate in the lowest amplitude limit cycle. Once oscillating, we have to decrease the power below the lowest fold of limit cycles at $P \sim 4.5mW$ in order to jump back onto the stable equilibrium solution. At each fold of limit cycles along the first Hopf branch, jumps occur up to the next highest amplitude stable limit cycle when increasing the laser power, or down to the next lowest amplitude stable limit cycle when decreasing the laser power. Entering the region of period doubling, stable n-cycles give rise to stable 2n-cycles and so there are no jumps. However, it is unclear if stable periodic motions exist over the entire

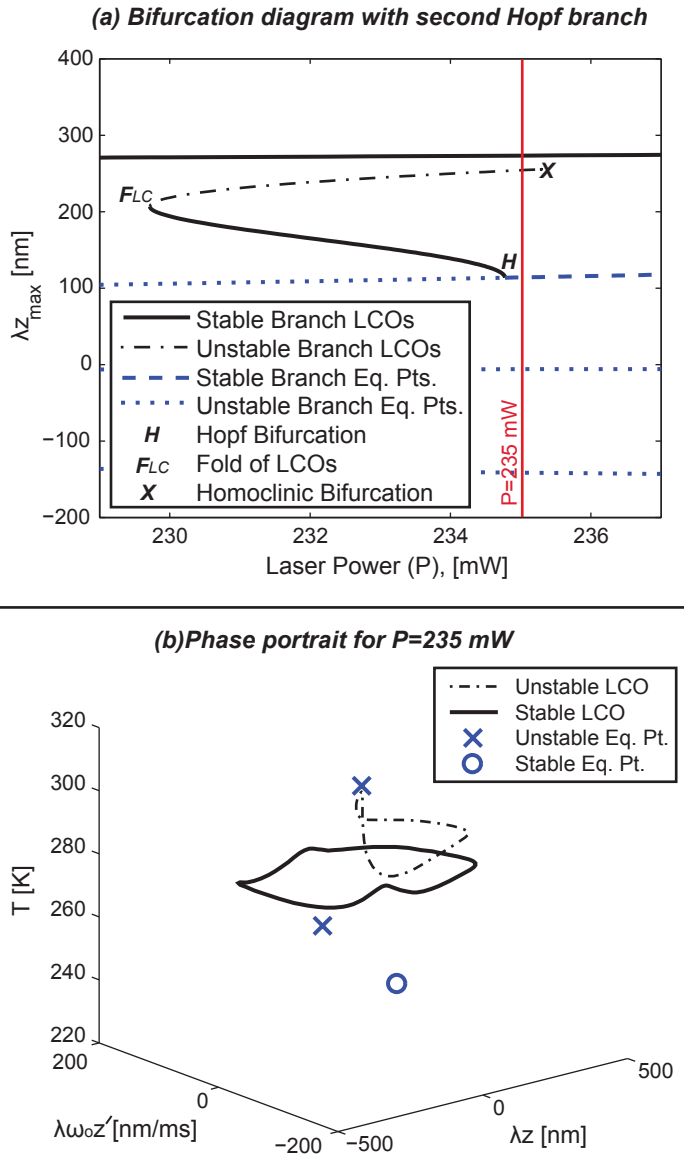

Figure 4.11: Portion of the bifurcation diagram (a) in the region of the second Hopf point (after the thermal buckling point as seen in figure 4.12), and phase portrait (b) of the system just before the homoclinic bifurcation. The unstable limit cycle has developed a kink as it approaches the stable and unstable manifold of an equilibrium point. Included is the neighboring limit cycle from the first Hopf branch, though higher amplitude limit cycles are omitted.

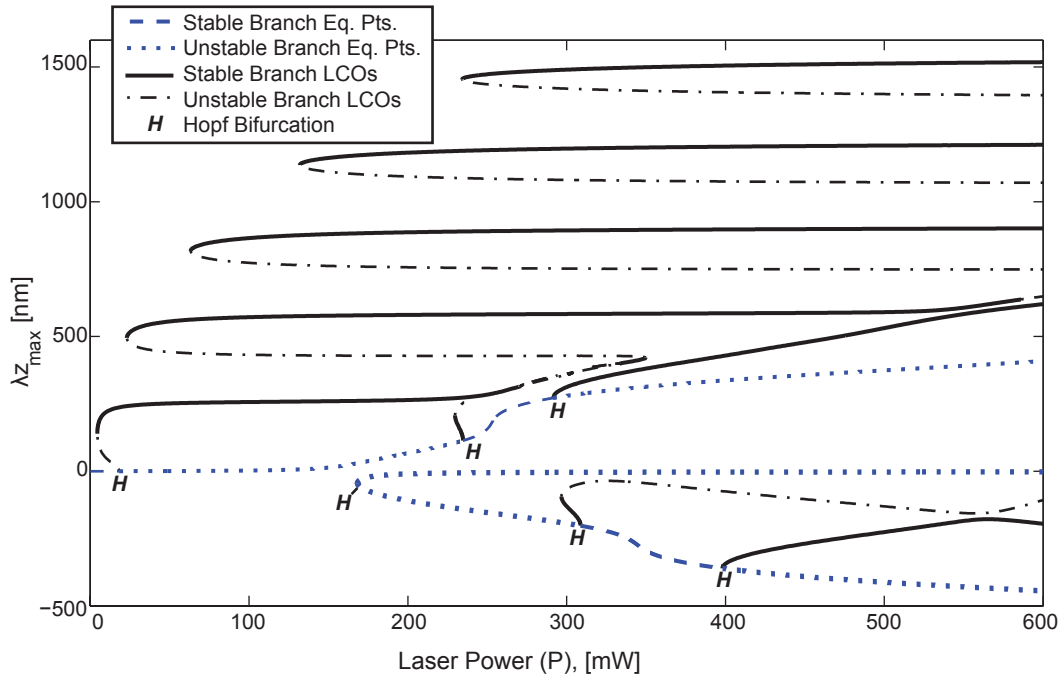

Figure 4.12: Complete bifurcation diagram of the system. Note that the limit cycle oscillation born in a Hopf bifurcation in the elbow of the fold of equilibria dies so quickly in a homoclinic bifurcation that it its not visible on the bifurcation diagram at this scale.

interval or if there are regions of chaos.

4.2.5 Comparison with Previous Work

Previous work [7, 144] on modeling limit cycle oscillations in optically driven MEMS resonators has assumed small displacement, and expanded the optical equation (4.7) in a power series losing the periodicity in the process, but making the equations amenable to approximate analytic methods. This small displacement approximation predicts a single Hopf bifurcation, either subcritical

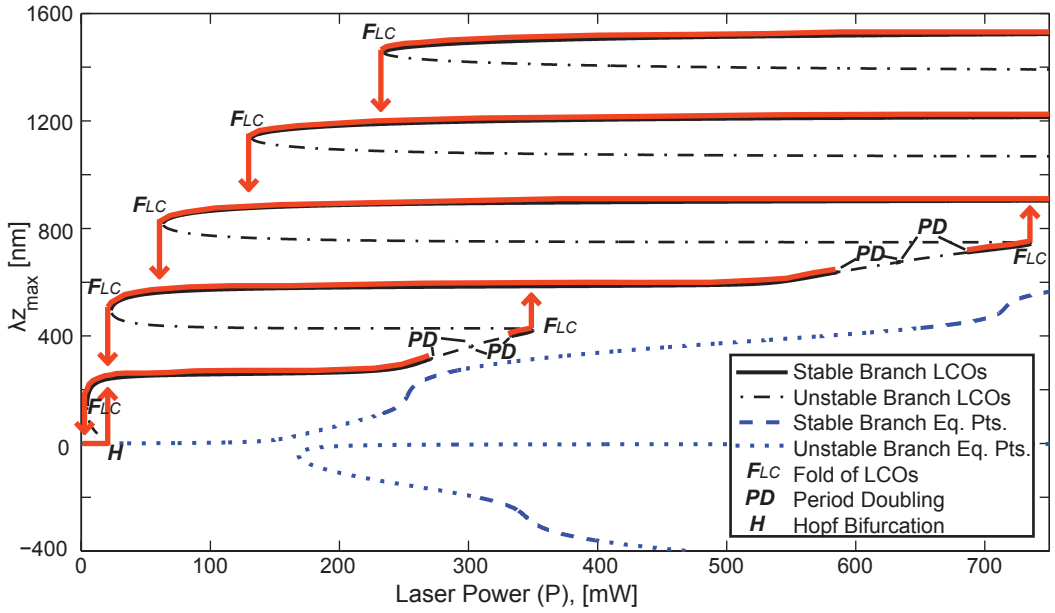

Figure 4.13: Jump phenomenon in the first Hopf branch.

or supercritical, leading to a stable/unstable pair or single stable limit cycle respectively. Thus series expanding the optical equation suppresses secondary Hopf bifurcations and folds of limit cycles. For comparison, a bifurcation diagram for equations (4.5,4.6) is given in Figure (4.14), where the parameters for a 10 μm long beam from Table 4.4 are used but equation (4.7) has been Taylor expanded in z, keeping the first 2 terms.

4.2.6 Conclusion

A MEMS device illuminated within an interference field will self-oscillate due to feedback between absorption and displacement. Models in the form of coupled differential equations have been used to describe the dynamics of such vibrations [7, 145, 93, 106, 91, 92, 19, 144], and analyzed under the assumption of small displacement. In this work, we show that if we relax that assump-

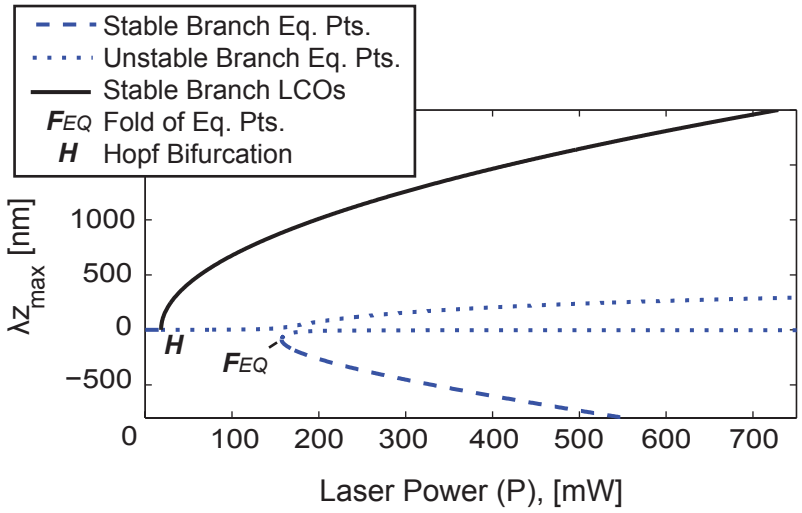

Figure 4.14: Bifurcation diagram of the model equations assuming small displacement, where equation (4.7) has been expanded in a first order Taylor series. Buckling has not been suppressed, but secondary Hopf bifurcations and folds of limit cycles have been lost. The approximate equations give a similar value for P_{Hopf} but not of the limit cycle amplitude or equilibrium solution.

tion then multiple stable limit cycles are possible due to the periodicity of the interference field. The frequency of these oscillations is shown to depend sensitively on the laser power with competition between linear and non-linear tuning mechanisms as seen in Section 3.2. Other complex motions exist for high laser power.

The analysis presented is applicable to any interferometrically driven MEMS device with a temperature dependent stiffness and static deflection, though clamped-clamped beams were chosen to analyze here due to their relatively simple structure. Physical devices exhibiting multiple stable limit cycles due to the phenomenon presented are expected to share some common characteristics:

(a) The need for a temperature dependent stiffness and deflection suggests

the use of devices that can generate tension across the device, i.e. clamped-clamped beams or domes rather than cantilevers or disks.

(b) Damping has been shown to decrease the number of stable limit cycles accessible at a given power, thus devices would need to be high-Q.

(c) Stable limit cycles are seen to be separated in amplitude by $\Delta x \simeq \frac{\lambda}{2}$. To permit n-stable limit cycles, devices must have a initial gap-to-substrate of greater than $\frac{\lambda}{2}$ in order to prevent contact with the substrate. Excitation with a HeNe laser would require a gap of $\gtrsim 1\ \mu m$ in order to see three limit cycles.

Although rigorously derived and analyzed, the results are expected only to present a qualitative picture of the dynamics of interferometrically driven MEMS devices, i.e. that multiple stable periodic motions are to be expected in large clamped-clamped beams and domes in low damping environments. Note that these motions are seen for low laser powers (below the buckling temperature). Above the buckling temperature, the frequency-compression relationship changes, and the model may lose validity. A description of the bifurcation structure in this region of high laser power ($P > 168\ mW$ for the parameters used here) is presented and represents simply an analysis of the model, which suggests the possibility of period doubling, chaos, and secondary Hopf bifurcations in the physical system. Multiple limit cycles were not observed in our devices possibly due to the fact that LCO was not observed in pre-buckled beams, or possibly due to our limited gap-to-substrate.

4.3 First Principles Model

Motivated by the need to understand the contributors to low power self-resonant devices at the level of device design, in this paper we sacrifice accuracy for ease of use and present an (almost) parameter free model of interferometrically driven self-resonant MEMS. Perturbation analysis is used to predict the threshold power for self-oscillation, and predictions compared with the results of numerical continuation. Scalings of threshold power with device geometry and pre-stress are discussed.

4.3.1 Mathematical Model

Our analysis models doubly-supported MEMS beams illuminated with a laser focused to a spot at the beam's midline (see Figure 4.15). To begin with, we use beam theory to model the mechanical behavior of the resonator. Our model is adapted from an equation for the vibration of a beam including membrane stiffness. Only the details are sketched here, and the reader is referred to the original paper for further details [29]. Letting x be the position along the beam and $y(x)$ be the lateral deflection at point x, standard beam theory gives

$$EIy'''' + m\ddot{y} + \zeta\dot{y} = 0, \tag{4.8}$$

where m is the mass per unit length, ζ is the viscous damping coefficient, EI is the flexural rigidity, primes denote spatial derivatives, and overdots denote time derivatives. As noted in Section 4.1, such a model neglects in-plane tension which is the main driver of displacement due to heating in doubly-supported

beams. Thus, we extend the model to account for in-plane forces due to deflection, heating and residual tension. Using linear thermo-elasticity and writing the axial extension due to deflection to first order, the force of tension, F, is

$$F = \sigma A - \frac{EA}{L}\int_0^L \alpha_e U(x)dx + \frac{EA}{2L}\int_0^L (y'(x))^2 dx, \tag{4.9}$$

where A is the cross-sectional area of the beam, L is the length, α_e is the coefficient of thermal expansion, and $U(x)$ is the temperature above ambient. The sign convention used is that positive loads are tensile and negative loads are compressive. The first term, σA, is the residual tension from device fabrication, the second is due to heating/cooling of the beam, and the last is the due to deflection. The equation on the displacement field including the effect of tension, and assuming clamped-clamped boundary conditions is:

$$\begin{aligned} M[y,U] &= EIy'''' + \left[-\sigma A + \frac{EA}{L}\int_0^L \alpha_e U(x)dx - \frac{EA}{2L}\int_0^L (y'(x))^2 dx\right] y'' + \zeta\,\dot{y} + m\ddot{y} = 0, \\ & y(0) = y(L) = 0, \qquad y'(0) = y'(L) = 0. \end{aligned} \tag{4.10}$$

Fourier's law is used to model the temperature field. It was shown in Section 4.1 that beam deformation was caused by in-plane thermal expansion, thus we model the temperature in the beam using a $1D$ thermal model. Let $\dot{q}(x)$ be the heat generated per unit volume. Assuming the temperature above ambient is zero at the ends, we get

$$H[y,U] = \dot{U} - \alpha_c U'' - \frac{1}{\rho c}\dot{q}(x) = 0; \quad U(0) = U(L) = 0. \tag{4.11}$$

where α_c is the thermal diffusivity, ρ is the mass density, and c is the specific heat capacity.

The heating $\dot{q}(x)$ depends on the total laser power P, spatial distribution of power, and on the fraction, $f(x)$, of power absorbed at a given distance along the beam. Due to the Fabry-Pérot interferometer between the beam and substrate, $f(x)$ depends on x through the displacement field $y(x)$. Using the optical properties of the films involved, and their thicknesses, $f(y(x))$ can be solved for numerically [111]. We found in Section 4.2 that the power needed to obtain LCO depends on this function only in the neighborhood of the fixed point, and so we use a Taylor series approximation about the un-deflected state [10]. Assuming that the laser power is focused to a spot at the beam's centerline we get

$$\dot{q}(x) = \frac{P}{A}\Big[\alpha_o + \gamma y(x)\Big]\delta\Big(x - \frac{L}{2}\Big), \tag{4.12}$$

where P is the total laser power, α_o is the zero-deflection absorption, γ is the absorption contrast of the Fabry-Pérot interferometer, and the delta-function, δ, is our spatial power distribution. See Figure 4.15 for a diagram of the system. Note that our thermal boundary conditions (4.11) assume that the substrate acts as an infinite heat sink. While not entirely accurate, this is a necessary simplification. For silicon-on-insulator (SOI) devices, the contrast in thermal conductivity between the silicon device layer and underlying oxide confines heat to the device layer, resulting in an elevated temperature at the anchor [10, 54]. Thus we expect SOI devices to have higher temperatures than the model predicts for the same applied flux (see Section 4.1).

[10] In this context "un-deflected" includes the initial deformation due to stress and imperfections. Unless the beam midline is located near a point of high curvature, the additional $O(1)$ nm static deflection due to laser heating causes a negligible change to the absorption contrast.

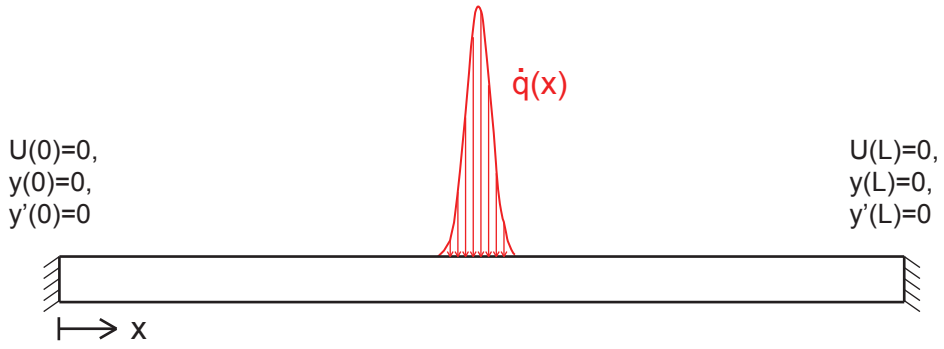

Figure 4.15: Diagram of modeled beam illustrating boundary conditions. The heating function $\dot{q}(x)$ is drawn with finite width for illustration purposes only, and in the model is described by a delta-function and thus has no width.

Finally, our equations are projected onto a set of test functions using the Galerkin method, and a set of coupled, non-linear ODEs obtained. For our test functions we select a time-dependent unit normal weight function multiplied by a space dependent shape function:

$$\tilde{y}(x,t) = \frac{a(t)}{2}\Big(1 - \cos\Big(\frac{2\pi x}{L}\Big)\Big), \qquad \tilde{U}(x,t) = b(t)\sin\Big(\frac{\pi x}{L}\Big). \tag{4.13}$$

Note that our test functions satisfy the boundary conditions (4.10) and (4.11) regardless of the time dependent weight functions. Requiring that our error in approximation be orthogonal to the test functions gives 2 ODEs governing the weight functions

$$\int_0^L \tilde{y}(x,t)M[\tilde{y}(x,t),\tilde{U}(x,t)]dx = 0 \quad \rightarrow \quad \ddot{a} + c_0\dot{a} + a(c_1 - c_3 b) + c_2 a^3 = 0, \tag{4.14}$$

$$\int_0^L \tilde{U}(x,t)H[\tilde{y}(x,t),\tilde{U}(x,t)]dx = 0 \quad \rightarrow \quad \dot{b} = -c_4 b + \frac{2P}{mcL}\Big[\alpha_o + \gamma a\Big], \tag{4.15}$$

with the constants c_i defined as follows

$$\begin{aligned} c_0 &= \frac{\zeta}{m} \\ c_1 &= \left[\frac{4\pi^2\sigma A}{3mL^2} + \frac{16\pi^4 EI}{3mL^4}\right] \\ c_2 &= \left[\frac{\pi^4 AE}{3mL^4}\right] \\ c_3 &= \left[\frac{8\pi\alpha_e AE}{3mL^2}\right] \\ c_4 &= \left[\frac{\pi^2\alpha_c}{L^2}\right]. \end{aligned} \tag{4.16}$$

Our thermal equation (4.15) is a simple first order thermal equation coupled to the mechanical equation (4.14) through the $\frac{2P}{mcL}\Big[\alpha_o + \gamma a\Big]$ term. The mechanical equation is in the form of a damped Duffing oscillator coupled to the thermal equation through the $c_3 ab$ term. Note that all of the constants, c_i, are strictly positive, except for *(possibly)* the linear spring stiffness c_1. If we neglect the damping and non-linear terms in (4.14) then we get the equation for a simple harmonic oscillator with spring stiffness c_1 that depends on residual stress σ. As we decrease σ, i.e. increase compression, the frequency $\sqrt{c_1}$ decreases as $\sqrt{\sigma - \sigma_B}$ until $\sigma = \sigma_B = \frac{-4\pi^2 EI}{AL^2}$ at which point the linear spring stiffness passes through zero as the equilibrium lifts up from the $a = 0$ axis. To determine the post-buckled linearized frequency we introduce a new variable to shift the equilibrium back to zero. This process is discussed in Section 4.3.3. Thus, our linearized mechanical equation(4.14) demonstrates the correct frequency relationship inherent in Euler buckling and correctly predicts the buckling load [131]. For a fixed level of pre-stress, thermal buckling is also possible and occurs at $P_B = \frac{mcLc_1c_4}{2\alpha_o c_3}$.

Note that $(a_{eq} = 0,\ b_{eq} = \frac{2P\alpha_o}{mcc_4L})$ is always an equilibrium solution to equations (4.14), (4.15) which thus exhibit perfect buckling. Thus, the displacement a_{eq}

will be independent of the laser power P until thermal buckling occurs. As a result, feedback oscillations are not possible for pre-buckled beams in this model. However, in the physical system, asymmetry of the support, initial shape imperfections, or fabrication defects break the symmetry and lead to imperfection buckling where there is a small non-zero deflection before the buckling load (see Section 4.1). The most common technique for dealing with these asymmetries analytically is to lump all contributors to asymmetry together into a net imperfection modeled as small amplitude pre-deformation of the beam in it's first buckling mode [34]. The beam's amplitude of imperfection is typically unknown in advance, and would become a fitting parameter in the system [34]. As such, rather than incorporate the effect of imperfections at the stage of PDEs, we choose to do so at the stage of ODEs, by adding a thermal-mechanical coupling term, $c_5 b$, to the mechanical equation which breaks the symmetry and gives a_{eq} a non-zero value pre-buckling. Drawbacks of this method are discussed in Appendix A.

Including this imperfection term, and re-writing (4.14), (4.15) in first order form with the change of variables $a \rightarrow z$; $\dot{a} \rightarrow v$; $b \rightarrow T$ we get our model equations

$$\begin{bmatrix} \dot{z} \\ \dot{v} \\ \dot{T} \end{bmatrix} = \begin{bmatrix} v \\ -c_0 v - c_1 z - c_2 z^3 + c_3 z T + c_5 T \\ -c_4 T + \frac{2P}{mcL}\Big(\alpha_o + \gamma z\Big) \end{bmatrix}, \tag{4.17}$$

where T is the centerline beam temperature above ambient, z is the centerline beam displacement, and v is the velocity of the centerline.

4.3.2 Bifurcation Analysis

Since the transition to self-oscillation has been shown to happen in a Hopf bifurcation [7], we analyze our equations (4.17) for the laser power, P_{Hopf}, which causes this bifurcation. In order for a Hopf bifurcation to occur, we need a pair of eigenvalues to cross from the left to right half of the complex plane, or vice-versa. Thus, we calculate the steady state deflection and temperature as a function of laser power, P, linearize the system about this equilibrium solution, and then check for a pair of pure imaginary eigenvalues in the linearized system.

Plugging in the equilibrium condition $\dot{z} = \dot{v} = \dot{T} = 0$ we get an algebraic equation for the location $[z_{eq}, v_{eq}, T_{eq}]$ of the equilibrium point. One equation is trivially $v_{eq} = 0$. We can find a closed form solution for $z_{eq}(P)$ and $T_{eq}(P)$ by solving the last equation for T_{eq} and plug into the second to get a cubic equation on z_{eq}. However, such a solution is unwieldy and produces formulas for P_{Hopf} which are impractical to evaluate. Once again, we choose to sacrifice accuracy for manageability by estimating the equilibrium condition using a perturbation series.

In the pre-buckling regime, the laser power is low and deformation is dominated by the imperfection level. We let $P = \epsilon P$, $z_{eq} = z_0 + \epsilon z_1 + \epsilon^2 z_2 + ...$ and collect powers in ϵ to get to lowest order:

$$\begin{aligned} z_{eq}^{pre}(P) &= \frac{2\alpha_o c_5}{c_1 c_4 mcL} P \\ T_{eq}^{pre}(P) &= \frac{2P}{c_4 mcL}\Big[\alpha_o + \gamma z_{eq}^{pre}\Big], \end{aligned} \tag{4.18}$$

In the post-buckling regime, the effect of the imperfection level on deflection is

insignificant, as deflection is governed by the linear and non-linear stiffness. We let $c_5 = \epsilon c_5,\ z_{eq} = z_0 + \epsilon z_1 + \epsilon^2 z_2 + ...$ to get:

$$\begin{aligned} z_{eq}^{post}(P) &= \frac{\sqrt{c_3^2 P^2 \gamma^2 - c_1 c_2 c^2 m^2 L^2 c_4^2 + 2\alpha_o c_2 c_3 c_4 mcLP} + c_3 \gamma P}{c_2 c_4 mcL} \\ T_{eq}^{post}(P) &= \frac{2P}{c_4 mcL}\Big[\alpha_o + \gamma z_{eq}^{post}\Big], \end{aligned} \tag{4.19}$$

Evaluating the Jacobian at the estimated equilibrium point, we get the following characteristic equation governing the eigenvalues, λ_i:

$$\lambda^3 + k_2\lambda^2 + k_1\lambda + k_0 = 0, \tag{4.20}$$

where k_i depend on P through $z_{eq}(P)$ and $T_{eq}(P)$. Letting $\lambda = \pm i\omega$ and equating the real and imaginary parts yields the following equation on P_{Hopf}

$$k_0(P_{Hopf}) = k_1(P_{Hopf}) \cdot k_2(P_{Hopf});\ k_0(P_{Hopf}) > 0. \tag{4.21}$$

In the pre-buckled regime we use (4.18) for the equilibrium solution $[z_{eq}(P), 0, T_{eq}(P)]$. The coefficients from the characteristic equation (4.20) are given below:

$$\begin{aligned} k_0^{pre}(P) &= -\frac{2c_5\gamma P}{mcL} - \frac{8\alpha_o c_3 c_5 \gamma P^2}{c_1 c_4 m^2 c^2 L^2} - \frac{2\alpha_o c_3 P}{mcL} + \frac{12 c_2 \alpha_o^2 c_5^2 P^2}{c_4 c_1^2 m^2 c^2 L^2} + c_1 c_4 \\ k_1^{pre}(P) &= -\frac{4\alpha_o c_3 c_5 \gamma P^2}{c_1 c_4^2 m^2 c^2 L^2} - \frac{2\alpha_o c_3 P}{c_4 mcL} + \frac{12 c_2 c_5^2 \alpha_o^2 P^2}{c_1^2 c_4^2 m^2 c^2 L^2} + c_0 c_4 + c_1 \\ k_2^{pre}(P) &= c_4 + c_0 \end{aligned} \tag{4.22}$$

When the coefficients (4.22) are plugged into (4.21) they give a quadratic on P, the correct solution to which is an estimate of P_{Hopf} in the pre-buckled regime. In order to determine which root is extraneous, we note the results of Section 4.1, namely that limit cycle oscillation is not possible in the pre-buckled regime without imperfections to couple heating to displacement. As the imperfection level approaches zero ($c_5 \to 0$), the power needed for self-oscillation should grow without bound ($P_{Hopf} \to \infty$). Thus we keep the root which comes in from infinity and is positive.

In the post-buckled regime we use (4.19) for the equilibrium solution and get the following coefficients:

$$\begin{aligned}
k_0^{post}(P) &= \frac{2c_3\gamma P\ \sqrt{c_3^2\gamma^2P^2 - c_1c_2c_4^2m^2c^2L^2 + 2\alpha_o c_2c_3c_4mcLP}}{c_2c_4mcL^2} \\
&+ \frac{2c_3^2\gamma^2P^2}{c_2c_4m^2c^2L^2} + P\frac{4\alpha_o c_3 - 2c_5\gamma}{mcL} - 2c_1c_4 \\
k_1^{post}(P) &= \frac{4c_3\gamma P\ \sqrt{c_3^2\gamma^2P^2 - c_1c_2c_4^2m^2c^2L^2 + 2\alpha_o c_2c_3c_4mcLP}}{c_2c_4^2m^2c^2L^2} \\
&+ \frac{4c_3^2\gamma^2P^2}{c_2c_4^2m^2c^2L^2} + \frac{4\alpha_o c_3P}{c_4mcL} + c_0c_4 - 2c_1 \\
k_2^{post}(P) &= c_4 + c_0
\end{aligned} \tag{4.23}$$

When (4.23) are plugged into (4.21) they give an implicit equation for P_{Hopf} in the post-buckled regime, which may be numerically evaluated using a root-finding method. In Section (4.3.4) these formula will be evaluated and the results compared with continuation results for physically relevant parameters.

4.3.3 Parameter Fitting

While our first-principles derivation of the governing equations skirts the need for time consuming FEA to fit model parameters, there are still two parameters which require analysis: the damping constant, c_0, and the thermal-mechanical coupling constant, c_5. In this section we present those analyses and give the values for the material and geometric properties used in calculating the other parameters.

We begin by discussing the damping constant, c_0. There are many sources of damping in MEMS, including viscous or squeeze-film damping, thermo-elastic damping, and clamping losses [139]. Rather than relating the damping term c_0 to these environment factors, we relate it to the measurable quality factor Q of the resonator. Imagine that the resonator is driven at small amplitude with the laser power low enough not to affect the device dynamics, i.e. $P \to 0$ and $T \to 0$, and a quality factor Q measured. In this situation, our mechanical equation (4.17) reduces to $\ddot{z} + c_0\dot{z} + c_1 z + c_2 z^3 = 0$. In the pre-buckled regime ($c_1 > 0$) the only equilibrium is $z_{eq} = 0$ and linearized frequency is simply $\sqrt{c_1}$. We get damping term $c_0 = \frac{\sqrt{c_1}}{Q}$ by comparison of the linearized equation to the simple harmonic oscillator, $\ddot{z} + \frac{\omega_o}{Q}\dot{z} + \omega_o^2 z = 0$. In the post-buckled regime ($c_1 < 0$), we have $z_{eq} = \sqrt{\frac{-c_1}{c_2}}$ and linearized frequency of $\sqrt{-2c_1}$ giving $c_0 = \frac{\sqrt{-2c_1}}{Q}$. Note that our calculation of the pre- and post-buckled frequency agrees quite well with those given in [11]. Having fit the damping constant, we then turn our attention to the imperfection level.

Given the way in which we've incorporated the imperfection amplitude, our thermal-mechanical coupling constant, c_5, can be related to the change in displacement per unit temperature rise. Doing a perturbation series approxima-

tion in T to our mechanical equation about the $z = 0$ equilibrium we get the following relationship for the equilibrium solution $z_{eq} = \frac{c_5}{c_1} T_{eq} + O(T^2)$. To fit c_5 we could in theory, heat the sample to a known temperature, measure the displacement and take the ratio, scaled by c_1. FEM data on the imperfection level of a $15\mu m$ beam is presented in [10], and experimental data for beams of length $30\mu m$ to $140\mu m$ in [34]. The imperfection amplitude scales as the length of the beam, thus $\frac{c_5}{c_1 L}$ is a constant. Using the data in [10] we get a change in displacement per unit temperature rise per unit length of $\frac{c_5}{c_1 L} = 5 \times 10^{-7} \frac{1}{K}$, similar to the $\frac{c_5}{c_1 L} = 1.58 \times 10^{-6} \frac{1}{K}$ from [34]. The former value is used in the calculations which follow. See Appendix A for a detailed discussion of this procedure, along with a comparison of the imperfection levels measured in terms of a pre-deformation from Section 2.2.3.

Material and geometric parameters used in subsequent numerical results are given below. Optical parameters (α_o,γ) are fit using a physics based model of reflection, transmission and absorption in thin films given in [111]. Note that the equilibrium value shifts with pre-stress or heating, particular for buckled beams. For buckled beams, if the buckling amplitude is a significant fraction of the period of the interference field, one would need to include the buckling amplitude when calculating the absorption function. The shift in equilibrium due to pre-stress in the non-buckled regime, or due to heating is negligible for devices studied here.

Parameter	Value	Parameter	Value
E	130×10^9 [Pa]	I	1.69×10^{-27} $[m^4]$
m	1.22×10^{-9} $[\frac{kg}{m}]$	A	5.03×10^{-13} $[m^2]$
α_e	2.5×10^{-6} $[\frac{1}{K}]$	α_c	9.87×10^{-5} $[\frac{m^2}{s}]$
α_o	0.043	γ	-9×10^4 $[\frac{1}{m}]$
Q	10,000	$\frac{c_5}{c_1 L}$	5×10^{-7} $[\frac{1}{K}]$
c	712 $[\frac{J}{kgK}]$	L	Continuation Parameter [m]
σ	Continuation Parameter [Pa]	P	Continuation Parameter [W]

4.3.4 Numerical Results

The continuation tool AUTO 2000 [23] is used to examine the nature of solutions to (4.17), in order to validate approximate results presented in Section 4.3.2. This software package is commonly used in bifurcation analysis of differential equations and algebraic systems. Using AUTO, we can calculate P_{Hopf} as a function of the beam's length and pre-stress level in order to verify the analytic estimate of $P_{Hopf}(L, \sigma)$ found using perturbation theory.

We treat L, σ, and P as our continuation parameters, and start with $L = 10\mu m$, $\sigma = 0$, $P = 0$ which has known equilibrium value $[z_{eq} = 0, v_{eq} = 0, T_{eq} = 0]$. We then continue this equilibrium solution in P, monitoring the eigenvalues of the Jacobian of the linearized system for Hopf bifurcations. Once we reach $P_{Hopf}(10, 0)$, we switch parameters, and continuing the Hopf point in L, and σ. In this way we can trace out the surface $P_{Hopf}(L, \sigma)$. Due to the singular nature of the buckling point, we cannot continue solutions across it. In order to trace out the post-buckled surface, we calculate an equilibrium solution in the buckled regime ($\sigma = 2\sigma_B$) using a root-finding routine, and repeat the process of finding $P_{Hopf}(10, 2\sigma_B)$ and continuing it in L and σ in that region. The stress required to produce buckling depends on beam length. In order to compare results for beams of different lengths, we scale the residual stress by the buckling

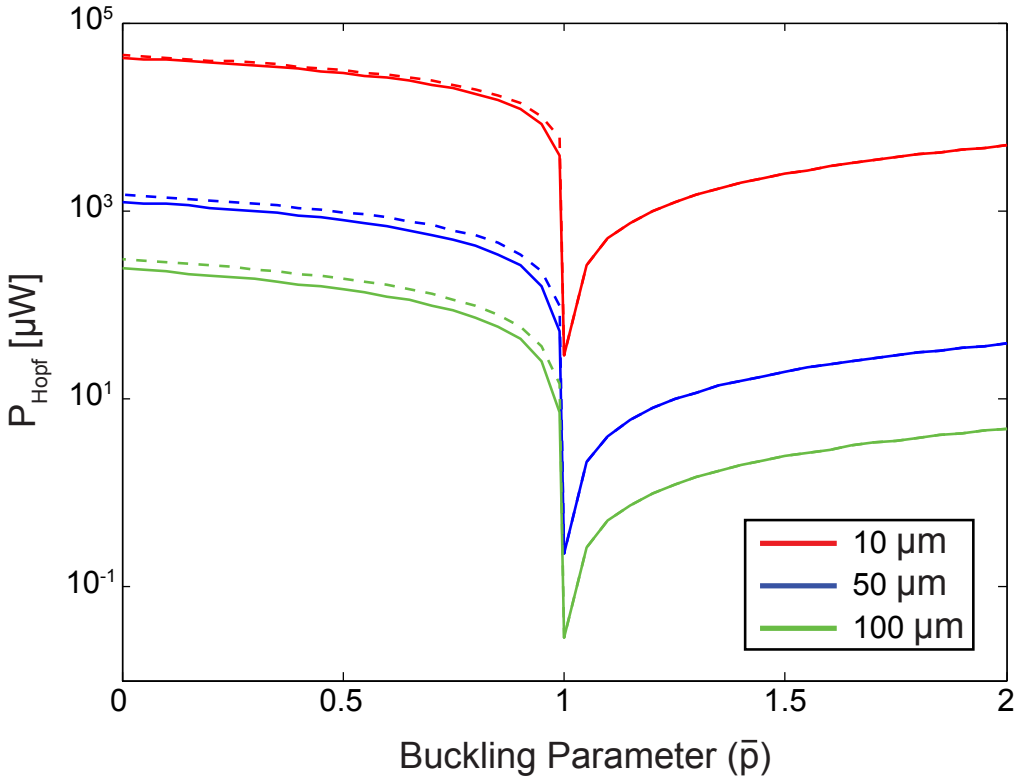

Figure 4.16: Threshold power for self-oscillation, P_{Hopf}, calculated using continuation theory (solid line) and approximated using perturbation theory (dotted line), plotted as a function of buckling parameter $\bar{p}$ for fixed length. Note that $\bar{p} = 1$ is the buckling load.

stress, plotting the buckling parameter $\bar{p} = \frac{\sigma}{\sigma_B}$ as our non-dimensional measure of stress with $\sigma_B = \frac{-4\pi^2 EI}{AL^2}$ for a clamped-clamped beam [131] (see also Section 4.3.2).

Note in Figure 4.16 that P_{Hopf} decreases with length for a fixed buckling parameter. For fixed length, P_{Hopf} is lowest at buckling, where it appears to go to zero. We believe this is because of the strength of coupling between heating and displacement in this region. As the level of pre-stress approaches the buckling load, the slope of the load curve becomes almost vertical at the (imperfect)

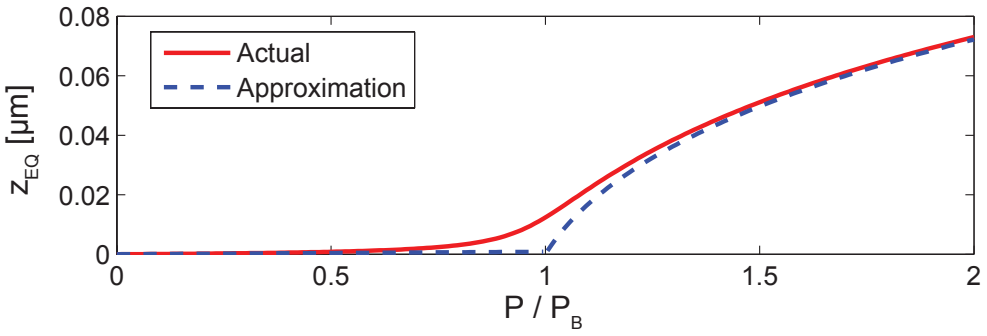

Figure 4.17: AUTO calculated and approximate equilibrium solutions as a function of laser power P. Data is for a $50\mu m$ beam with no initial pre-stress. Note that our approximations (4.18,4.19) lose accuracy near the thermal buckling load, and that the slope of the actual load curve approaches vertical there.

buckling point (see Figure 4.17). As a result, heating is most strongly coupled to displacement near buckling, giving strong thermo-mechanical feedback. In the post-buckled region, the slope of the load curve tapers off, leading to a decrease in coupling and increase in P_{Hopf}.

In order to verify our perturbation results, we compare the estimates of (4.22, 4.23) to the results of numerical continuation (see Figure 4.18). Note that our approximations of P_{Hopf} lose accuracy near the buckling load, and are worse in the pre-buckled regime where our equilibrium value approximations are worse. Higher order approximations of the equilibrium point give more accurate results, but yield unwieldy formulas for P_{Hopf}. Note that these results merely illustrate the loss in accuracy between direct analysis of model equations and perturbation solutions. They do not validate that the model PDEs accurately describe the system of interest, nor probe the error induced in the projection from PDEs to ODEs.

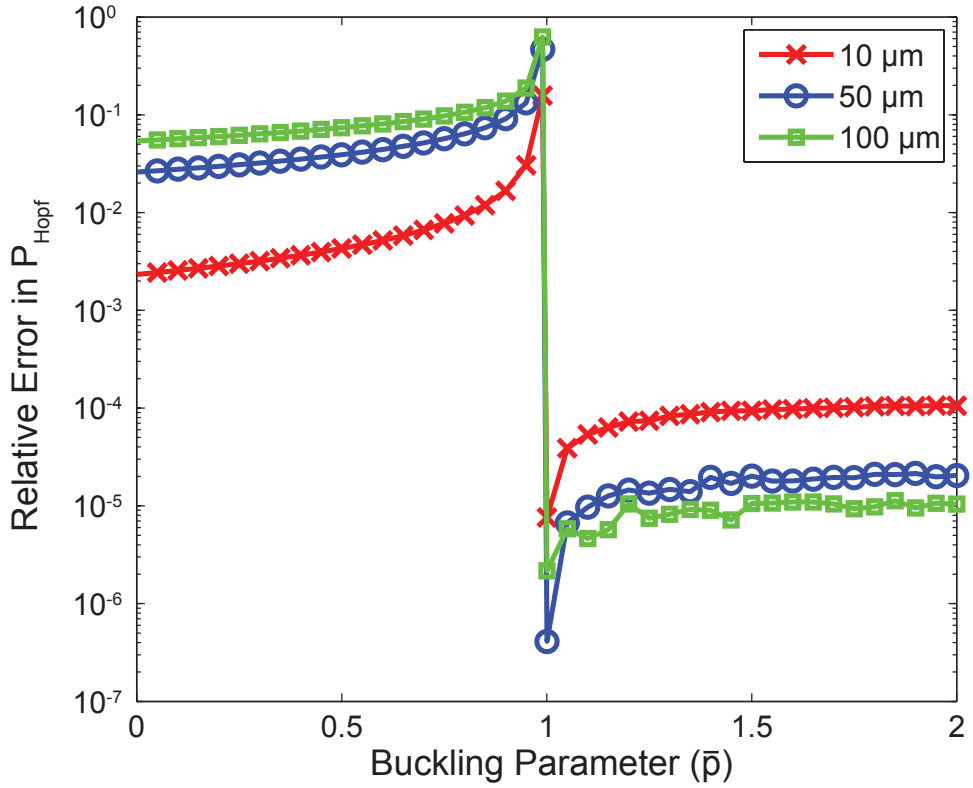

Figure 4.18: Relative error in perturbation approximation of P_{Hopf} as compared with actual result found using numerical continuation

While the threshold power for self-oscillation is predicted to decrease drastically near buckling, the frequency also goes to zero. In practical applications, low threshold powers of self-oscillation and high frequencies are both desirable. Thus, a good figure of merit for a self-resonant beam would be:

$$\text{F.O.M.} = \frac{\text{resonant frequency}}{\text{threshold power for self-oscillation}}$$

In Figure 4.19 we plot the relative figure of merit for the beams under consideration. Longer, just barely buckled beams have the highest figure of merit.

In the following section we compare model parameters calculated using the first principles model with those calculated in previous sections using FEM

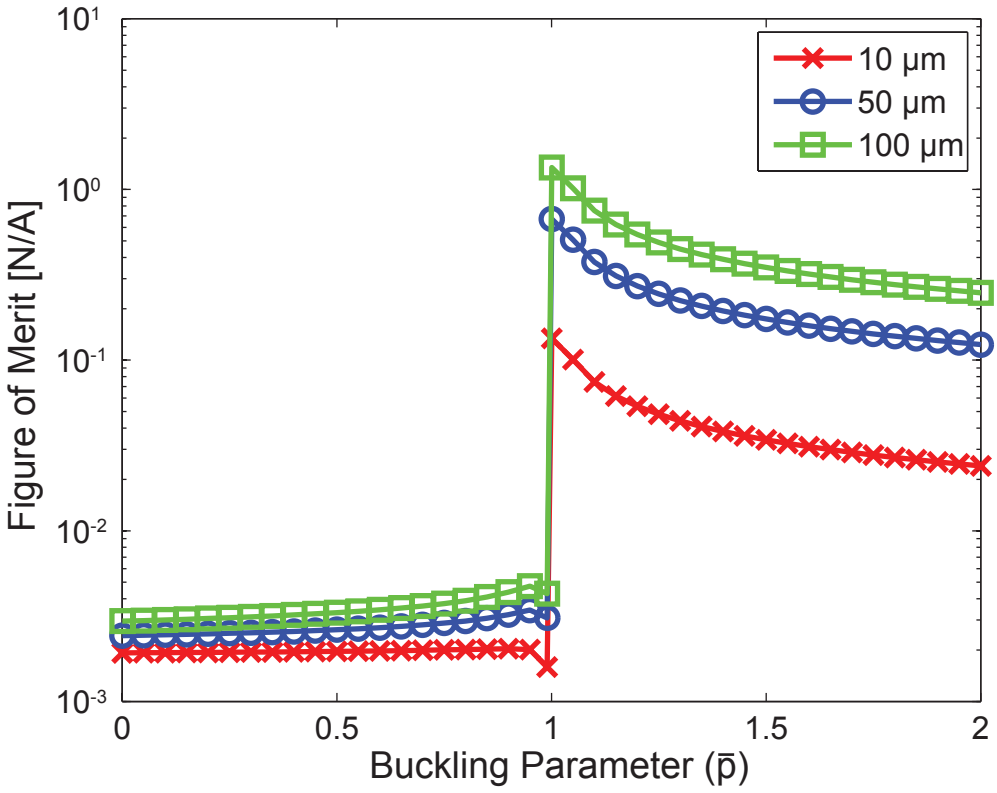

Figure 4.19: Figure of merit for self-resonant MEMS

modeling. In addition, we compare predicted values of P_{Hopf} with experimentally measured values.

4.3.5 Comparison with FEM and Experimental Data

We note that the mechanical equation (4.17) derived above is identical with those used in Sections 4.1 and 4.2 under the non-dimensionalization $z \to \frac{a}{\lambda}$; $\tau \to t\sqrt{c_1}$ and a re-labeling of parameters[11]. The same holds true for the thermal equation, except that the absorption curve is linearized. Under this transforma-

[11]The comparison for post-buckled beams is less straight forward.

tion, equations (4.17) become:

$$z'' + \frac{c_0}{\sqrt{c_1}} z' + \left(1 - \frac{c_3}{c_1} T\right) z + \frac{c_2 \lambda^2}{c_1} z^3 = \frac{c_5}{\lambda c_1} T \tag{4.24}$$

$$T' = \frac{-c_4}{\sqrt{c_1}} T + \frac{2}{\sqrt{c_1} mcL} P\,[\alpha + \gamma \lambda z] \tag{4.25}$$

where primes denote derivatives with respect to non-dimensional time. In order to verify the use of equations (4.16) to determine parameters in the equation of motion, we compare parameters given in section 4.1 and 4.2 found using FEA with their counterparts in equation of motion (4.24) calculated using equations (4.16). Results are presented in Table 4.6. Note that the *measured* resonant frequency is used to normalize equations with FEA calculated parameters and the *predicted* resonant frequency is used to normalize equations with parameters calculated from formulae. Significant error in the predicted frequency is present[12]. This error is propagated into calculation of the other (non-dimensionalized) parameters. Reproduction of the quality factor is exact by design. Nonetheless it is clear that there are disparities between FEA calculated and analytically predicted parameters. In particular, our analytic formulae over-estimate the strength of the stiffness non-linearity as compared to finite element analysis.

The measured laser power on sample needed to get limit cycle oscillation is compared with model predictions in Table 4.7. A ±2 nm uncertainty in the device thickness is included in order to illustrate the sensitivity of predicted power to calculations of the interference field. Uncertainty in the buckling amplitude was not included, though would shift the location within the interference field

[12]This is particularly true of longer beams. The estimated pre-stress level used in Sections 4.1 and 4.2 of 55 MPa was based off of dynamic analysis to deduce buckling and significantly over-estimates the stress-level estimated based on imperfection effects. This leads to a significant under-prediction of device frequency in devices whose length is near the buckling length.

Sec. 4.1	Q=10,900	T_{buckle}=28 K	β=6.72	D=2.32×10^{-4} [K^{-1}]
MODEL	$\frac{\sqrt{c_1}}{c_0}$=10,900	$\frac{c_1}{c_3}$=42.4 K	$\frac{c_2\lambda^2}{c_1}$=54	$\frac{c_5}{\lambda c_1}$=1.30×10^{-5} [K^{-1}]
Sec. 4.1 (*cont.*)	B=0.112	H=5,570 $\left[\frac{K}{W}\right]$	ω_r = 4.975 MHz	
MODEL (*cont.*)	$\frac{c_4}{\sqrt{c_1}}$=0.271	$\frac{2}{\sqrt{c_1}mcL}$=10,570 $\left[\frac{K}{W}\right]$	$\frac{\sqrt{c_0}}{2\pi}$= 2.11 MHz	
Sec. 4.2	Q=13,800	c_1=4.75 ×10^{-3} [K^{-1}]	β=4.65	c_2=1.37×10^{-5} [K^{-1}]
MODEL	$\frac{\sqrt{c_1}}{c_0}$=13,800	$\frac{c_3}{c_1}$=2.28 ×10^{-3} [K^{-1}]	$\frac{c_2\lambda^2}{c_1}$=11.5	$\frac{c_5}{\lambda c_1}$=8.75×10^{-6} [K^{-1}]
Sec. 4.2 (*cont.*)	B=0.152	H=4,410 $\left[\frac{K}{W}\right]$	ω_r = 9.96 MHz	
MODEL (*cont.*)	$\frac{c_4}{\sqrt{c_1}}$=0.125	$\frac{2}{\sqrt{c_1}mcL}$=3,290 $\left[\frac{K}{W}\right]$	$\frac{\sqrt{c_0}}{2\pi}$= 10.1 MHz	

Table 4.6: Comparison of parameters calculated using FEA in Sections 4.1 and 4.2 with those calculated using formulae in this section. Parameters from Section 4.1 are for a 201nm thick 15 μm long beam under 55 MPa stress, and those from Section 4.2 are for the 10 μm long beam.

by ± 10 nm and have considerable impact too, particularly on the 30 μm beams which sit next to a peak in the interference field. Predicted values of P_{Hopf} are generally consistent with measured data, though not entirely accurate.

Device, Chip I	P_{Hopf} [μW] *measured*	P_{Hopf} [μW] *predicted*
30 [μm]	93	68.6-N/A
Device, Chip II	P_{Hopf} [μW] *measured*	P_{Hopf} [μW] *predicted*
20 [μm]	N/A	552-3734
25 [μm]	N/A	N/A
30 [μm]	128	63.2-92.5
35 [μm]	32	19.8-33.0
40 [μm]	50	9.43-10.3

Table 4.7: Measured laser power on sample at onset of LCO (P_{Hopf}) compared with predictions using model of doubly-supported beams illuminated at their midline. The range given for the predicted values includes the ±2 nm uncertainty in device thickness from Section 3.1. Note that devices whose buckling amplitude places them need a peak/valley in the absorption spectrum are extremely sensitive to errors in measured thickness. In the case of the 30 μm device from Chip I, this variation spans the range from positive feedback to negative feedback.

4.3.6 Conclusion

A MEMS device, illuminated within an interference field may self-oscillate due to feedback between heating and absorption. Prior work on modeling the dynamics of such devices has used ad-hoc models and fit model parameters using a number of extensive FEA calculations. Here we use a first-principles method to derive the model equations without need for parameter estimation analyses. Quantitative accuracy is sacrificed for the sake of implicit or explicit equations for the threshold power for self-oscillation from which conclusions can be drawn about the qualitative device features which would lead to low power self-oscillation. Predicted values of P_{Hopf} are compared with the results of numerical continuation, and a parametric study is performed, varying device length and level of pre-stress. Results support the prediction in Section 4.1 that barely post-buckled beams should have the lowest threshold power for self-oscillation due to their strong thermal mechanical coupling. More specifically, results show that the value of P_{Hopf} is dominated by the slope of the load curve. In the post-buckled region, this slope is determined by the buckling parameter, whereas in the pre-buckled region, it is determined by the level of imperfection - a parameter which is difficult to control experimentally.

Equation parameters are compared to those calculated using finite element analysis, and disparities exist, particularly in the predicted magnitude of the stiffness nonlinearity. Finally, predicted values of P_{Hopf} are compared with measured values presented in Section 3.1, and show remarkable agreement in spite of disparities in parameter calculation. Ultimately, given the high level of imperfection in our devices, initial out-of-plane deformation is significant in comparison to the periodicity of the interference field and varies between beams

of different lengths. Thus, it is difficult from experimental data to separate geometry and stress-related factors from interferometric ones in their impact on P_{Hopf}.

4.4 Absorption in Thin Films

Limit cycle oscillations in optically driven MEMS have traditionally been modeled as occurring due to one of two effects: that modulation of average temperature across the device leads to a modulation of the spring stiffness and thus parametric amplification [63]; or that temperature gradients through the thickness of the device create a thermal moment which displaces it via the thermostat effect [67, 19, 45]. The efficacy of the latter depends on significant absorption induced thermal moments to drive deformation. Typically it is assumed that any heating occurs on the surface of the device, possibly due to metallic coatings used to increase absorption and create a bi-metallic effect. In uncoated beams there is no bi-metallic effect and if heating occurred throughout the thickness of the device, the resultant thermal moments would be insignificant. In order to evaluate the validity of the claim that thermal moments drive LCO in uncoated beams, we determine precisely where in the device absorption induced heating occurs by solving for the electric and magnetic fields and then calculating the resultant loss of field energy to Joule heating. The calculations are designed with uncoated resonators in mind, though are applicable to any thin film stack (where vacuum and/or air could be included as a "film").

Skin Depth

Before examining absorption in an optically-thin film stack, we first discuss

absorption of monochromatic light in a semi-infinite media, where there is no reflected wave to interfere with the transmitted wave. This well studied problem will allow us to define at what thickness a device is "optically-thin" and provide a test case to which later results should converge in the limit of thick films. In such a case, the electric field is seen to decay at a rate which depends on the imaginary part of the wave number. Assuming that the wave is traveling in the z^+ direction with the $z = 0$ plane defining the interface between the initial vacuum ($z < 0$) and the conducting medium ($z > 0$), we get the following expression for the electric field [57]:

$$\overrightarrow{E} = \tilde{\overrightarrow{E_0}} e^{i(\tilde{k}z - \omega t)}. \tag{4.26}$$

We adopt the convention that vectors are denoted with over-arrows and complex quantities are denoted with a tilde. Phase is accounted for by making the field amplitudes complex, thus the actual amplitude is the real part of the complex valued field. If we write the complex wave number[13] in terms of real and imaginary components, $\tilde{k} = k_{rn} + i\,k_{cn}$, then equation 4.26 may be further simplified to:

$$\overrightarrow{E} = \tilde{\overrightarrow{E_0}} e^{-k_{cn}} e^{i(k_{rn}z - \omega t)}. \tag{4.27}$$

Note in 4.27 that the electric field amplitude decays exponentially. The distance it takes to reduce the field amplitude by a factor of $\frac{1}{e}$ is called the "skin depth"[14]:

[13]Note the some authors write the complex index of refraction as $\tilde{n} = n + i\,\kappa$ while some write the complex wave number as $\tilde{k} = k + i\,\kappa$. In order to avoid ambiguity we use $\tilde{k} = k_{rn} + i\,k_{cn}$ and $\tilde{n} = n_{rn} + i\,n_{cn}$.

[14]"Penetration depth" may also be used to disambiguate between the distance that it takes to

$$d \equiv \frac{1}{k_{cn}}. \tag{4.28}$$

For silicon illuminated with a HeNe laser we have $\tilde{n} = 3.882 + 0.019\,i$ (see Section 2.2.1), giving $\tilde{k} = \frac{2\pi\tilde{n}}{\lambda_0} = 0.0385 + 0.000188\,i\left[\frac{1}{nm}\right]$. Thus silicon has a skin depth of $d = 5300$ nm at wavelength $\lambda_0 = 633$nm. For comparison, aluminum at the same wavelength has a complex wavenumber of $\tilde{n} = 1.374 + 7.620\,i$ giving it a skin depth of 13 nm.

Thus our devices with thickness $t \approx 200$ nm are optically thin, but a 13 nm surface coating of aluminum would confine absorption to the top surface. Next we turn our attention to a thin film stack where there is interference between reflected and transmitted waves.

Field Equations for a Thin Film Stack

Assume that monochromatic plane waves are normally incident on a stack of uniform films deposited on a semi-infinite substrate, with direction of propagation $\hat{z}$. Without loss of generality, we assume that the incoming and reflected electric-field is polarized in the $\hat{x}$ direction and the magnetic-field in the $\hat{y}$ direction (see Figure 4.20)[15]. We will also assume that the magnetic permeability, μ, of each layer is the same - this is approximately true of the materials under consideration.

Let $\tilde{k_0}$ be the complex wave number in the initial medium, $\tilde{k_1}$ .. $\tilde{k_n}$ be the complex wave number in each subsequent film layer, and $\tilde{k_s}$ be the complex wave

reduce the field intensity (square of field amplitude) by a factor of $\frac{1}{e}$.

[15] In our experimental setup the incoming light is circularly polarized, not linearly polarized, and in oblique incidence from conductors, reflected waves change their polarization. Thus these assumptions are simplifications to the problem.

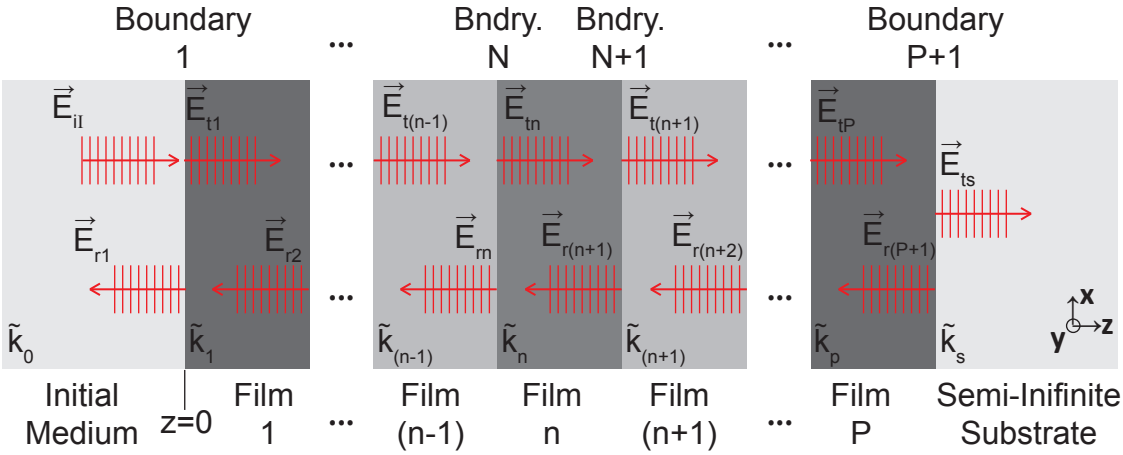

Figure 4.20: Diagram of Films and Fields

number in the semi-infinite substrate. The wave number may be related to the complex index of refraction, $\tilde{n}$, using $\tilde{k} = \frac{2\pi\tilde{n}}{\lambda_0}$. Here λ_0 the wavelength in vacuum. We use the convention that $\tilde{n} = n_{rn} + i\,n_{cn}$, thus plane waves have the following general form (pg. 297 in Ref [57])[16]:

$$\begin{aligned} \vec{E} &= \tilde{\vec{E}_0} e^{i(\tilde{\vec{k}}\cdot\vec{r}-\omega t)}, \\ \vec{H} &= \tilde{\vec{H}_0} e^{i(\tilde{\vec{k}}\cdot\vec{r}-\omega t)}, \end{aligned} \tag{4.29}$$

where $\tilde{\vec{k}}$ is a vector with magnitude equal to the complex wave number and pointing in the direction of propagation of the wave. $\tilde{\vec{E}_0}$ and $\tilde{\vec{H}_0}$ are the electric and magnetic field amplitude at $\vec{r} = \vec{0}$ respectively[17]. Our geometry and polarization assumptions give us the following formulae for transmitted waves

[16] A note of caution: Jackson uses Gaussian units, while Marion and Hecht use MKSA. As a result, some equations are different in Jackson. In addition, some use the convention that $\tilde{n} = n_{rn} - i\,n_{cn}$ and define the amplitude in terms of the real part of the complex conjugate of the wave.

[17] Here **H** actually refers to the "auxiliary field," which is related to the magnetic field, **B**, and magnetization, **M**. Many authors refer to **H** as the magnetic field since it has no other name.

(i.e. traveling in the z^+ direction) and reflected waves (i.e. traveling in the z^- direction) respectively :

$$\begin{aligned} \overrightarrow{E_t} &= \tilde{E}_t e^{i(\tilde{k}z-\omega t)}\hat{x}; \quad \overrightarrow{E_r} = \tilde{E}_r e^{i(-\tilde{k}z-\omega t)}\hat{x}, \\ \overrightarrow{H_t} &= \tilde{H}_t e^{i(\tilde{k}z-\omega t)}\hat{y}; \quad \overrightarrow{H_r} = \tilde{H}_r e^{i(-\tilde{k}z-\omega t)}\hat{y}. \end{aligned} \tag{4.30}$$

We can relate our magnetic field and electric field using [48]:

$$\overrightarrow{H} = \frac{\lambda_0}{2\pi}\sqrt{\frac{\epsilon_0}{\mu_0}}\tilde{\overrightarrow{k}} \times \overrightarrow{E}, \tag{4.31}$$

where ϵ_0 is permittivity of free space, and μ_0 is permeability of free space. Let the field at the N^{th} boundary between films be given as:

$$\overrightarrow{E} = \tilde{E}_N e^{-i\omega t}\hat{x}; \quad \overrightarrow{H} = \tilde{H}_N e^{-i\omega t}\hat{y}. \tag{4.32}$$

The incident wave, $\overrightarrow{E_{iI}}$, and transmitted wave in the semi-infinite substrate, $\overrightarrow{E_{ts}}$, may be written as:

$$\begin{aligned} \overrightarrow{E_{iI}} &= \tilde{E}_{iI} e^{i(\tilde{k}_0 z-\omega t)}\hat{x}, \\ \overrightarrow{E_{ts}} &= \tilde{E}_{ts} e^{i(\tilde{k}_s z-\omega t)}\hat{x}. \end{aligned} \tag{4.33}$$

The wave reflected *from* the $(n+1)^{th}$ interface, $\overrightarrow{E}_{r(n+1)}$, and wave transmitted *through* the n^{th} interface, $\overrightarrow{E_{ts}}$, may be written as:

$$\begin{aligned}
\overrightarrow{E}_{r(n+1)} &= \tilde{E}_{r(n+1)} e^{i(-\tilde{k}_n z - \omega t)} \hat{x}, \\
\overrightarrow{E_{tn}} &= \tilde{E}_{tn} e^{i(\tilde{k}_n z - \omega t)} \hat{x}.
\end{aligned} \tag{4.34}$$

Note that the reflected wave, $\overrightarrow{E}_{r(n+1)}$, travels in the opposite direction of the transmitted wave, $\overrightarrow{E_{tn}}$, giving the negative sign in front of the complex wave number in 4.34. Both travel through the same film layer, so the index of the complex wave number is the same.

Now we apply boundary conditions and solve for all of the reflected and transmitted waves in terms of the incident wave. Here, the appropriate boundary conditions are that the tangential components of $\overrightarrow{H}$ and $\overrightarrow{E}$ are continuous across the boundary (pg. 336 in Ref [57] or pg. 170 in Ref [77]). Applying this condition, we obtaining for boundary N:

$$\begin{aligned}
\tilde{E}_N &= \tilde{E}_{tN} e^{i\tilde{k}_n d_{(n-1)}} + \tilde{E}_{r(N+1)} e^{-i\tilde{k}_n d_{(n-1)}} \\
&= \tilde{E}_{t(N-1)} e^{i\tilde{k}_{(n-1)} d_{(n-1)}} + \tilde{E}_{rN} e^{-i\tilde{k}_{(n-1)} d_{(n-1)}} \\
\tilde{H}_N &= \left(\frac{\lambda_0}{2\pi}\sqrt{\frac{\epsilon_0}{\mu_0}}\right) \tilde{k}_n (\tilde{E}_{tN} e^{i\tilde{k}_n d_{(n-1)}} - \tilde{E}_{r(N+1)} e^{-i\tilde{k}_n d_{(n-1)}}) \\
&= \left(\frac{\lambda_0}{2\pi}\sqrt{\frac{\epsilon_0}{\mu_0}}\right) \tilde{k}_{(n-1)} (\tilde{E}_{t(N-1)} e^{i\tilde{k}_{(n-1)} d_{(n-1)}} - \tilde{E}_{rN} e^{-i\tilde{k}_{(n-1)} d_{(n-1)}}).
\end{aligned} \tag{4.35}$$

where d_n is the distance down to the $(N+1)^{th}$ interface. At the subsequent boundary, we have:

$$\tilde{E}_{N+1} = \tilde{E}_{tN} e^{i\tilde{k}_n d_n} + \tilde{E}_{r(N+1)} e^{-i\tilde{k}_n d_n}$$

$$
\begin{aligned}
&= \tilde{E}_{t(N+1)} e^{i\tilde{k}_{(n+1)} d_n} + \tilde{E}_{r(N+2)} e^{-i\tilde{k}_{(n+1)} d_n}, \\
\tilde{H}_{N+1} &= \left(\frac{\lambda_0}{2\pi}\sqrt{\frac{\epsilon_0}{\mu_0}}\right)\tilde{k}_n (\tilde{E}_{tN} e^{i\tilde{k}_n d_n} - \tilde{E}_{r(N+1)} e^{-i\tilde{k}_n d_n}) \\
&= \left(\frac{\lambda_0}{2\pi}\sqrt{\frac{\epsilon_0}{\mu_0}}\right)\tilde{k}_{(n+1)} (\tilde{E}_{t(N+1)} e^{i\tilde{k}_{(n+1)} d_n} - \tilde{E}_{r(N+2)} e^{-i\tilde{k}_{(n+1)} d_n}).
\end{aligned} \tag{4.36}
$$

Solving equations 4.36 for $\tilde{E_{tN}}$ and $\tilde{E}_{r(N+1)}$ in terms of the electric and magnetic field at the subsequent boundary, we get:

$$
\begin{aligned}
\tilde{E}_{tN} &= \frac{1}{2} e^{-i\tilde{k}_n d_n}\left[\tilde{E}_{N+1} + \frac{2\pi}{\lambda_0}\sqrt{\frac{\mu_0}{\epsilon_0}}\tilde{k}_n \tilde{H}_{N+1}\right], \\
\tilde{E}_{r(N+1)} &= \frac{1}{2} e^{i\tilde{k}_n d_n}\left[\tilde{E}_{N+1} - \frac{2\pi}{\lambda_0}\sqrt{\frac{\mu_0}{\epsilon_0}}\tilde{k}_n \tilde{H}_{N+1}\right].
\end{aligned} \tag{4.37}
$$

Plugging 4.37 into 4.35 and noting the definitions of the trigonometric functions in terms of complex exponentials we get the following equation relating the electric and magnetic fields on adjacent boundaries:

$$
\begin{bmatrix} \tilde{E}_N \\ \tilde{H}_N \end{bmatrix} = \begin{bmatrix} cos(\tilde{k}_n h_n) & \frac{-i2\pi\sqrt{\mu_0} sin(\tilde{k}_n h_n)}{\lambda_0 \sqrt{\epsilon_0}\tilde{k}_n} \\ \frac{-i\lambda_0\sqrt{\epsilon_0}\tilde{k}_n sin(\tilde{k}_n h_n)}{2\pi\sqrt{\mu_0}} & cos(\tilde{k}_n h_n) \end{bmatrix} \begin{bmatrix} \tilde{E}_{N+1} \\ \tilde{H}_{N+1} \end{bmatrix}, \tag{4.38}
$$

where we have defined $h_n \equiv d_n - d_{(n-1)}$ to be the thickness of film n. Note that the *transfer matrix* in equation 4.38 relating the fields at interface N to those at interface $N+1$ depends only on the properties of the Nth film. Thus we may write:

$$
\begin{bmatrix} \tilde{E}_N \\ \tilde{H}_N \end{bmatrix} = M_N \begin{bmatrix} \tilde{E}_{N+1} \\ \tilde{H}_{N+1} \end{bmatrix}, \tag{4.39}
$$

for each film layer, where M_N is the Nth transfer matrix. For a P-layer film stack, the *characteristic matrix*, M, relates the fields at first boundary (1) to the fields at the last boundary (P+1) and is just the product of all of the transfer matrices:

$$M = M_1 M_2 \cdots M_P = \begin{bmatrix} m_{11} & m_{12} \\ m_{21} & m_{22} \end{bmatrix}. \tag{4.40}$$

Now we will solve for the electric and magnetic field in each film and use it to calculate the drop in intensity through the film stack. To begin with we relate the fields at the first interface to the films at the last interface using the characteristic matrix:

$$\begin{bmatrix} \tilde{E}_1 \\ \tilde{H}_1 \end{bmatrix} = M \begin{bmatrix} \tilde{E}_{P+1} \\ \tilde{H}_{P+1} \end{bmatrix}. \tag{4.41}$$

Noting that the electric field at any point is the vector sum of a left and right traveling wave, writing the magnetic field in terms of the electric field using equation 4.31, and expanding out 4.41 in terms of the electric field amplitudes using equations 4.33 and 4.34, we get:

$$\begin{bmatrix} \tilde{E}_{iI} + \tilde{E}_{r1} \\ \frac{\lambda_0}{2\pi}\sqrt{\frac{\epsilon_0}{\mu_0}}\tilde{k}_0(\tilde{E}_{iI} - \tilde{E}_{r1}) \end{bmatrix} = \begin{bmatrix} m_{11} & m_{12} \\ m_{21} & m_{22} \end{bmatrix} \begin{bmatrix} \tilde{E}_{ts} e^{i\tilde{k}_s d_P} \\ \frac{\lambda_0}{2\pi}\sqrt{\frac{\epsilon_0}{\mu_0}}\tilde{k}_s \tilde{E}_{ts} e^{i\tilde{k}_s d_P} \end{bmatrix}. \tag{4.42}$$

Since the substrate is considered semi-infinite, there is no reflected wave in the substrate, while in the initial medium there is the incident wave, and wave reflected from the first boundary. The wave incident on the first boundary is assumed to have known amplitude, $\tilde{E}_{iI}$. Thus we have a set of 2 equations for

2 unknowns $\tilde{E}_{r1}$ and $\tilde{E}_{ts}$. These equations give us the ratio of the total reflected and transmitted waves to the incident wave:

$$\begin{aligned}
\frac{\tilde{E}_{ts}}{\tilde{E}_{iI}} &= \frac{2\tilde{k}_0 e^{-i\tilde{k}_s d_P}}{\tilde{k}_0 m_{11} + \frac{\lambda_0}{2\pi}\sqrt{\frac{\epsilon_0}{\mu_0}}\tilde{k}_0\tilde{k}_s m_{12} + \frac{2\pi}{\lambda_0}\sqrt{\frac{\mu_0}{\epsilon_0}} m_{21} + \tilde{k}_s m_{22}} \\
\frac{\tilde{E}_{r1}}{\tilde{E}_{iI}} &= \frac{\tilde{k}_0 m_{11} + \frac{\lambda_0}{2\pi}\sqrt{\frac{\epsilon_0}{\mu_0}}\tilde{k}_0\tilde{k}_s m_{12} - \frac{2\pi}{\lambda_0}\sqrt{\frac{\mu_0}{\epsilon_0}} m_{21} - \tilde{k}_s m_{22}}{\tilde{k}_0 m_{11} + \frac{\lambda_0}{2\pi}\sqrt{\frac{\epsilon_0}{\mu_0}}\tilde{k}_0\tilde{k}_s m_{12} + \frac{2\pi}{\lambda_0}\sqrt{\frac{\mu_0}{\epsilon_0}} m_{21} + \tilde{k}_s m_{22}}.
\end{aligned} \tag{4.43}$$

Note that these equations are linear in $\tilde{E}_{iI}$ as expected. Furthermore, we define all of our fields in such a way that the exponential decay component has unit magnitude at the first interface ($z = 0$), rather than at the interface from which the wave is reflected or transmitted, and thus these ratios are not *'r'* and *'t'* as defined in Hecht (pg. 313 in [48]). They may however be used to calculate the total absorption, reflection, and transmission, if the transmission amplitude is re-scaled appropriately. Given the incoming wave $\tilde{E}_{iI}$, the process to solve for the electric field throughout the whole stack is as follows:

- First we find the total electric and magnetic fields at the first and last boundaries using equations 4.43 and 4.35, noting that $\tilde{E}_{t(P+1)} \equiv \tilde{E}_{ts}$, $\tilde{E}_{t(0)} \equiv \tilde{E}_{iI}$, and $\tilde{E}_{r(P+2)} \equiv 0$.
- Next we use our transfer matrices (4.38) recursively to solve for the total electric field, $\tilde{E}_N$, and magnetic field, $\tilde{H}_N$, at each boundary, N, within the stack.
- Then we solve equations 4.37 to get the transmitted, $\tilde{E}_{tN}$, and reflected, $\tilde{E}_{r(N+1)}$, electric wave amplitudes inside each film in terms of the total electric and magnetic field at the subsequent boundary.

- Finally, given the wave amplitudes $\tilde{E}_{tN}$ and $\tilde{E}_{rN}$ for each N, we can calculate the electric field at any point in space/time as a vector sum of the reflected and transmitted waves using equations 4.34.

Calculating Joule Heating

In order to calculate the heat generation due to Joule heating, we examine the drop in field intensity. We can calculate the flux in energy carried by the field using the Poynting Vector (pg. 139 in Ref [77]):

$$I(z) \equiv < \overrightarrow{S}(z) >= \frac{c}{8\pi} Re(\overrightarrow{E}(z) \times \overrightarrow{H}^{*}(z)) \tag{4.44}$$

where c is the speed of light in vacuum, and the only spatial dependence is in the direction of propagation $\hat{z}$ due to the plane-wave assumption. Using equation 4.31 we can re-write the magnetic field in terms of the electric field to give the following expression for the intensity in the n^{th} film layer:

$$I(z) = \frac{c\lambda_0}{16\pi^2}\sqrt{\frac{\epsilon_0}{\mu_0}} Re\{[\tilde{E}_{tN}e^{i\tilde{k}_n z} + \tilde{E}_{r(n+1)}e^{-i\tilde{k}_n z}] \times [\tilde{k}_n\tilde{E}_{tN}e^{i\tilde{k}_n z} - \tilde{k}_n\tilde{E}_{r(n+1)}e^{-i\tilde{k}_n z}]^{*}\}, \tag{4.45}$$

If we express the complex wave amplitude in terms of a real amplitude and phase, and write the wave number explicitly in terms of its real and complex components we can simplify our calculation of the intensity. We make the following substitutions:

$$\tilde{E}_{tN} = E_{tn}e^{i\delta_{tn}},$$

$$\begin{aligned}\tilde{E}_{r(N+1)} &= E_{r(n+1)}e^{i\delta_{r(n+1)}},\\ \tilde{k_n} &= \frac{2\pi(n_{rn}+i\,n_{cn})}{\lambda_0} = k_{rn}+i\,k_{cn},\end{aligned} \tag{4.46}$$

where k_{rn} is the real part of the wave number, and k_{cn} is the imaginary part. This gives for the intensity:

$$\begin{aligned}I(z) &= \frac{c\lambda_0}{16\pi^2}\sqrt{\frac{\epsilon_0}{\mu_0}}\Big[k_{rn}(E_{tn}^2e^{-2k_{cn}z}-E_{r(n+1)}^2e^{2k_{cn}z})\\ &+ 2k_{cn}E_{tn}E_{r(n+1)}\sin(\delta_{r(n+1)}-\delta_{tn}-2k_{rn}z)\Big],\end{aligned} \tag{4.47}$$

where the sinusoidal term in 4.47 has to do with the interference of the transmitted wave traveling in the $\hat{z}^+$ direction and the reflected wave traveling in the $\hat{z}^-$ direction.

Heating is then related to the drop in intensity across the film. Since the intensity is the power stored in the field per unit area, we note that the derivative with respect to space in the direction of propagation is the power loss density. Thus we get the following expression for the heat generation per unit volume, $Q(z)$ in $\frac{W}{m^3}$:

$$\begin{aligned}Q(z) &= \frac{-dI(z)}{dz}\\ &= \frac{ck_{rn}k_{cn}\lambda_0}{8\pi^2}\sqrt{\frac{\epsilon_0}{\mu_0}}\Big[2E_{tn}E_{r(n+1)}\cos(\delta_{r(n+1)}-\delta_{tn}-2k_{rn}z)+\\ &\quad E_{tn}^2e^{-2k_{cn}z}+E_{r(n+1)}^2e^{2k_{cn}z}\Big]\end{aligned} \tag{4.48}$$

Typical plots are given in Figures 4.21, 4.22, and 4.23 for a vacuum-device-vacuum-substrate film stack with silicon device layer of varying thickness, fixed

400nm gap-to-substrate, and a semi-infinite silicon substrate. A laser wavelength of λ_0 =633nm is used, and 1 $\frac{W}{\mu m^2}$ incident intensity. Note that the intensity is continuous across the interfaces by assumption, but Joule heating is not due to the discontinuity in the wave number. While the Joule heat is periodic, the intensity is a strictly decreasing function of distance through the film as energy in the incident wave is irreversibly dissipated in the form of heat. Note that the modulation in the intensity has spatial period of $\frac{\lambda}{2}$ from the $2k_{rn}z$ term in 4.48, where λ is the wavelength *in the medium*, and is roughly 164 nm for a HeNe laser in silicon. For thin devices, the reflected wave is large in magnitude, and thus the oscillations in Joule heating are pronounced. As devices get thicker, the reflected wave is smaller, the oscillations decay, and the behavior tends more to strict exponential decay of fields and Joule heating which is the known solution for waves impinging on a semi-infinite conductor.

In conclusion, for devices thinner than their optical skin depth illuminated with a monochromatic light source, heating is not confined to the top surface, but rather periodically distributed throughout the interior due to interference between reflected and transmitted waves. In order for absorption/reflection to couple to displacement in a MEMS device, a Fabry-Pérot interferometer must be set up between the device and substrate below[18]. Thus, devices must be thinner than their skin depth to allow waves to penetrate to the gap-to-substrate and as such absorption will be periodically distributed throughout the device thickness. As a result, in devices capable of exhibiting optically induced thermo-mechanical feedback oscillations, heating due to absorption is **not** confined to

[18]That is of course, unless a partially reflective surface is placed in the beam path in front of a highly reflective device, creating the interference cavity in front of the device rather than behind it. This has been done previous by Langdon and Dowe among others [67], though it complicates the experimental setup. Stabilization of the partially reflective surface was seen to be challenging.

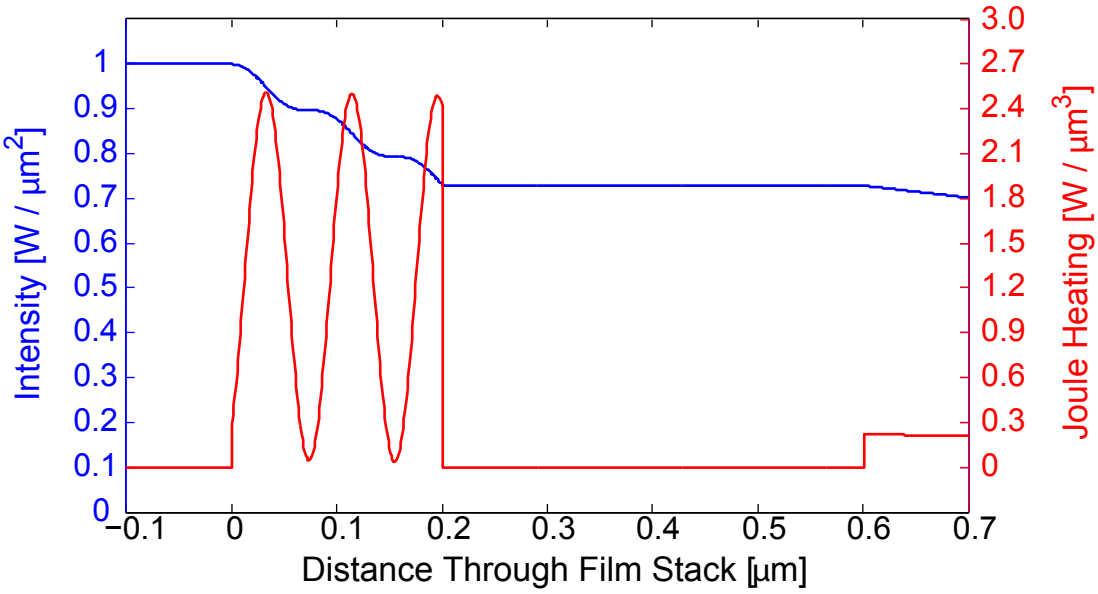

Figure 4.21: Joule Heating in 0.201 μm thin device with 0.4 μm gap-to-substrate. Distance is measured through the film stack with $z = 0\,\mu$m at the top surface of the device layer, $z = 0.201\,\mu$m at bottom of the device layer, and the substrate starting at $z = 0.601\,\mu$m. Note the continuity in intensity but discontinuity in Joule heating at each boundary.

the top surface of the device.

4.5 1D Thermal Modeling

In Section 4.1, we used a static thermo-mechanical analysis to study the coupling between heating and displacement in doubly-supported beams. Later, a three-dimensional transient thermal analysis was performed in order to calculate the lumped thermal mass and time constant used in a model of limit cycle oscillation. Analysis indicated that changes in the average temperature across the beam rather than temperature gradients at the anchor point led to out-of-

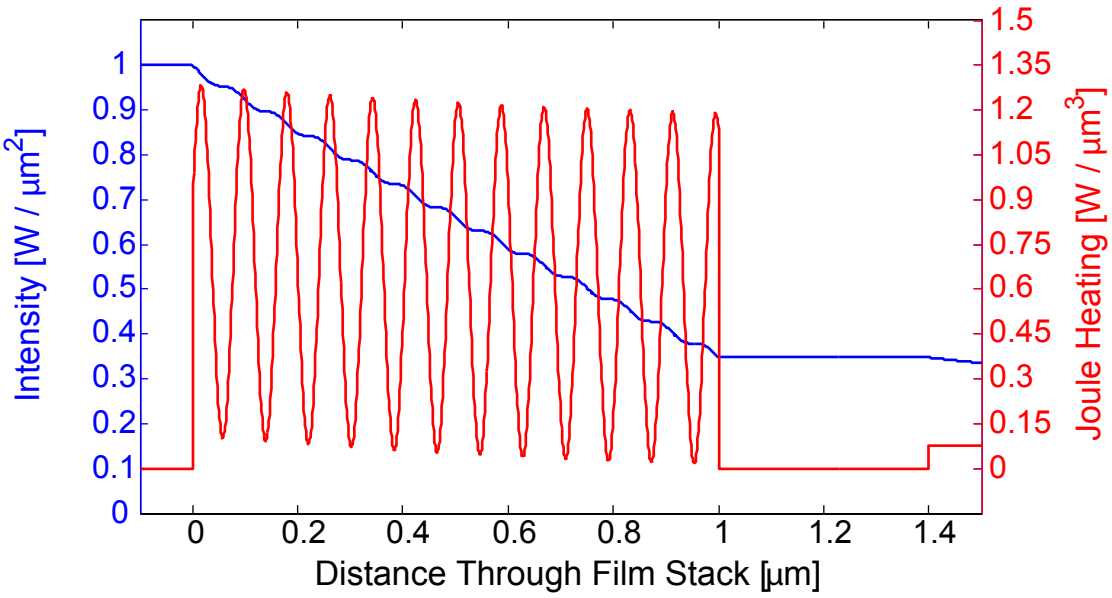

Figure 4.22: Joule Heating in 1 μm thin device with 0.4 μm gap-to-substrate. Distance is measured through the film stack with $z = 0\,\mu$m at the top surface of the device layer, $z = 1\,\mu$m at bottom of the device layer, and the substrate starting at $z = 1.4\,\mu$m.

plane deflection, and thus we were justified in using a one-dimensional thermal model which would capture the average temperature across a device but not the temperature distribution at the anchor support. While lumped parameter models cannot account for temperature distribution within the extended system, they can account for phase lag. An early model of self-oscillation in thermo-optically transduced micro beams by Churenkov, suggested that excitation depended critically on the phase-difference between absorbed power and thermoelastic stress [19]. In this section we offer analytic solutions of the one-dimensional heat equation for a sinusoidally heated beam semi-infinite length, present numerical solutions for a beam of finite length, and discuss phase and

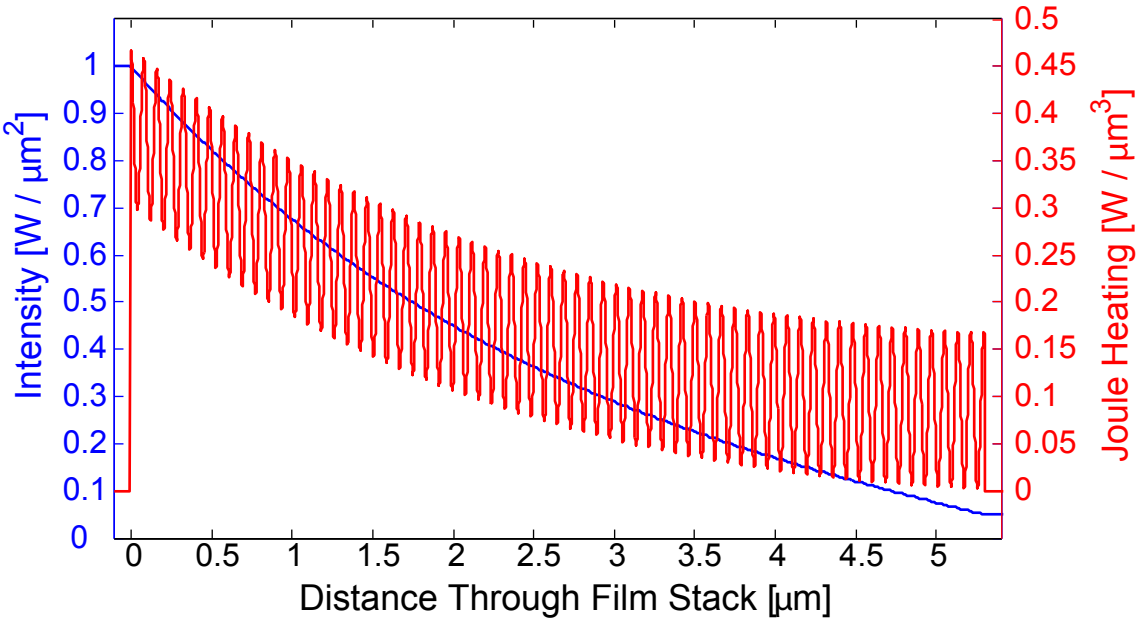

Figure 4.23: Joule Heating in 5.3 μm thin device *(skin depth of silicon)* with 0.4 μm gap-to-substrate. Distance is measured through the film stack with $z = 0\,\mu$m at the top surface of the device layer, $z = 5.3\,\mu$m at bottom of the device layer, and the substrate starting at $z = 5.7\,\mu$m. Note that the intensity (*square of field amplitude*) has been reduced by a factor of $\sim \frac{1}{e^2}$ by the bottom of the device layer.

attenuation of one-dimensional thermal waves.

Analytic Solution:

Consider a semi-infinite, one-dimensional beam defined on $x > 0$, to which a sinusoidal heat flux is applied. The governing equations are:

$$U_{xx} = \frac{1}{\alpha_c} U_t; \;\; x > 0, \;\; t > 0 \tag{4.49}$$

with α_c the thermal diffusivity in $\left[\frac{m^2}{s}\right]$, U the temperature above ambient in $[K]$, and subscripts used to denote partial derivatives. We apply the following

boundary and initial conditions:

$$\begin{aligned} B.C.: \; U(x,t) &= 0, \; x \to \infty, \; t > 0, \\ U_x(0,t) &= A \sin(\omega t), \\ I.C.: U(x,0) &= 0. \end{aligned} \tag{4.50}$$

Duhamel's Theorem may be used to solve (4.49,4.50). Letting $t \to \infty$ we obtain the steady state solution:

$$U(x,t) = \frac{\delta A}{\sqrt{2}} e^{\frac{-x}{\delta}} \cos\left(\omega t - \frac{x}{\delta} + \frac{\pi}{4}\right), \tag{4.51}$$

where the exponential term in (4.51) defines a decay envelope which determines the amplitude of oscillation at a point in space and the cosine term in (4.51) gives the phase of oscillation. The thermal diffusion length, δ, is the length over which the wave amplitude is reduced by a factor of $\frac{1}{e}$. This characteristic thermal length decreases with frequency and is defined as:

$$\delta = \sqrt{\frac{2\alpha_c}{\omega}}. \tag{4.52}$$

In addition, it is clear from (4.51) that $2\pi\delta$ is the distance between points at the same phase.

Instead of a characteristic length, we may think of a critical *angular* frequency, $\omega_{crit} = \frac{2\alpha_c}{x^2}$, at which heat is confined within a distance x of the point of heating. Note that the critical frequency for heating has the same dependence on length as the mechanical resonant frequency which determines the

frequency of heating (see Section 2.2.2)[19]. The thermal diffusion length and critical frequency for singly- and doubly-supported devices from Chip I are calculated using the measured resonant frequency from Section 2.2.2, and are given in Table (4.8). For the critical frequency, we assume centerline illumination in doubly-supported beams, i.e. $x = \frac{L}{2}$, and assume tip illumination in singly-supported beams, i.e. $x = L$. Note that the thermal diffusion length is roughly one sixth to one ninth the device length for doubly-supported devices, and one third the device length for singly-supported devices. At the same time, it is six to sixty times the device thickness. As a result, the through thickness critical frequency for singly- and doubly-supported devices is $f_{crit} = \frac{\omega_{crit}}{2\pi} = 785$ MHz. In the following sections we examine the phase and amplitude of the average temperature and thermal moment as a function of frequency for in-plane and through thickness temperature distributions.

Length [μm]	7	10	15	20	25	30	35	40
δ (doubly-supported) [μm]	1.24	1.62	2.42	2.98	3.29	3.69	4.08	4.39
ω_r/ω_{crit} (doubly-supported) [1]	7.99	9.55	9.63	11.2	14.4	16.5	18.4	20.8
δ (singly-supported) [μm]	2.61	3.65	5.61	7.30	9.03	10.9	12.6	N/A
ω_r/ω_{crit} (singly-supported) [1]	7.17	7.51	7.15	7.51	7.66	7.59	7.76	N/A

Table 4.8: Thermal diffusion length, δ, and across length critical frequency ω_{crit} for singly- and doubly-supported devices from Chip I using α_c from Section 4.3. Thermal diffusion lengths for devices from Chip II, are within 10% of those for Chip I.

Numerical Solutions Across Length:

Assuming a semi-infinite beam for the analytic solutions above allows us to neglect reflected thermal waves and greatly simplifies the analysis. In addition, the calculated thermal diffusion length for our devices was seen to be a fraction

[19]Ignoring the effects of pre-stress on frequency in doubly-supported beams.

of the length, suggesting that reflected thermal waves should be small in amplitude. In this section, we numerically solve equation (4.49) on the finite interval $0 < x < h$, and compare the calculated phase and amplitude of the average temperature with that calculated using the lumped parameter model in Section 4.2.

The heat equation (4.49) remains the same, though we get a new solution interval and boundary condition. We assume the substrate acts as a perfect heat sink and use a Dirichlet boundary condition at $x = 0$. We further assume periodic heating at $x = h$ to get:

$$\begin{aligned} U_{xx} &= \frac{1}{\alpha_c} U_t;\ 0 < x < h,\ t > 0 \\ B.C.:\ U(0,t) &= 0 \\ U_x(h,t) &= \frac{I}{k} \sin(\omega t) \\ I.C.: U(x,0) &= 0 \end{aligned} \tag{4.53}$$

where I is the laser intensity in $\left[\frac{W}{m^2}\right]$ and $k = 170\left[\frac{W}{m\,K}\right]$ is the thermal conductivity. To calculate the intensity, we assume the beam has thickness 201 nm and width 2 μm, and that 1 mW is incident on the beam with 4% absorbed across the interior cross-section, giving $I = 7.96 \times 10^7\left[\frac{W}{m^2}\right]$.

Equation (4.53) is solved numerically in MATLAB using the built in initial-boundary value solver for 1D parabolic-elliptic PDEs, `pdepe`. A domain length of $h = 5$ μm is selected to model a 10μm beam subject to centerline illumination. A spatial mesh is selected based on the heating frequency, ω, which ensures at least 100 nodes across the interval, h, and at least 5 nodes per thermal diffusion length, δ. Transient behavior is integrated out, and then the solution is

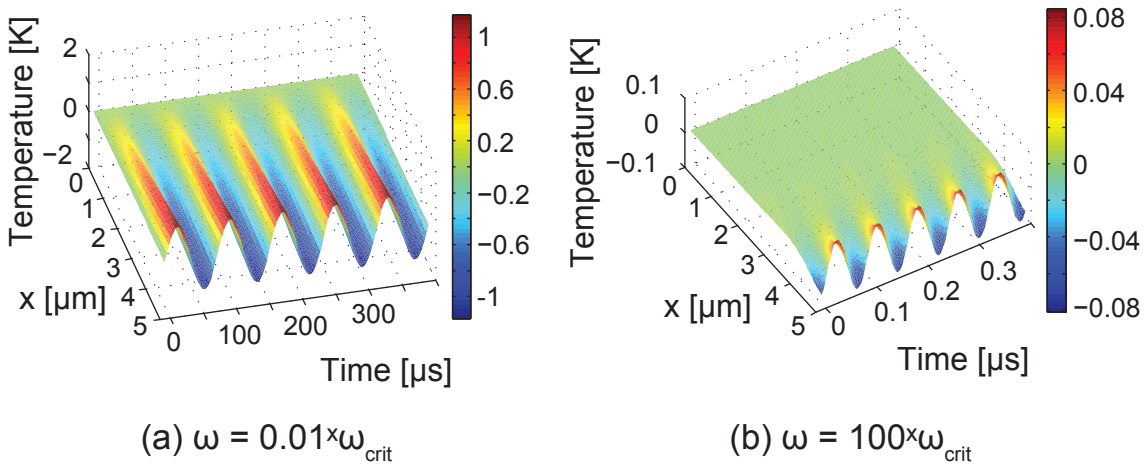

Figure 4.24: Surface plots of the temperature distribution as a function of length in a 10 μm beam sinusoidally heated: (a) below the critical frequency at $\omega = \frac{1}{100}\omega_{crit}$; and (b) above the critical frequency at $\omega = 100\omega_{crit}$.

requested at every $\frac{1}{25}^{th}$ the period for 5 periods. Finally, the average temperature is calculated at each time step, and fit to a sine-wave in order to determine the amplitude, and phase-lag with respect to heating.

Surface plots of the temperature distribution as a function of length are given in Figure 4.24. Note that for heating below the critical frequency the beam is always in thermal equilibrium - i.e. the temperature distribution at a given point in time is a straight line - while for heating above the critical frequency, excess temperature is confined to a small region near the beam center. The amplitude of the average temperature as a function of time, and phase lag with respect to heating are calculated using both the spatially extended 1D thermal model and lumped parameter model (from Section 4.2), and results are presented in Figure 4.25. Parameters used in the lumped parameter model are those presented in Section 4.2, transformed to dimensionally appropriate units[20]. Note that am-

[20]The lumped parameter model was based on the temperature at the centerline rather than

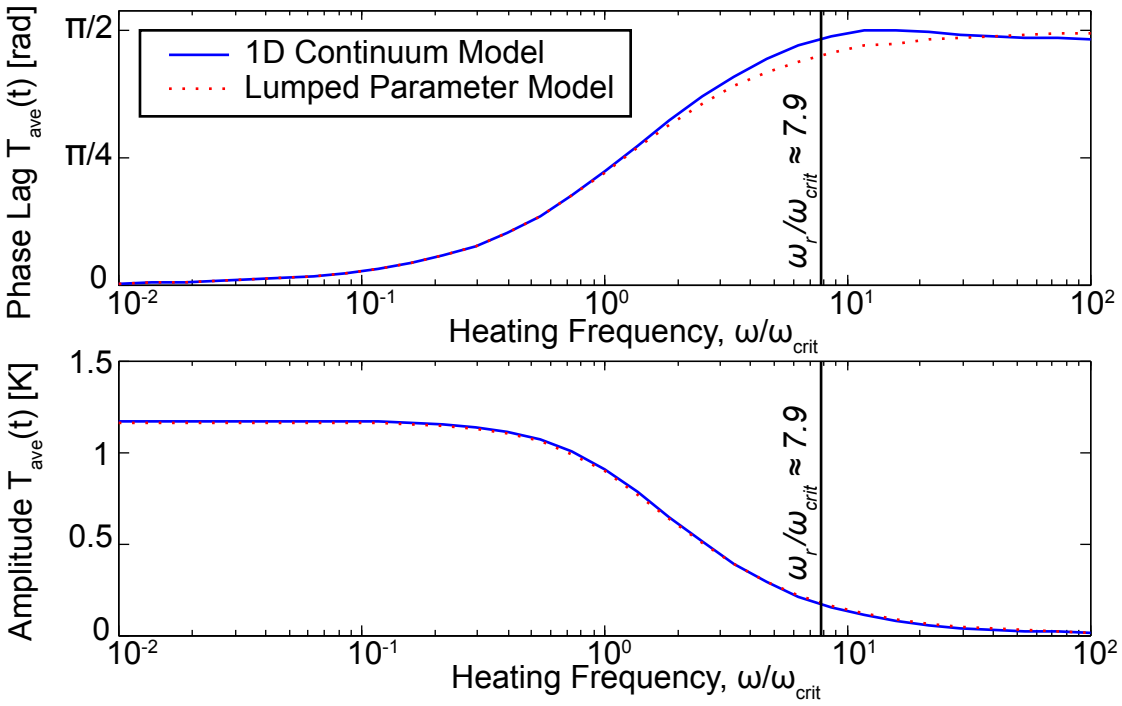

Figure 4.25: The amplitude and phase with respect to heating of the average temperature in a 10 μm device calculated using 1D continuum model and lumped parameter model. When the amplitude of motion is smaller than the optical critical amplitude (see Section 2.4.5) device heating occurs at the mechanical resonant frequency ω_r indicated on the plot (device from Chip II). For higher amplitude motion, heating occurs at harmonics of ω_r due to movement through peaks of the interference field.

plitude results are almost identical, and phase results similar, suggesting that the lumped parameter model is sufficient to capture the behavior of optically driven beams whose displacement depends on the average temperature across the device. Given that device heating in our devices occurs at a frequency 7 – 20 times greater than ω_{crit} (see Table 4.8), we operate in a regime where there is considerable phase lag between heating and average temperature with small, but non-negligible temperature amplitude.

the average temperature. Amplitude results for the lumped parameter model have been scaled by a factor of 0.5× to account for this difference in definition.

Numerical Solutions Through Thickness:

Next we examine the frequency dependent phase and amplitude of thermal moments generated due to *surface* absorption, by amending equation 4.53. We model a device with optical coatings used to ensure surface heating, and assume the incident laser is evenly absorbed across the top surface of the device. Thus we apply an insulated boundary condition to the bottom surface, i.e. $U_x(0,t) = 0$, and h becomes the device thickness. We still assume 1 mW incident power, though absorbed over a $2 \times 10\ \mu m^2$ area, giving $I = 1.60 \times 10^6 \left[\frac{W}{m^2}\right]$ for a 10 μm beam. The moment is calculated based off of the temperature distribution using:

$$M(t) = \int_0^h \alpha_e E W U(x,t)\left(x - \frac{h}{2}\right) dx, \tag{4.54}$$

where $\alpha_e = 2.5 \times 10^{-6}\ [K^{-1}]$ is the coefficient of thermal expansion, $E = 130$ GPa is the Young's modulus, and $W = 2\mu$m is the beam width. Once again, equation (4.53) is solved numerically in MATLAB but with updated boundary condition and a domain length of $h = 201$ nm. The moment is calculated at each time step, and fit to a sine-wave in order to determine the amplitude, and phase-lag with respect to heating. Results are shown in Figure 4.26. Note that mechanical resonant frequencies of our singly- and doubly supported devices are in the range of $10^{-1} - 10^{1}$ MHz, orders of magnitude lower than the through thickness critical frequency of $f_{crit} = 785$ MHz. Thus, even if devices were coated to confine heating to the top surface, through-thickness temperature moments would be in-phase with heating/displacement.

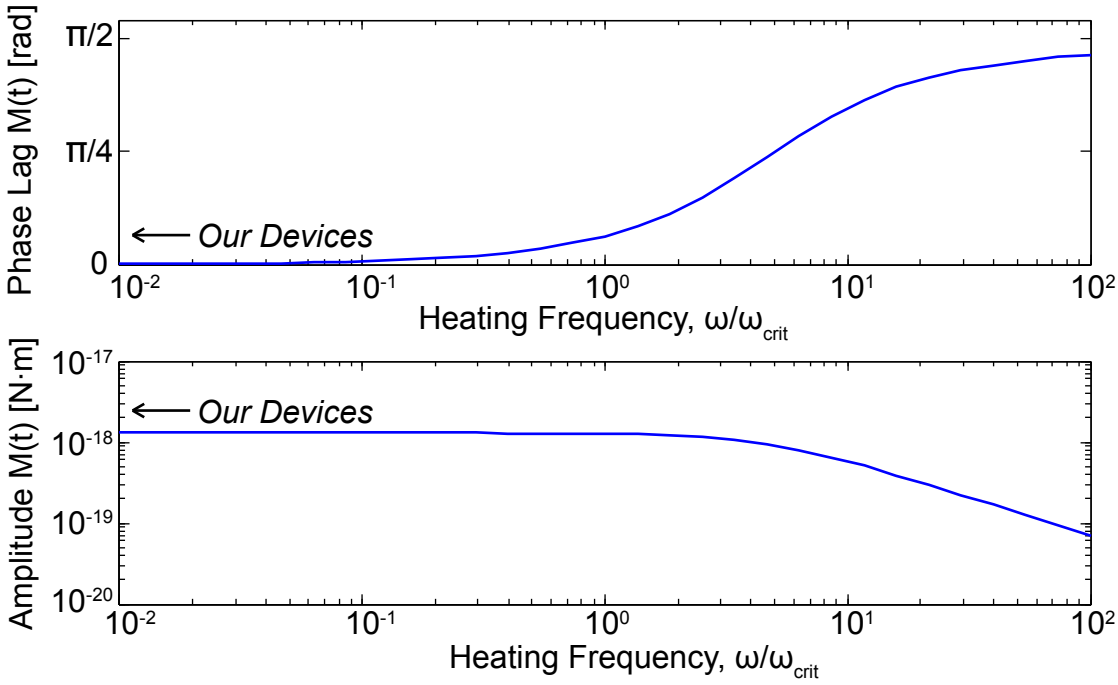

Figure 4.26: The amplitude and phase with respect to heating of the moment calculated using 1D continuum model with insulated boundary condition.

CHAPTER 5

CONCLUSIONS AND FUTURE WORK

In closing we summarize what was discovered while conducting this research, and what contributions were made to the field of optically-transduced MEMS resonators - recognizing that this is not the first body of work in the area, and hoping that it will not be the last. In addition we will suggest directions for future work in the area.

Transition to Limit Cycle Oscillation:

Initially discovered by Langdon and Dowe 25 years ago, significant work exists in the area of optically excited limit cycle oscillations in MEMS resonators. In the following years, competing theories developed as to the conditions which gave rise to such self-oscillations. Though most researchers agreed that oscillations were caused by feedback between displacement and absorption/reflection of light, disagreement remained as to the specifics of the thermo-mechanical coupling. In addition, models were developed to reproduce experimental data for specific devices of various geometry. However, the need for extensive parameter estimation limited their predictive capacity.

In this dissertation, we examined uncoated optically-thin beams. Singly- and doubly-supported devices ranging in length from 7-40 μm were fabricated, and the threshold power for self-oscillation, P_{Hopf} measured in Section 3.1. To the author's knowledge, the data presented there represents the most comprehensive set on devices of a fixed geometry. P_{Hopf} was seen to vary in a complex manner on beam length and location of illumination. A first-principles model

of self-oscillation in doubly-supported beams was simultaneously developed which indicated the need for better understanding of the nature of the thermo-mechanical coupling in such devices.

In order to study deflection in initially straight doubly-supported devices due to laser absorption, an FEM model was built. Results indicated that out-of-plane deflection was due to in-plane thermal stresses which tended to bend devices up when heated due to support asymmetry, and not due to vertical thermal gradients at the support which tended to bend singly-supported devices down when heated due to the thermostat effect. The implications of this analysis are:

- Since deflection in doubly-supported beams is due to average excess temperature and not the distribution of that temperature, the phase lag of thermal-waves at the anchor is insignificant, and lumped parameter modeling is valid. Further validation of lumped parameter modeling is presented in Section 4.5.
- Direction of deflection is one element determining the sign of the feedback gain in thermo-optically excited devices. As such, for a singly-supported and doubly-supported beam at the same location within the interference field, one would experience positive feedback leading to self oscillation, and the other negative feedback leading to vibration damping.

Results of the FEM model were incorporated into a first principles model of self-oscillation presented in Section 4.3. Model reduction using a Galerkin projection produced the same equations as prior ad-hoc models, but model parameters were expressed in closed-form in terms of geometric and material properties. Perturbation theory was used to derive an approximate formula for P_{Hopf}

which was verified using numerical continuation and compared to experimental results. The model suggested that devices with compressive pre-stress levels between the transition region and buckled region should have the lowest power for self-oscillation. This conclusion could not be firmly made based on the data, in part due to the large out-of-plane deflection with respect to the period of the interference field.

Although the inclusion of support asymmetry within our model via deflection per unit temperature rise was sufficient to describe the effect of imperfection on P_{Hopf}, it was insufficient to predict the out-of-plane deflection or change in resonant frequency due to imperfection. Limited work exists in modeling the deflection or frequency of imperfect microbeams, and available experimental data is even more limited. Given that the standard method for measuring device-layer pre-stress in deposited films is based on perfect-buckling, better models of imperfection buckling could yield better methods for measuring device pre-stress based on out-of-plane deflection and frequency of doubly-supported beams.

Finally, an analysis of absorption, reflection, and transmission from a thin film stack was presented in Section 4.4. This work was initially done in support of the FEM modeling. It represented an improvement on the analysis by Sekaric [111], who did not determine where within the stack the incident laser power is absorbed [111]. We found that interference between reflected and transmitted waves results in Joule heating within the film whose spatial distribution is described by sinusoidal variation within an exponential decay envelope.

Frequency Tuning:

The frequency of oscillation of singly- and doubly-supported devices was measured as a function of laser power on sample. For powers lower than P_{Hopf} the small amplitude inertially driven frequency was measured, and for powers greater than P_{Hopf} the limit cycle frequency was measured. In doubly-supported beams, results indicated a competition between linear frequency tuning due to in-plane tension, and non-linear frequency tuning due to the amplitude-frequency relationship (see Section 3.2). The existence of these competing effects was predicted in our earlier work where large amplitude motions were examined in ad-hoc model equations using numerical continuation (see Section 4.2). Unfortunately, model parameters used were not those for devices in which limit cycle oscillation was later seen experimentally. In that same section we showed that if we do not assume small deformation, past ad-hoc models also predict multiple stable limit cycles periodically spaced in amplitude due to periodicity in the interference field, as well as period doubling and secondary Hopf bifurcations. Model parameters appropriate to the devices under test were presented in Appendix B for the *a priori* model derived in Section 4.1. Qualitative analysis of the results presented in Section 3.2 using the equations presented in Appendix B is forthcoming.

Though limited data is presented in this dissertation on the subject, we also discovered that variation in the laser power could lead to frequency noise in doubly-supported beams via the power-amplitude-frequency relationship. This result is of particular interest because of the recent attention paid to frequency-noise in resonant MEMS for chemical sensing. Results were also presented for singly-supported devices which exhibited negligible frequency-tuning, had relatively weak amplitude-frequency relationship, and exhibit significantly less frequency noise than doubly-supported ones.

We note that the relationship between tunability and frequency noise would not be specific to feedback oscillations in optically-transduced MEMS, but would be equally applicable to electrostatic feedback oscillations. Further work would involved separating out noise due to aliasing of the laser power from adsorption-desorption noise, thermal background fluctuations, and other sources of noise.

A significant body of work exists on tuning linear and non-linear frequency of MEMS resonators. In conjunction with a means to determine the sign of non-linearity from noise statistics, this work suggests that one could infer the level of non-linearity and tune it in order to reduce frequency noise.

Entrainment:

Entrainment of a limit cycle oscillator was first discovered by Balthasar van der Pol in 1920, and was later demonstrated within the field of MEMS by Maxim Zalalutdinov 83 years later. Zalalutdinov demonstrated 1:1 and 2:1 entrainment, illustrating how it could be used to stabilize a noisy limit cycle oscillator. In this dissertation we measured the statistics of entrainment illustrating that noise in the LCO frequency leads to transient locking for low forcing amplitudes.

Past modeling work by Pandey suggested that amplitude hardening limit cycle oscillators are constrained to entrain to the backbone curve. We examined the region of primary entrainment as a function of the operating point on the backbone curve of an amplitude-softening oscillator, showing that hysteresis is most prominent at the base of the backbone curve. This phenomenon had previously been observed by Zalalutdinov and attributed to frequency noise, though

no data was presented. In light of Pandey's analysis and our data it appears that hysteresis in the region of entrainment is due to the amplitude-frequency relationship: e.g. for an amplitude-hardening limit cycle, when sweeping the drive frequency up, an entrained limit cycle can ride up the backbone curve; However, when sweeping down entrainment must cease when the base of the backbone curve is reached.

Regions of primary, subharmonic, and superharmonic entrainment were also mapped out for a both doubly- and singly-supported devices. In doubly-supported beams subharmonic entrainment up to 3:1 and superharmonic entrainment up to 1:7 was demonstrated as well as primary entrainment with relative frequency width of up to $\sim 25\%$. In comparison, in singly-supported beams sub- and superharmonic entrainment were not seen, and the region of primary entrainment had a relative frequency width of less that $\sim 0.45\%$. Results suggest that the strength of non-linearity is responsible for both the width of the primary entrainment region and level of sub- or superharmonic entrainment possible. Further modeling and analysis of entrainment results is forthcoming.

We note that Van der Pol's original work demonstrating 200:1 subharmonic entrainment was on a relaxation oscillator - a highly non-linear oscillator with two-time scale motion. At the same time, large amplitude vibrations of MEMS limit cycle oscillators with strong amplitude-frequency relationships exhibit a two-time scale response due to the stiffness non-linearity. As such it is of particular interest to discern whether high order subharmonic entrainment is made possible by variability in the limit cycle frequency or two-time scales in the limit cycle motion. Preliminary results based on the order of entrainment possible at various locations along the backbone curve point to the former.

APPENDIX A

CALCULATION OF IMPERFECTION LEVEL

Throughout this dissertation, two separate mathematical descriptions of imperfection level are used depending on the context. Fang's original work on imperfection buckling in microbeams lumped together all sources of imperfection into a pre-deformation of the initial configuration with centerline amplitude $w^*_{max} = \gamma_{imp} L$, where γ_{imp} is the non-dimensional imperfection level, and L is the beam length [34]. In Section 2.2.3 we use this description to determine the imperfection level in our beams using optical profilometry data.

In Section 4.1, we explicitly probe one source of imperfection, anchor support asymmetry, using finite element modeling. In that model, the beam is initially straight, and the level of imperfection is described by the slope of the load curve $\left(\frac{dx}{dT}\Big|_{T=T^*}\right)$, with T^* the initial temperature above ambient, and x the centerline displacement. Excess temperature (T) is related to compressive stress (σ) via the coefficient of thermal expansion (α_e) and Young's modulus (E) using: $T\alpha_e = \frac{\sigma}{E}$. In Section 4.3, the description of imperfection in terms of thermal-mechanical coupling is used in our first-principles model to fit the imperfection level. In this section of the appendix we describe how we relate these two descriptions and the limitations thereof.

Transforming stress to excess temperature in Fang's "linear model with imperfection" we get an approximation to the load curve in the pre-buckled region and corresponding initial slope:

$$x(T) = \frac{\gamma_{imp} L}{1 - \frac{3T\alpha L^2}{\pi^2 t^2}} \tag{A.1}$$

$$m = \left.\frac{dx}{dT}\right|_{T=0} = \frac{3\gamma_{imp}L^3\alpha_e}{\pi^2 t^2}, \tag{A.2}$$

where x is the centerline displacement, T is the average temperature above ambient, t is the beam thickness, L is the beam length, and α_e is the coefficient of thermal expansion. Ignoring feedback, we get the following equilibrium condition in our model: $c_1 x + c_2 x^3 = c_3 xT + c_5 T$. We perform the perturbation series approximation $T = \epsilon T, x = x_0 + \epsilon x_1 + ...$ to obtain:

$$x(T) = \frac{c_5}{c_1}T + \frac{c_3 c_5}{c_1^2}T^2 + ... \tag{A.3}$$

$$m = \left.\frac{dx}{dT}\right|_{T=0} = \frac{c_5}{c_1}, \tag{A.4}$$

where the constants c_i are defined in Section 4.3 with c_5 describing the imperfection level.

Examining equation A.3, and using the FEM data from Section 4.1 for a 15μm beam under 35 MPa pre-stress we calculate a load curve slope of $m = \frac{c_5}{c_1} = 7.5 \times 10^{-6}\frac{\mu m}{K}$. We further assume that the slope of the load curve scales with length of the beam giving $\frac{m}{L} = \frac{c_5}{c_1 L} = 5.0 \times 10^{-7}\frac{1}{K}$. From the slope per unit length we can calculate c_5 for beams of different lengths using $c_5 = 5.0 \times 10^{-7} c_1 L$ with c_1 in $[\frac{1}{s^2}]$ and L in $[m]$. Comparing equations A.3 and A.1 we get a corresponding imperfection within Fang's framework of $\gamma_{imp} = 1.2 \times 10^{-4}$. This value is somewhat smaller than the $\gamma_{imp} = 3.7 \times 10^{-4}$ which he calculates for his devices, and significantly less than the $\gamma_{imp} = 5.1 \times 10^{-3}$ and $\gamma_{imp} = 6.6 \times 10^{-3}$ which we calculate for our devices on Chip I and II respectively based on measured out of plane deflection (see Section 2.2.3). Thus, it appears that sources other than anchor deformations dominate imperfection levels in actual micro-devices.

Based on the following limitations, we note that calculations are valid only for small imperfection levels with small deviations in length:

- This analysis assumes that the load curve is linear which is approximately true for small imperfection levels in the pre-buckled regime. In the post-buckled regime this is not true, though displacement is governed more by the linear and non-linear stiffness than the imperfection level.
- Under the above assumptions load curves calculated with the same "imperfection level" but different initial stress levels will not be equivalent under translation: i.e. changing the initial stress level *does not* simply change the initial location on a fixed load curve, but rather alters its shape. In particular, this method tends to shrink the actual level of imperfection near buckling when c_1 goes to zero.
- Fang's assumption of initial deformation scaling with length and our assumption of the slope of the load curve at zero pre-stress scaling with length are not equivalent[1].

[1]It is possible to incorporate imperfection in our model using Fang's formalism by including the pre-deformation in the original partial differential equations. Carrying it through the Galerkin projection produces extra non-linear terms in the final ordinary differential equations. This process was examined but deemed to be unnecessarily complicated.

APPENDIX B

MECHANICAL ONLY MODEL

Experimental results presented in Sections 3.2 and 3.3 necessitate an analysis of stiffness non-linearities, and linear frequency as a function of stress level in doubly-supported beams. In this section, we present an analysis of the mechanical equation derived in Section 4.3, with particular attention paid to the linear frequency of oscillation and stiffness non-linearity.

"Perfect" Model

We begin with a discussion of the mechanical model exhibiting perfect buckling, i.e. zero imperfection. Returning to the mechanical equation of motion without imperfection (4.14), relabeling $a \to x$; $b \to T$ for convenience, and rearranging terms we have:

$$\ddot{x} + c_0\dot{x} + c_1\left[1 - \frac{c_3}{c_1}T\right]x + c_2x^3 = 0, \tag{B.1}$$

with parameters given in equations (4.16). Note that c_2 and c_3 are strictly positive and depend only on the device geometry and material properties while $c_1(\sigma)$ decreases linearly with compressive pre-stress: c_1 is positive in the pre-buckled regime; zero at buckling; and negative in the post-buckled regime. Setting the time derivatives $(\ddot{x}, \dot{x})$ equal to zero we get an equilibrium equation, $x\left[1 - \frac{c_3}{c_1}T + c_2x^2\right] = 0$, whose number of solutions depends on the sign of the linear stiffness $k(\sigma, T) = c_1\left[1 - \frac{c_3}{c_1}T\right]$ (i.e. discriminant). Buckling occurs when $k(\sigma, T)$ passes from positive to negative, and the $x = 0$ equilibrium solution goes unstable. This may occur either through pre-stress ($c_1(\sigma)$) or added thermal stress $\left(\frac{c_3}{c_1}T\right)$. We note the following about dynamics in the pre-buckled regime:

- The linear frequency, $\sqrt{c_1\left[1-\frac{c_3}{c_1}T\right]}$, decreases with T to zero at buckling. Thus pre-buckled devices are thermally-relaxing.
- The cubic non-linear stiffness, c_2x^3, has positive coefficient, and there is no quadratically non-linear stiffness. Thus pre-buckled devices are amplitude-hardening.

In the post-buckled regime, there are two stable equilibrium solutions $x = \pm x_b$ with $x_b = \sqrt{\frac{c_3T-c_1}{c_2}}$ and $x = 0$ is unstable. In order to analyze the device dynamics we shift the stable equilibrium back to the origin with the transformation $z = x - x_b$, and obtain:

$$\ddot{z} + c_0\dot{z} + \omega_0^2 z + \alpha z^2 + \beta z^3 = 0; \tag{B.2}$$

$$\omega_0^2 = -2c_1 + 2c_3T, \tag{B.3}$$

$$\alpha = 3\sqrt{c_2c_3T - c_1c_2}, \tag{B.4}$$

$$\beta = c_2. \tag{B.5}$$

$$\tag{B.6}$$

Note that $z = 0$ is now a stable equilibrium solution. Since c_1 is negative in the buckled regime while c_3 and T remain positive, the linear stiffness $k(\sigma, T) = -2c_1 + 2c_3T$ is positive. The cubic non-linearity is unaffected by the transformation, but mixed terms in the expansion produce a quadratic non-linearity. While the cubic non-linearity is hardening due to its positive coefficient c_2, the quadratic nonlinearity is softening regardless of the sign of its coefficient. The effective *(cubic)* non-linearity of the system [86] is $\beta_{eff} \equiv \beta - \left(\frac{10}{9\omega_0^2}\right)\alpha^2$. Plugging in

for the above we get $\beta_{eff} = -4c_2$. We note the following about dynamics in the post-buckled regime:

- The linear frequency, $\sqrt{-2c_1 + 2c_3T}$, increases with T from zero at buckling (since $c_3 > 0$). Thus post-buckled beams are thermally-stiffening.
- Both cubic and quadratic non-linearities exist. The effective *(cubic)* non-linear stiffness $-4c_2x^3$ has negative coefficient (since $c_2 > 0$). Thus post-buckled devices are amplitude-softening.

"Perfect" Model Parameters, Chip *I*				
L_{nom}	$c_0 \left[\frac{1}{\mu s}\right]$	$c_1 \left[\frac{1}{\mu s^2}\right]$	$c_2 \left[\frac{1}{\mu m^2 \mu s^2}\right]$	$c_3 \left[\frac{1}{\mu s^2 K}\right]$
7 [μm]	1.24×10^{-2}	1.54×10^{4}	3.69×10^{5}	1.64×10^{1}
10 [μm]	6.13×10^{-3}	3.76×10^{3}	1.16×10^{5}	9.16×10^{0}
15 [μm]	1.30×10^{-3}	1.69×10^{2}	2.38×10^{4}	4.15×10^{0}
20 [μm]	2.04×10^{-3}	-2.08×10^{2}	8.29×10^{3}	2.45×10^{0}
25 [μm]	2.18×10^{-3}	-2.37×10^{2}	3.56×10^{3}	1.61×10^{0}
30 [μm]	2.04×10^{-3}	-2.07×10^{2}	1.78×10^{3}	1.14×10^{0}
35 [μm]	1.85×10^{-3}	-1.70×10^{2}	9.58×10^{2}	8.34×10^{-1}
40 [μm]	1.69×10^{-3}	-1.42×10^{2}	5.86×10^{2}	6.52×10^{-1}

Table B.1: Table of device parameters calculated for Chip *I* using the perfect model, with σ = 55MPa compressive pre-stress, and effective length, thickness, and material properties from Chapter 2.

"Imperfect" Model

Including the imperfection term into (B.7) we obtain the following:

$$\ddot{x} + c_0\dot{x} + c_1\left[1 - \frac{c_3}{c_1}T\right]x + c_2x^3 = c_5T; \tag{B.7}$$

with parameters given in (4.16). Setting the time derivatives equal to zero we get the same equilibrium equation as before, with a new constant term c_5T. For

$T = 0$ the analysis is exactly as before with linear frequency $\sqrt{c_1\left[1 - \frac{c_3}{c_1}T\right]}$ and non-linear stiffness c_2x^3. Thus, one of the unintended consequences of modeling imperfection in this way is that for low-laser power, the device linear frequency is independent of imperfection level. While this could be true for imperfections caused by asymmetry in the support conditions, it is certainly not true for imperfections in the form of pre-deformation where initial arching would add stiffness to the system.

Since the equilibrium equation is a cubic in x, closed form solutions exist but are unwieldy. We perform a perturbation series approximation for the equilibrium solution, scaling the imperfection level by a small parameter: $c_5 = \epsilon c_5$, $x = x_0 + \epsilon x_1 + ...$ We perturb off of the solution $x_0 = 0$ in the pre-buckled regime and $x_0 = x_b$ in the post-buckled regime. Setting our small parameter to unity and shifting the equilibrium to the origin with the transformation $z = x - (x_0 + \epsilon x_1 + ...)$ we get for the pre-buckled regime:

$$\ddot{z} + c_0\dot{z} + \omega_0^2 z + \alpha z^2 + \beta z^3 = O(\epsilon); \tag{B.8}$$

$$\omega_0^2 = c_1 - c_3T + \frac{3c_2c_5^2T^2}{c_3^2T^2 - 2c_1c_3T + c_1^2} + ..., \tag{B.9}$$

$$\alpha = \frac{3c_2c_5T}{c_1 - c_3T} + ..., \tag{B.10}$$

$$\beta = c_2. \tag{B.11}$$

$$\tag{B.12}$$

Note that a quadratic non-linearity is introduced *in the pre-buckled regime* which is generally small *(scales as c_5)*, though is singular in the region of thermal buckling, i.e. near $T = \frac{c_1}{c_3}$. Thus imperfection may result in amplitude-softening in the transition region proceeding buckling. In addition, for $T \neq 0$ the resonant

frequency, ω_0, depends on the imperfection level, c_5. For $c_5 = 0$ these results reduce to the "perfect" case as expected. For the post-buckled region, we obtain:

$$\ddot{z} + c_0\dot{z} + \omega_0^2 z + \alpha z^2 + \beta z^3 = O(\epsilon); \tag{B.13}$$

$$\omega_0^2 = -2c_1 + 2c_3T + \frac{6c_2c_5Tx_b}{2c_3T - 2c_1} + ..., \tag{B.14}$$

$$\alpha = 3\sqrt{c_2c_3T - c_1c_2} + \frac{3c_2c_5T}{2c_3T - 2c_1} + ..., \tag{B.15}$$

$$\beta = c_2. \tag{B.16}$$

$$\tag{B.17}$$

Once again, for $c_5 = 0$ these results reduce to the "perfect" case as expected.

"Imperfect" Model Parameters, Chip *I*					
L_{nom}	$c_0\left[\frac{1}{\mu s}\right]$	$c_1\left[\frac{1}{\mu s^2}\right]$	$c_2\left[\frac{1}{\mu m^2 \mu s^2}\right]$	$c_3\left[\frac{1}{\mu s^2 K}\right]$	$c_5\left[\frac{\mu m}{\mu s^2 K}\right]$
7 [μm]	1.36×10^{-2}	1.85×10^{4}	3.69×10^{5}	1.64×10^{1}	3.33×10^{0}
10 [μm]	7.41×10^{-3}	5.49×10^{3}	1.16×10^{5}	9.16×10^{0}	1.32×10^{1}
15 [μm]	3.08×10^{-3}	9.51×10^{2}	2.38×10^{4}	4.15×10^{0}	3.40×10^{-1}
20 [μm]	1.59×10^{-3}	2.54×10^{2}	8.29×10^{3}	2.45×10^{0}	1.18×10^{-1}
25 [μm]	8.14×10^{-4}	6.63×10^{1}	3.56×10^{3}	1.61×10^{0}	3.81×10^{-2}
30 [μm]	2.73×10^{-4}	7.44×10^{0}	1.78×10^{3}	1.14×10^{0}	5.08×10^{-3}
35 [μm]	5.13×10^{-4}	-1.32×10^{1}	9.58×10^{2}	8.34×10^{-1}	-1.05×10^{-2}
40 [μm]	6.17×10^{-4}	-1.90×10^{1}	5.86×10^{2}	6.52×10^{-1}	-1.72×10^{-2}

Table B.2: Table of device parameters calculated for Chip *I* using the imperfect model, with $\sigma = 16$MPa compressive pre-stress, and effective length, thickness, and material properties from Chapter 2.

BIBLIOGRAPHY

[1] Milton Abramowitz and Irene A. Stegun. *Handbook of Mathematical Functions with Formulas, Graphs and Mathematical Tables*. Dover Publications, 1964.

[2] Scott G. Adams, Fred M. Bertsch, Kevin A. Shaw, and Noel C. MacDonald. Independent tuning of linear and nonlinear stiffness coefficients. *Journal of Microelectromechanical Systems*, 7(2):172–180, 1998.

[3] S.G. Adams, F.M. Bertsch, K.A. Shaw, P.G. Hartwell, F.C. Moon, and N.C. MacDonald. Capacitance based tunable resonators. *J. Micromech. Microeng.*, 8:15–23, 1998.

[4] O. Arcizet, P.F. Cohadon, T. Briant, M. Pinard, and A. Heidmann. Radiation pressure cooling and optomechanical instability of a micromirror. *Nature*, 444:71–74, 2006.

[5] S. Atluri. Nonlinear vibrations of a hinged beam including nonlinear inertia effects. *Journal of Applied Mechanics*, pages 121–126, 1973.

[6] Keith L. Aubin, Maxim Zalalutdinov, Robert B. Reichenbach, Brian Houston, Alan T. Zehnder, Jeevak M. Parpia, and Harold G. Craighead. Laser annealing for high-Q MEMS resonators. In *Proc. SPIE 5116*, pages 531–535, Maspalomas, Gran Canaria, Spain, May 19, 2003.

[7] Keith L. Aubin, Maxim K. Zalalutdinov, Tuncay Alan, Robert B. Reichenbach, Richard H. Rand, Alan Taylor Zehnder, Jeevak M. Parpia, and Harold G. Craighead. Limit cycle oscillations in CW laser-driven NEMS. *J. Microelectromech. Syst.*, 13(6):1018–1026, 2004.

[8] Keith Lewis Aubin. *Radio Frequency Nano/Microelectromechanical Resonators : Thermal and Nonlinear Dynamics Studies*. PhD thesis, Cornell University, 2005.

[9] David B. Blocher, Richard H. Rand, and Alan T. Zehnder. Multiple limit cycles in laser interference transduced resonators. In *Proceedings of the 2011 ASME Design Engineering Technical Conferences, & Computers and Information in Engineering Conference*, Washington D.C., Aug. 28-31, 2011.

[10] David B. Blocher, Alan Taylor Zehnder, Richard H. Rand, and Shreyasi Mukerji. Anchor deformations drive limit cycle oscillations in interfero-

metrically transduced MEMS beams. *Finite Elem. Anal. Des.*, 49(1):52–57, 2012.

[11] Siebe Bouwstra and Bert Geijselaers. On the resonance frequency of microbridges. In *Digest of Technical Papers, Solid-State Sensors & Actuators (Transducers'91)*, pages 538–542, 1991.

[12] Siebe Bouwstra, Paul Kemna, and Rob Legtenberg. Thermally excited resonating membrane mass flow sensor. *Sensors and Actuators*, 20:213–223, 1989.

[13] Kevin S. Brown and James P. Sethna. Statistical mechanical approaches to models with many poorly known parameters. *Physical Review E*, 68, 2003.

[14] Matthew Bryant and Ephrahim Garcia. Modeling and testing of a novel aeroelastic flutter energy harvester. *Journal of Vibration and Acoustics*, 133, 2011.

[15] Hans-Jürgen Butt and Manfred Jaschke. Calculation of thermal noise in atomic force microscopy. *Nanotechnology*, 6(1):1–7, 1995.

[16] Dustin W. Carr, Stephane Evoy, Lidija Sekaric, Harold G. Craighead, and Jeevak M. Parpia. Measurement of mechanical resonance in nanometer scale silicon wires. *Appl. Phys. Lett.*, 75(7):920–922, 1999.

[17] Dustin W. Carr, Lidija Sekaric, and Harold G. Craighead. Measurement of nanomechanical resonant structures in single crystal silicon. *J. Vac. Sci. Technol. B*, 16(6):3821–3824, 1998.

[18] Xing Chen, LianSheng Ma, YingMei Zheng, and Dong-Weon Lee. Theoretical analysis of postbuckling behavior with experimental validation using electrothermal microbeams. *Applied Physics Letters*, 98(7), 2011.

[19] A.V. Churenkov. Photothermal excitation and self-excitation of silicon microresonators. *Sens. Actuators A*, 39:141–148, 1993.

[20] E. Collin, Y.M. Bunkov, and H. Godfrin. Addressing geometric nonlinearities with cantilever microsystems: Beyond the Duffing model. *Physical Review B*, 82, 2010.

[21] Phanos G. Datskos, Slobodan Rajic, and Irene Datskou. Photoinduced and

thermal stress in silicon microcantilevers. *Applied Physics Letters*, 73:2319–2321, 1998.

[22] Barry E. DeMartini, Jeffrey F. Rhoads, Kimberly L. Turner, Steven W. Shaw, and Jeff Moehlis. Linear and nonlinear tuning of parametrically excited MEMS oscillators. *Journal of Microelectromechanical Systems*, 16(2):310–318, 2007.

[23] Eusebius J. Doedel. Lecture notes on numerical analysis of nonlinear equations. In Bernd Krauskopf, Hinke M. Osinga, and Jorge Gálan-Vioque, editors, *Numerical Continuation Methods for Dynamical Systems: path following and boundary value problems*, pages 1–49. Springer, 2007.

[24] Eusebius J. Doedel, Randy C. Paffenroth, Alan R. Champneys, Thomas F. Fairgrieve, Yuri A. Kuznetsov, Bart E. Oldeman, Björn Sandstede, and Xianjun Wang. *AUTO 2000: Continuation and Bifurcation Software for Ordinary Differential Equations (with HomCont)*, 2002.

[25] Earl H. Dowell, Edward F. Crawley, Howard C. Curtiss Jr., David A. Peters, Robert H. Scanlan, and Fernando Sisto, editors. *A Modern Course in Aeroelasticity (Solid Mechanics and its Applications)*. Springer, 3rd edition, 1995.

[26] E.H. Dowell. Nonlinear oscillations of a fluttering plate. ii. *AIAA Journal*, 5(10):1856–1862, 1967.

[27] J.A. Dunnmon, S.C. Stanton, B.P. Mann, and E.H. Dowell. Power extraction from aeroelastic limit cycle oscillations. *Journal of Fluids and Structures*, 27:1182–1198, 2011.

[28] Joe G. Eisley. Large amplitude vibration of buckled beams and rectangular plates. *AIAA Journal*, 2(12):2207–2209, 1964.

[29] Joe G. Eisley. Nonlinear vibration of beams and rectangular plates. *J. Appl. Math. Phys.*, 15:167–175, 1964.

[30] David A. Evensen. Nonlinear vibration of beams with various boundary conditions. *AIAA Journal*, 6(2):370–372, 1967.

[31] W. Fang and J.A. Wickert. Post-buckling of micromachined beams. In *IEEE Workshop on Micro Electro Mechanical Systems, 1994, MEMS '94*, pages 182–187, 1994.

[32] W Fang and J.A. Wickert. Determining mean and gradient residual stresses in thin films using micromachined cantilevers. *J. Micromech. Microeng.*, 6:301–309, 1996.

[33] Weileun Fang, Chun Hsien Lee, and Hsin Hua Hu. On the buckling behavior of micromachined beams. *J. Micromech. Microeng.*, 9:236–244, 1999.

[34] Weileun Fang and J.A. Wickert. Post buckling of micromachined beams. *J. Micromech. Microeng.*, 4:116–122, 1994.

[35] Rebwar M.A. Fatah. Mechanisms of optical activation of micromechanical resonators. *Sens. Actuators, A*, 33:229–236, 1992.

[36] Jinyang Feng, Xiongying Ye, Masayoshi Esashi, and Takahito Ono. Mechanically coupled synchronized resonators for resonant sensing applications. *J. Micromech. Microeng.*, 20, 2010.

[37] X.L. Feng, C.J. White, A. Hajimiri, and M.L. Roukes. A self-sustaining ultrahigh-frequency nanoelectromechanical oscillator. *Nature Nanotechnology*, 3:342–346, 2008.

[38] Paul A. Flinn. Principles and applications of wafer curvature techniques for stress measurements in thin films. In *Proceedings of the Materials Research Society Symposium, Thin Films: Stresses and Mechanical Properties*, Boston, MA, Nov. 28-30 1988.

[39] Wilhelm Flügge, editor. *Handbook of Engineering Mechanics*. McGraw-Hill, 1962.

[40] Thomas B. Gabrielson. Mechanical-thermal noise in micromachined acoustic and vibration sensors. *IEEE Transactions on Electron Devices*, 40(5):903–909, 1993.

[41] B.J. Gallacher, J. Hedley, J.S. Burdess, and A.J. Harris. Frequency tuning of silicon micromechanical cantilevers using laser ablation. In *Technical Proceedings of the 2003 Nanotechnology Conference and Trade Show, Volume 1*, pages 478–481, 2003.

[42] James M. Gere. *Mechanics of Materials*. Brookes/Cole, 5th ed. edition, 2001.

[43] S. Gigan, H.R. Böhm, M. Paternostro, F. Blaser, G. Langer, J.B. Hertzberg,

K.C. Schwab, D Bäuerle, M. Aspelmeyer, and A. Zeilinger. Self-cooling of a micromirror by radiation pressure. *Nature*, 444:67–70, 2006.

[44] H. Guckel, D. Burnst, C. Rutigliano, E. Lovell, and B. Choi. Diagnostic microstructures for the measurement of intrinsic strain in thin films. *J. Micromech. Microeng.*, 2:86–95, 1992.

[45] K. Hane. Analytical modeling of micromachined resonator sensor activated by CW laser irradiation. In *International Conference on Solid-State Sensors and Actuators, 1997*, pages 105–108, Chicago, IL, USA, June 16-19, 1997.

[46] Kazuhiro Hane and K. Suzuki. Self-excited vibration of a self-supporting thin film caused by laser irradiation. *Sens. Actuators, A*, 51:179–182, 1996.

[47] Chihiro Hayashi. *Nonlinear Oscillations in Physical Systems*. McGraw-Hill, Inc., 1964.

[48] Eugene Hecht and Alfred Zajac. *Optics*. Addison-Wesley Publishing Company, 1974.

[49] Joshua A. Henry, Yu Wang, Debodhonyaa Sengupta, and Melissa A. Hines. Understanding the effects of surface chemistry on q: Mechanical energy dissipation in alkyl-terminated (c_1-c_{18}) micromechanical silicon resonators. *J. Phys. Chem. B*, 111(1):88–94, 2007.

[50] Matthew A. Hopcroft, William D. Nix, and Thomas W. Kenny. What is the young's modulus of silicon? *J. Microelectromech. Syst.*, 19(2):229–238, 2010.

[51] H. Hu. Solution of a quadratic nonlinear oscillator by the method of harmonic balance. *Journal of Sound and Vibrations*, 293:462–468, 2006.

[52] Jeffrey L. Hutter and John Bechhoefer. Calibration of atomic force microscope tips. *Rev. Sci. Instrum.*, 67(4):1868–1873, 1993.

[53] Bojan Rob Ilic, David A. Czaplewski, Harold G. Craighead, Pavel Neuzil, C. Campagnolo, and Carl A. Batt. Mechanical resonant immunospecific biological detector. *Appl. Phys. Lett.*, 77:450–452, 2000.

[54] Bojan Rob Ilic, Slava Krylov, and Harold G. Craighead. Theoretical and

experimental investigation of optically driven nanoelectromechanical oscillators. *J. Appl. Phys.*, 107, 2010.

[55] Bojan Rob Ilic, Slava Krylov, Marianna Kondratovich, and Harold G. Craighead. Optically actuated nanoelectromechanical oscillators. *IEEE J. Sel. Top. Quantum Electron.*, 13(2):392–399, 2007.

[56] J. David Zook, David W. Burns, William R. Herb, Henry Guckel, Joon-Won Kang, and Yongchul Ahn. Optically excited self-resonant microbeams. *Sens. Actuators, A*, 52:92–98, 1996.

[57] John David Jackson. *Classical Electrodynamics*. John Wiley & Sons, INC., 2nd edition, 1975.

[58] Seong Chan Jun, X.M.H. Huang, M. Manolidis, C.A. Zorman, M. Mehregany, and J. Hone. Electrothermal tuning of Al-SiC nanomechanical resonators. *Nanotechnology*, 17:1506–1511, 2006.

[59] Ville Kaajakari, Tomi Mattila, Aarne Oja, and Heikki Seppä. Nonlinear limits for single-crystal silicon microresonators. *J. Microelectromech. Syst.*, 13(5):715–724, 2004.

[60] S.M.M Kafumbe, J.S. Burdess, and A.J. Harris. Frequency adjustment of microelectromechanical cantilevers using electrostatic pull down. *J. Micromech. Microeng.*, 15:1033–1039, 2005.

[61] T.J. Kippenberg, H. Rokhsari, T. Carmon, A. Scherer, and K.J. Vahala. Analysis of radiation-pressure induced mechanical oscillation of an optical microcavity. *Physical Review Letters*, 95, 2005.

[62] Gregory Kovacs. *Micromachined Transducers Sourcebook*. McGraw Hill, 1998.

[63] S.M. Kozel, V.N. Listvin, and A.V. Churenkov. Photothermal self-excitation of mechanical microresonators. *Opt. Spectrosc.*, 69(3):675–677, 1991.

[64] I. Kozinsky, H. W. Ch. Postma, I. Bargatin, and M.L. Roukes. Tuning nonlinearity, dynamic range, and frequency of nanomechanical resonators. *Appl. Phys. Lett.*, 88, 2006.

[65] Walter Lacarbonara. A theoretical and experimental investigation of nonlinear vibrations of buckled beams. Master's thesis, Virginia Polytechnic and State University, 1997.

[66] Theo S.J. Lammerink, Miko Elwenspoek, and Jan H.J. Fluitman. Optical excitation of micro-mechanical resonators. In *IEEE Micro Electro Mechanical Systems, MEMS 1991*, pages 160–165, Nara, Japan, Jan. 30 - Feb. 2, 1991.

[67] R.M. Langdon and D.L. Dowe. Photoacoustic oscillator sensors. In *SPIE Conf. Fiber Opt. Sens.*, pages 86–93, 1987.

[68] Ki Bang Lee and Young-Ho Cho. A triangular electrostatic comb array for micromechanical resonant frequency tuning. *Sensors and Actuators A*, 70:112–117, 1998.

[69] Seungbae Lee, Mustafa U. Demirci, and Clark T.-C Nguyen. A 10-MHz micromechanical resonator pierce reference oscillator for communications. In *Digest of Technical Papers, the 11 th Int. Conf. Solid-State Sens. & Actuators (Transducers'01)*, pages 10–14, 2001.

[70] W. Lestari and S. Hanagud. Nonlinear vibration of buckled beams: Some exact solutions. *International Journal of Solids and Structures*, 38:4741–4757, 2001.

[71] Mo Li, W. H. P. Pernice, C. Xiong, T. Baehr-Jones, M. Hochberg, and H. X. Tang. Harnessing optical forces in integrated photonic circuits. *Nature*, 456:480–485, 2008.

[72] Liwei Lin, Roger T. Howe, and Albert P. Pisano. Microelectromechanical filters for signal processing. *J. Microelectromech. Syst.*, 7(3):286–294, 1998.

[73] N. Liu, F. Giesen, M. Belov, J. Losby, J. Moroz, A.E. Fraser, G. McKinnon, T.J. Clement, V. Sauer, W.K. Hiebert, and M.R. Freeman. Time-domain control of ultraghigh-frequency nanomechanical systems. *Nature Nanotechnology*, 3:715–718, 2008.

[74] Yingming Liu, Xiangzhao Wang, and Xuefeng Wang. Study on silicon micro-resonators by using a novel optical excitation and detection apparatus. *Chinese Optics Letters*, 4(5):309–310, 2006.

[75] Cheng Luo, Anand Francis, and Xinchuan Liu. Determination of com-

pressive residual stress in a doubly-clamped microbeam according to its buckled shape. *Microelectronic Engineering*, 85(2):229–347, 2008.

[76] Pramod Malatkar. *Nonlinear Vibrations of Cantilevered Beams and Plates*. PhD thesis, Virginia Polytechnic and State University, 2003.

[77] Jerry B. Marion. *Classical Electromagnetic Radiation*. Academic Press, 1965.

[78] Jerry B. Marion and Stephen T. Thorton. *Classical Dynamics of Particles and Systems*. Harcourt College Publishers, 4th edition edition, 1995.

[79] Constanze Höhberger Metzger and Khaled Karrai. Cavity cooling of a microlever. *Nature*, 432:1002–1005, 2004.

[80] Ronald E Mickens. Quadratic non-linear oscillators. *Journal of Sound and Vibrations*, 270:427–432, 2004.

[81] Francis Charles Moon. Experiments on chaotic motions of a forced nonlinear oscillator: Strange attractors. *J. Appl. Mech.*, 47(3):638–640, Sept. 1980.

[82] Brian Morgan and Reza Ghodssi. Vertically-shaped tunable MEMS resonator. *Journal of Microelectromechanical Systems*, 17(1):85–92, 2008.

[83] A. Muszynska. Whirl and whip - rotor/bearing stability problems. *Journal of Sound and Vibrations*, 110(3):443–462, 1986.

[84] A.H. Nayfeh, W. Kreider, and T.J. Anderson. Investigation of natural frequencies and mode shapes of buckled beams. *AIAA Journal*, 33(6):1121–1126, 1995.

[85] Ali H. Nayfeh and Samir A. Emam. Exact solution and stability of postbuckling configurations of beams. *Nonlinear Dynamics*, 54(4):395–408, 2008.

[86] Ali H. Nayfeh and Dean T. Mook. *Nonlinear Oscillations*. John Wiley & Sons, Inc., 1979.

[87] Armand Neukermans and Rajiv Ramaswami. MEMS technology for optical networking applications. *IEEE Communications Magazine*, 39(1):62–69, 2001.

[88] Clark T.-C. Nguyen and Roger T. Howe. Microresonator frequency control and stabilization using an integrated micro oven. In *7th International Conference on Solid-State Sensors, Actuators, and Microsystems*, pages 1040–1043, 1993.

[89] D. Niarchos. Magnetic MEMS: Key issues and some applications. *Sensors and Actuators A*, 109:166–173, 2003.

[90] Gregory N. Nielson, Jonathan Wittwer, Leslie Phinney, David Epp, Uma Krishnamoorthy, Vipin Gupta, and Paul Resnick. MEMS solar energy harvesting. Technical Report SANDIA2007-8100, Sandia National Laboratories, 2007.

[91] Manoj Pandey, Keith L. Aubin, Maxim K. Zalalutdinov, Robert B. Reichenbach, Alan Taylor Zehnder, Richard H. Rand, and Harold G. Craighead. Analysis of frequency locking in optically driven MEMS resonators. *J. Microelectromech. Syst.*, 15(6):1546–1554, 2006.

[92] Manoj Pandey, Richard H. Rand, and Alan Taylor Zehnder. Perturbation analysis of entrainment in a micromechanical limit cycle oscillator. *Commun. Nonlinear Sci. and Numer. Simul.*, 12:1291–1301, 2007.

[93] Manoj Pandey, Richard H. Rand, and Alan Taylor Zehnder. Frequency locking in a forced Mathieu-van der Pol-Duffing system. *Nonlinear Dyn.*, 54:3–12, 2008.

[94] Andrew Pember, John Smith, and Henri Kemhadjian. Study of the effect of boron doping on the aging of micromachined silicon cantilevers. *Applied Physics Letters*, 66(5):577–579, 1995.

[95] Kurt E. Petersen. Silicon as a mechanical material. *Proc. IEEE*, 70(5):420–457, 1982.

[96] R.J. Pitcher, K.W.H. Foulds, J.A. Clements, and J.M. Naden. Optothermal drive of silicon resonators: the influence of surface coatings. *Sensors and Actuators A*, 21:387–390, 1990.

[97] H.W.Ch. Postma, I. Kozinsky, A. Husain, and M.L. Roukes. Dynamic range of nanotube- and nanowire-based electromechanical systems. *Appl. Phys. Lett.*, 86, 2005.

[98] Albert Prak and Theo S.J. Lammerink. Effect of electronic strain on the

optically induced mechanical moment in silicon microstructures. *Journal of Applied Physics*, 71:5242–5245, 1992.

[99] Marcel W. Pruessner, Todd H. Stievater, Jacob B. Khurgin, and William S. Rabinovich. An integrated waveguide-DBR microcavity opto-mechanical system. *Optics Express*, 19(22):21904–21918, 2011.

[100] R.H. Rand. *Topics in Nonlinear Dynamics with Computer Algebra*. Gordon and Breach, 1994.

[101] Richard H. Rand. *Lecture Notes on Nonlinear Vibrations, ver. 45*. Available online at http://hdl.handle.net/1813/79, 2003.

[102] G.M. Rebeiz. *RF MEMS: Theory, Design and Technology*. John Wiley & Sons, Inc., 2004.

[103] Robert B. Reichenbach, Maxim K. Zalaludinov, Keith L. Aubin, David A. Czaplewski, Bojan Ilic, Harold G. Craighead, Jeevak M. Parpia, and Brian H. Houston. Resistively actuated micromechanical dome resonators. In *Proc. SPIE 5344*, pages 51–58, San Jose, CA, USA, Jan. 26 2004.

[104] Todd Remtema and Liwei Lin. Active frequency tuning for micro resonators by localized thermal stressing effects. *Sensors and Actuators A*, 91(3):326–332, 2001.

[105] H. Rokhsari, T.J. Kippenberg, T. Carmon, and K. J. Vahala. Radiation-pressure-driven micro-mechanical oscillator. *Optics Express*, 13(14):5293–5301, 2005.

[106] Tuhin Sahai, Rustom B. Bhiladvala, and Alan Taylor Zehnder. Thermo-mechanical transitions in doubly-clamped micro-oscillators. *International Journal of Non-Linear Mechanics*, 42(4):596–607, 2007.

[107] A.G. Salinger, E.A. Burroughs, R.P. Pawlowski, E.T. Phipps, and L.A. Romero. Bifurcation tracking algorithms and software for large scale applications. *International Journal of Bifurcation and Chaos*, 15(3):1015–1032, 2005.

[108] James C. Salvia, Renata Melamud, Saurabh A. Chandorkar, Scott F. Lord, and Thomas W. Kenny. Real-time temperature compensation of mems oscillators using an integrated micro-oven and a phase-locked loop. *Journal of Microelectromechanical Systems*, 19(1):192–201, 2010.

[109] Jeffrey B. Sampsell. Digital micromirror device and its application to projection displays. *Journal of Vacuum Science & Technology B: Microelectronics and Nanometer Structures*, 12(6):3242–3246, 1994.

[110] Peter R. Saulson. Thermal noise in mechanical experiments. *Physical Review D*, 42(8):2437–2445, 1990.

[111] Lidija Sekaric. *Studies in NEMS : Nanoscale Dynamics, Energy Dissipation, and Structural Materials*. PhD thesis, Cornell University, 2003.

[112] Lidija Sekaric, Maxim K. Zalalutdinov, Rustom B. Bhiladvala, Alan Taylor Zehnder, Jeevak M. Parpia, and Harold G. Craighead. Operation of nanomechanical resonant structures in air. *Appl. Phys. Lett.*, 81(14):2641–2643, 2002.

[113] Lidija Sekaric, Maxim K. Zalalutdinov, Stephen W. Turner, Alan Taylor Zehnder, Jeevak M. Parpia, and Harold G. Craighead. Nanomechanical resonant structures as tunable passive modulators of light. *Appl. Phys. Lett.*, 80(19):3617–3619, 2002.

[114] Seung-Bo Shim, Matthias Imboden, and Pritiraj Mohanty. Synchronized oscillation in coupled nanomechanical oscillators. *Science*, 316(95):95–99, 2007.

[115] Cristoph L. Spiel, R.O. Pohl, and Alan Taylor Zehnder. Normal modes of a Si(100) double-paddle oscillator. *Review of Scientific Instruments*, 72(2):1482–1491, 2001.

[116] R.G. Stearns and G.S. Kino. Effect of electronic strain on photoacoustic generation in silicon. *Applid Physics Letters*, 47:1048–1050, 1985.

[117] N.A.D. Stokes, Rebwar M.A. Fatah, and Shalini Venkatesh. Self-excitation in fiber-optic microresonator sensors. *Sens. Actuators, A*, 21:369–372, 1990.

[118] N.A.D. Stokes, R.M.A. Fatah, and S. Venkatesh. Self-excited vibrations of optical microresonators. *Electronic Letters*, 24(13):777–778, 1988.

[119] G.G. Stoney. The tension of metallic films deposited by electrolysis. *Proc. R. Soc. London, Ser. A*, 82:172175, 1909.

[120] Duane Storti and Richard H. Rand. Subharmonic entrainment of a forced relaxation oscillator. *Int. J. Non-Linear Mechanics*, 23(3):231–239, 1988.

[121] Steven H. Strogatz. *Nonlinear Dynamics and Chaos*. Perseus Books, 1994.

[122] John W. Suh, Steven F. Glander, Robert B. Darling, Christopher W. Storment, and Gregory T.A. Kovacs. Organic thermal and electrostatic ciliary microactuator array for object manipulation. *Sensors and Actuators A*, 58:51–60, 1997.

[123] K. Tanaka, Y. Mochida, M. Sugimoto, K. Moriya, T. Hasegawa, K. Atsuchi, and K. Ohwada. A micromachined vibrating gyroscope. *Sensors and Actuators A*, 50:111–115, 1995.

[124] Earl Arthur Thornton. *Thermal Structures for Aerospace Applications*. AIAA, 1996.

[125] K.E.B. THornton, D. Uttamchandani, and B. Culshaw. Temperature dependence of resonant frequency in optically excited diaphrams. *Electronics Letters*, 22:1232–1234, 1986.

[126] K.E.B. THornton, D. Uttamchandani, and B. Culshaw. Novel optically excited resonant pressure sensors. *Electronics Letters*, 24(10):573–574, 1988.

[127] T. Thundat, P.I. Oden, and R.J. Warmack. Microcantilever sensors. *Microscale Thermophysical Engineering*, 1(3):185–199, 1997.

[128] Harrie A.C. Tilmans, Miko Elwenspoek, and Jan H.J. Fluitman. Micro resonant force gauges. *Sens. Actuators, A*, 30:35–43, 1992.

[129] S.P. Timoshenko. On the correction factor for shear of the differential equation for transverse vibrations of bars of uniform cross-section. *Philosophical Magazine*, 41:744–746, 1921.

[130] S.P. Timoshenko. On the transverse vibrations of bars of uniform cross-section. *Philosophical Magazine*, 43:125–131, 1922.

[131] Stephen P. Timoshenko. *Vibration Problems in Engineering*. D. Van Nostrand Company, INC, 3rd edition, 1955.

[132] Rodney S. Tucker, Douglas M. Baney, Wayne V. Sorin, and Curt A. Flory. Thermal noise and radiation pressure in MEMS fabrypérot tunable filters and lasers. *IEEE Journal on Selected Topics on Quantum Electronics*, 8(1):88–97, 2002.

[133] Quirin P. Unterreithmeier, Stephan Manus, and Jörg P. Kotthaus. Coherent detection of nonlinear nanomechanical motion using a stroboscopic downconversion technique. *Applied Physics Letters*, 94, 2009.

[134] Balth Van der Pol and J. Van der Mark. Frequency demultiplication. *Nature*, 120:363–364, 1927.

[135] P.S. Waggoner and H.G. Craighead. Micro- and nanomechanical sensors for environmental, chemical, and biological detection. *Lab Chip*, 7:1238–1255, 2007.

[136] Yu Wang. *Surface Chemistry Control of Mechanical Energy Dissipation in Micromechanical Devices*. PhD thesis, Cornell University, 2004.

[137] Y.T. Yang, C. Callegari, X.L. Feng, K.L. Ekinci, and M.L. Roukes. Zeptogram-scale nanomechanical mass sensing. *Nano Letters*, 6(4):583–586, 2006.

[138] J.J. Yao and N.C. MacDonald. A micromachined, single-crystal silicon, tunable resonator. *J. Micromech. Microeng.*, 5, 1995.

[139] Kevin Y. Yasumura, Timothy D. Stowe, Eugene M. Chow, Timothy Pfafman, Thomas W. Kenny, Barry C. Stipe, and Daniel Rugar. Quality factors in micron- and submicron-thick cantilevers. *J. Microelectromech. Syst.*, 9(1):117–125, 2000.

[140] Mohammad I. Younis. *MEMS Linear and Nonlinear Statics and Dynamics*. Springer, 2011.

[141] Maxim Zalalutdinov, Keith Aubin, Christopher Michael, Robert B. Reichenbach, Tuncay Alan, Alan Zehnder, Brian Houston, Jeevak Parpia, and Harold Craighead. Shell-type micromechanical oscillator. In *SPIE International Symposium on Microtechnolgies for the New Millenium*, San Agustín, Gran Canaria, Spain, May 19-21, 2003.

[142] Maxim K. Zalalutdinov, Keith L. Aubin, Manoj Pandey, Alan Taylor Zehnder, Richard H. Rand, Harold G. Craighead, Jeevak M. Parpia, and Brian H. Houston. Frequency entrainment for micromechanical oscillator. *Appl. Phys. Lett.*, 83(16):3281–3283, 2003.

[143] Maxim K. Zalalutdinov, Anatoli Olkhovets, Alan Taylor Zehnder, Bojan Rob Ilic, David A. Czaplewski, Harold G. Craighead, and Jeevak M.

Parpia. Optically pumped parametric amplification for micromechanical oscillators. *Appl. Phys. Lett.*, 78(20):3142–3144, 2001.

[144] Maxim K. Zalalutdinov, Jeevak M. Parpia, Keith L. Aubin, Harold G. Craighead, Tuncay Alan, Alan Taylor Zehnder, and Richard H. Rand. Hopf bifurcation in a disk-shaped NEMS. In *Proceedings of the 2003 ASME Design Engineering Technical Conferences, 19th Biennial Conference on Mechanical Vibrations and Noise*, pages 1759–1769, Chicago, IL, Sept. 2-6, 2003.

[145] Maxim K. Zalalutdinov, Alan Taylor Zehnder, Anatoli Olkhovets, Stephen W. Turner, Lidija Sekaric, Bojan Rob Ilic, David A. Czaplewski, Jeevak M. Parpia, and Harold G. Craighead. Autoparametric optical drive for micromechanical oscillators. *Appl. Phys. Lett.*, 79(5):695–697, 2001.

[146] L.M. Zhang, D. Walsh, D. Uttamchanddani, and B. Culshaw. Effect of optical power on the resonance frequency of optically powered silicon microresonators. *Sensors and Actuators A*, 29:73–78, 1991.

[147] Imed Zine-El-Abidine and Peng Yang. A tunable mechanical resonator. *J. Micromech. Microeng.*, 19(12), 2009.

[148] J.D. Zook and D.W. Burns. Resonant microbeam strain transducers. In *International Conference on Solid-State Sensors and Actuators, 1991*, pages 529–532, San Francisco, CA, USA, June 24-27, 1991.